



universität
wien

DISSERTATION

Titel der Dissertation

„Simulation of phase transitions in ice:
methods and applications“

Verfasser

Mag. Philipp Geiger

angestrebter akademischer Grad

Doktor der Naturwissenschaften (Dr. rer. nat.)

Wien, im August 2013

Studienkennzahl lt. Studienblatt: A 091 411

Dissertationsgebiet lt. Studienblatt: Physik

Betreuerin / Betreuer: Univ.-Prof. Mag. Dr. Christoph Dellago

Danksagung

Beginnend möchte ich Prof. Christoph Dellago, meinem Doktorvater, danken. Besonders möchte ich meinen Dank dafür aussprechen, dass ich meine wissenschaftliche Ausbildung in einem bemerkenswerten Arbeitsumfeld absolvieren konnte, welches nicht nur auf meine fachliche Entwicklung starken Einfluss hatte, sondern ebenso charakterbildend war.

Wiewohl ich viele meiner Kollegen, welche Teil der *Computational Physics* Gruppe sind und waren, stolz und gerne als Freunde bezeichne, möchte ich diejenigen namentlich erwähnen, die maßgeblich zur fachlichen Durchführung dieser Doktorarbeit beigetragen haben. Im besonderen sind dies Andreas Singraber und Georg Menzl, denen ich auch speziell dafür danken möchte, dass sie die vorliegende Arbeit korrekturgelesen haben.

Neben Prof. Christoph Dellago, der für den Großteil meiner finanziellen Unterstützung verantwortlich war, sei auch Prof. Georg Kresse und Priv.-Doz. Andreas Tröster gedankt, die mich über einen längeren Zeitraum angestellt haben.

Wie weit ich wohl ohne die Unterstützung meiner Familie gekommen wäre, lässt sich kaum erahnen. Eine Frage, über die nachzudenken ich kaum wage, weshalb ich - ohne auf die unzähligen Gründe einzugehen - es dabei belasse, meinen bescheidensten Dank, aus tiefstem Herzen, meiner Frau Silvana und meiner Mutter Karin auszusprechen.

Zusammenfassung

Diese Doktorarbeit befasst sich mit der Entwicklung und Anwendung von Computersimulationsmethoden um das Phasenübergangsverhalten von komplexen Substanzen wie etwa Wasser zu untersuchen. Wir präsentieren eine Methode, mittels derer spezielle Bereiche im Phasenraum abgesucht und auf chaotisches Verhalten untersucht werden können. Insbesondere Sattelpunkte in der Landschaft der freien Energie können mittels dieser Methode gefunden werden. Solche Sattelpunkte spielen bei Nukleationsprozessen, wie sie bei Phasenübergängen erster Ordnung auftreten, eine wichtige Rolle. Die sorgfältige Definition eines Ordnungsparameters, welcher den gesamten Nukleationsprozess beschreibt, ist ein wesentlicher Bestandteil der Studie, da eine Methode benötigt wird, um die beteiligten Strukturen eindeutig zu unterscheiden. Wir stellen in dieser Arbeit eine neue Methode vor, die es ermöglicht, mittels künstlicher neuronaler Netzwerke diverse Phasen einer Substanz zu unterscheiden. Dabei wird die Zugehörigkeit eines Einzelteilchens zu einer gewissen Struktur nur über dessen lokale Umgebung bestimmt. Aufgrund dieser Zuweisung ist es dann möglich Ordnungsparameter zu definieren, um damit Phasenübergänge zu studieren. Weiters demonstrieren wir die Effizienz unserer Strukturerkennungsmethode an der Unterscheidung zwischen flüssigen, sowie diversen Nieder- und Hochdruckeisphasen. Den zweiten Teil der vorliegenden Arbeit bildet eine Studie über das Phasenverhalten von Wasser. Wir zeigen dabei Infrarotspektren von kubischem Eis und prognostizieren basierend auf experimentellen Daten die Eigenschaften einer möglichen neuen kubischen Eisphase. Weiters zeigen wir Simulationsergebnisse für die Nukleation von hexagonalem Eis in unterkühltem flüssigen Wasser. Bei einem Unterkühlungsgrad von 13 % besteht der kritische Nukleus aus ungerfähr 300 Molekülen, wobei die Höhe der freien Energiebarriere $34 k_B T$ beträgt.

Abstract

This thesis focuses on the development of methods to study phase transitions of complex substances. In particular, we present a method to generate very atypical trajectories by biasing the sampling toward a certain degree of chaoticity. Such trajectories can exhibit the chaotic properties which characterize transition pathways in first order phase transitions. To track the progress of a transition during the nucleation process an order parameter only depending on the local environment of a single particle is needed. We develop a method which exploits the pattern recognition capabilities of artificial neural networks to differentiate a wide array of possible structures. In particular, we apply this structure detection method on the distinction of liquid water and several low and high pressure ice phases. The second part of this work covers the study of properties of liquid water and ice, for instance the prediction of a new ice phase by means of infrared spectroscopy. This prediction is based on experimental, as well as computational results. Furthermore, results of the study of the nucleation of undercooled liquid water into hexagonal ice using the aforementioned technique are presented. Here, for a degree of undercooling of 13% the critical nucleus consists of 300 molecules and the height of the barrier is roughly $34k_B T$.

Preface

The majority of results presented in this thesis have also been published in or submitted to peer-reviewed journals. In particular, these are:

1. The main part of Chapter 1 is published under the title "Identifying rare chaotic and regular trajectories in dynamical systems with Lyapunov weighted path sampling" in *Chemical Physics*, 375, 309–315 (2010).
2. An article with the title "Neural networks for local structure detection in polymorphic systems" including Chapters 2 and 4 has been submitted to *Journal of Chemical Physics*.
3. Chapter 3 has been submitted to *Physical Review B* as an article with the title "Proton ordering of cubic ice Ic: spectroscopy and computer simulations".

Contents

| | |
|---|-----------|
| Introduction | 1 |
| I. Novel methods | 3 |
| 1. Creating reactive pathways with Lyapunov weighted path sampling | 5 |
| 1.1. Motivation | 6 |
| 1.2. Lyapunov instability | 7 |
| 1.3. Numerical determination of finite time Lyapunov exponents | 10 |
| 1.4. Lyapunov weighted trajectory ensemble | 10 |
| 1.5. Sampling trajectories with TPS | 11 |
| 1.6. Results | 12 |
| 1.6.1. Standard map | 13 |
| 1.6.2. Spring pendulum | 15 |
| 1.6.3. Lorentz gas | 17 |
| 1.6.4. Fermi-Pasta-Ulam chain | 20 |
| 1.6.5. Double well system | 21 |
| 1.6.6. Double well dimer in a solvent | 23 |
| 1.7. Conclusions | 25 |
| 2. Structure detection using neural networks | 29 |
| 2.1. The problem of detecting local structures | 30 |
| 2.2. Neural network for structure recognition | 33 |
| 2.2.1. Feed-forward neural network | 33 |
| 2.2.2. Symmetry functions | 36 |
| 2.2.3. Training the neural network | 40 |
| 2.2.4. Implementation details | 41 |
| 2.2.5. Application to Lennard-Jones systems | 43 |

| | |
|--|------------|
| 2.2.6. Comparison to Steinhardt bond order parameters | 49 |
| 2.2.7. Parameters of symmetry functions | 53 |
| II. Application: Simulation of ice | 55 |
| 3. Proton ordering of cubic ice | 57 |
| 3.1. Introduction | 58 |
| 3.2. Simulations | 61 |
| 3.2.1. Model and Methods | 61 |
| 3.2.2. Simulation results | 64 |
| 3.3. Experiments | 74 |
| 3.4. Discussion | 78 |
| 4. Detection of ice structures | 83 |
| 4.1. Motivation | 84 |
| 4.2. Training set | 85 |
| 4.3. Symmetry functions | 86 |
| 4.4. Neural network training and structure detection | 89 |
| 4.5. Crystallization of supercooled water | 89 |
| 4.6. Summary and conclusions | 93 |
| 4.7. Parameters of symmetry functions | 96 |
| 5. Technical aspects | 97 |
| 5.1. Modeling the water molecule | 98 |
| 5.2. Generation of ice crystal structures | 99 |
| 5.3. Equilibrium sampling | 101 |
| 5.4. Electrostatic interactions | 102 |
| 5.4.1. Convergence parameter | 104 |
| III. Appendices | 111 |
| A. Determination of linearized equation of motion for pair potentials | 113 |
| B. Time-propagation of rigid water molecules in various ensembles | 117 |
| B.1. Mathematical basics | 117 |

| | |
|---|------------|
| B.2. Dynamics in the NVE ensemble | 122 |
| B.3. Dynamics in the NVT ensemble | 125 |
| B.4. Dynamics in the NPT ensemble | 128 |
| Index | 137 |
| Bibliography | 139 |

Introduction

This thesis focuses on two major fields of study mainly examined by computational methods in chemical physics. In particular, these are the study of solid water phases and the transition process a system undergoes when it transforms from one phase to another. This thesis is divided into two parts, the first one describing two novel methods to study phase transitions and the second containing the applications of these methods and the simulation of ice in general.

The first technique described here is the *Lyapunov weighted path ensemble* which can be used to sample trajectories with atypical chaotic properties. The idea is to generate a weighted ensemble of trajectories such that a pre-adjusted degree of chaoticity is achieved. In the language of chaos theory, a phase transition takes place when the system crosses saddle points in phase space. Such saddle points are characterized by their ability to 'produce' chaos. Thus, when favoring trajectories with high chaoticity the system can be dragged through phase space to produce reactive trajectories, which connect two thermodynamic states of the system. This feature can be utilized to study phase transitions where the two states are separated by high barriers in the free energy landscape. A supercooled liquid for example, stays in its meta-stable state for long times before a so-called rare event takes place, which lets the system cross the free energy barrier to the thermodynamically stable solid phase. Usually, this barrier is high enough to prevent the system from overcoming the barrier for very long times. This motivates our approach to speed up the system's dynamics by sampling only reactive trajectories.

Another approach introduced in this thesis is a newly-developed method to assign the particles within a simulation box to certain phases. For example, when nucleation processes are studied, crucial insights can be gained from the properties of the critical nucleus. Here, a cluster of particles of the more stable phase is embedded by surrounding particles in the initial meta-stable phase. To track the growth of the nucleus a quantity is needed which classifies the clustered particles and distinguish them in a unique way. Such local bond order parameters are designed to be sensi-

tive to specific symmetries by using geometrical information of neighboring particles. While many methods exist to provide bond order parameters, a general procedure is missing and in principle each molecular substance needs a custom approach. In particular, for the high pressure phases of ice conventional methods to detect those structures fail. To overcome this problem we have developed a very unconventional but powerful method, where we treat this detection problem as a pattern recognition problem for *artificial neural networks*. This approach, referred to in the following as the *neural network structure detection* method, provides a generalized way to identify structures based on local spatial information, thus providing a quantity to describe phase transitions where structural symmetry changes are involved.

The applications part covers a few general properties of liquid water and ice, for instance a detailed study of proton ordering of cubic (Ic) and hexagonal (Ih) ice and a study of the nucleation of liquid water into low-density ice Ih. The last chapter of the applications part covers technical aspects of the computer simulation of water, in particular the proper treatment of the Coulombic interactions. This thesis is closed by a comprehensive appendix containing mathematical derivations and methods used to obtain the results presented here.

Part I.

Novel methods

In the last decades, the study of physical phenomena using computer simulation has been established as its own discipline somewhere between experimental and theoretical physics. In the center of this discipline is the development and the application of numerical methods.

In this part we introduce two newly-developed techniques mainly used to study the transition mechanism of nucleation processes. The first method, which uses principles of chaos theory can be used to search for reactive pathways connecting two thermodynamically stable states. The second method uses artificial neural networks to recognize structures only from local spatial information and differentiate between different polymorphs of a given substance.

Chapter 1.

Creating reactive pathways with Lyapunov weighted path sampling

Depending on initial conditions, individual finite time trajectories of dynamical systems can have very different chaotic properties. Here we present a numerical method to identify trajectories with atypical chaoticity, pathways that are either more regular or more chaotic than average. The method is based on the definition of an ensemble of trajectories weighted according to their chaoticity, the Lyapunov weighted path ensemble. This ensemble of trajectories is sampled using algorithms borrowed from transition path sampling, a method originally developed to study rare transitions between long-lived states. We demonstrate our approach by applying it to several systems with numbers of degrees of freedom ranging from one to several hundred and in all cases the algorithm found rare pathways with atypical chaoticity. For a double-well dimer embedded in a solvent, which can be viewed as simple model for an isomerizing molecule, rare reactive pathways were found for parameters strongly favoring chaotic dynamics.*

* The main part of this chapter is published in *Chemical Physics*, 375, 309-315 (2010) under the title "Identifying rare chaotic and regular trajectories in dynamical systems with Lyapunov weighted path sampling".

1.1. Motivation

The phase space of dynamical systems often exhibit regions with qualitatively very different dynamics. In the Henon-Heiles model or similar low-dimensional Hamiltonian systems, for instance, islands of stability are embedded in a chaotic sea [1]. Other examples for this kind of behavior include the Fermi-Pasta-Ulam chain, in which special initial conditions lead to physically very different soliton and "chaotic breather" solutions, and gravitational many-body systems in celestial mechanics, which, for appropriate initial conditions, produce orbits that are stable for very long times [2]. Although such particularly regular (or irregular) trajectories may be very rare, they may be responsible for important physical phenomena as is the case for chemical reactions, where trajectories passing through unstable saddle points regions carry the system from one chemical species to another [3, 4].

Identifying and describing such trajectories is therefore of great interest. Recently, Tailleur and Kurchan [5] presented a powerful new method, the *Lyapunov weighted dynamics* (LWD), which is applicable to a broad range of high-dimensional problems. In this evolutionary approach, a swarm of walkers progress according to the rules of the underlying dynamics. The walkers proliferate or die depending on the degree of chaos encountered by the system along a particular trajectory and, after many generations, only walkers on trajectories with the desired stability properties survive. Tailleur and Kurchan have demonstrated that their method is capable of finding even very small stability regions in systems of many degrees of freedom.

Inspired by the work of Tailleur and Kurchan, we introduce here a general and efficient algorithm for finding trajectories with atypical stability properties, which is equally applicable to stochastic and deterministic dynamics. The central notion of our approach lies in the definition of a Lyapunov weighted path ensemble, in which the statistical weight of trajectories explicitly depends on a measure for the chaoticity of the underlying dynamics. The degree with which particularly chaotic trajectories are favored or disfavored depends on the value of a parameter that can be viewed as conjugate to the measure of chaos, for instance the Lyapunov exponent [1]. This ensemble of trajectories is then sampled using techniques borrowed from transition path sampling (TPS), a method originally developed to study rare transitions between long-lived stable states in complex molecular systems [6–9]. Note that a related combination of transition path sampling with a Lyapunov weighted action has been suggested before [10, 11]. By construction, the transition path sampling

procedure generates a Markov chain of trajectories distributed according to the chosen bias function. Following the terminology of Tailleur and Kurchan [5], we call this approach *Lyapunov weighted path sampling*. Similar techniques were recently used by Chandler and collaborators to sample an ensemble of trajectories weighted by an order parameter describing the mobility of particles in a system undergoing the glass transition [12].

The remainder of this chapter is organized as follows. In Sec. 1.2 we briefly introduce the concept of Lyapunov instability and discuss ways to probe chaotic dynamics along individual trajectories. In Sec. 1.4 we define the Lyapunov weighted path ensemble and in Sec. 1.5 we explain how it can be sampled with transition path sampling algorithms. In Sec. 1.6 this approach is then applied to detect particularly stable and unstable trajectories in various systems. Conclusions are provided in Sec. 1.7.

1.2. Lyapunov instability

Chaotic dynamical systems are characterized by a strong sensitivity to small changes in the initial conditions. To quantify this concept, consider a dynamical system, described by a set of N coupled first order ordinary differential equations,

$$\dot{\mathbf{x}} = \mathbf{F}(\mathbf{x}), \quad (1.1)$$

where x denotes a point in the N -dimensional phase space. The formal solution of this differential equations reads

$$\mathbf{x}(t) = \phi_t(\mathbf{x}_0), \quad (1.2)$$

where the time evolution operator ϕ_t is called the propagator and given by

$$\phi_t = e^{i\mathcal{L}t}, \quad i\mathcal{L} = \mathbf{F}(\mathbf{x}) \cdot \frac{\partial}{\partial \mathbf{x}}, \quad (1.3)$$

with Liouville operator \mathcal{L} . The time evolution of an infinitesimally small deviation $\delta\mathbf{x}$ separating two close-by trajectories is then governed by the linearized equations of motion

$$\delta\dot{\mathbf{x}}(t) = \mathbf{D}(\mathbf{x})\delta\mathbf{x}(t), \quad (1.4)$$

where $\mathbf{D}(\mathbf{x}) = \partial\mathbf{F}/\partial\mathbf{x}$ is the Jacobi matrix of the system evaluated at \mathbf{x} . Eq. (1.4) has the formal solution

$$\delta\mathbf{x}(t) = \frac{\partial}{\partial \mathbf{x}_0} \phi_t(\mathbf{x}_0) \delta\mathbf{x}_0. \quad (1.5)$$

In a chaotic system, two points in phase space, initially separated by $\delta\mathbf{x}(0)$ at time $t = 0$, will lead to trajectories that, on average, separate exponentially in time, $|\delta\mathbf{x}(t)| \approx |\delta\mathbf{x}(0)| \exp(\lambda t)$. Here, the vertical lines denote the Euclidean norm of a vector. The coefficient λ , the long-time averaged growth rate of infinitesimally small displacements defined as

$$\lambda = \lim_{t \rightarrow \infty} \frac{1}{t} \ln \frac{|\delta\mathbf{x}(t)|}{|\delta\mathbf{x}(0)|}, \quad (1.6)$$

is called the Lyapunov exponent of the system. A positive Lyapunov exponent corresponds to exponential growth of an initially small perturbation and implies information loss and strong sensitivity to initial conditions, the defining feature of chaotic dynamics. (It is possible to define whole spectra of Lyapunov exponents characterizing the growth rates of small perturbation in different directions of phase space [13, 14]. In this article, however, we will consider only the largest Lyapunov exponent defined in Eq. (1.6).)

Since Lyapunov exponents are defined as long-time averages, in an ergodic system every initial condition will yield the same λ . For finite periods of time however, trajectories can display very different chaotic properties. An example are trajectories in “sticky regions” in the phase space of the standard map, in which trajectories can spend a long time before escaping away into more chaotic regions [15, 16]. Other parts of phase space may be filled with regular periodic orbits that have a vanishing Lyapunov exponents and are dynamically disconnected with the chaotic surroundings. To describe such behavior of individual trajectories of finite length it is convenient to consider so-called finite time Lyapunov exponents $\lambda_f(\mathbf{x}_0, t)$ that depend on the initial condition \mathbf{x}_0 and on the temporal trajectory length t ,

$$\lambda_f(x_0, t) = \frac{1}{t} \ln \frac{|\delta\mathbf{x}(t)|}{|\delta\mathbf{x}(0)|}. \quad (1.7)$$

Such finite time Lyapunov exponents can be used to quantify the chaoticity of finite length trajectories.

One difficulty occurring in the definition of the finite time Lyapunov exponent of Eq. (1.7), however, is that λ_f also depends on the initial orientation of the displacement vector $\delta\mathbf{x}(0)$. This vector reorients into the direction of fastest growth, but, depending on the degree of chaos prevalent in the respective phase space region, this reorientation may take a time long with respect to the trajectory length t . In fact, the time τ_r it takes to turn the displacement vector into the direction of the fastest growth is inversely proportional to the difference of the two largest

Lyapunov exponents $\tau_r \propto 1/(\lambda_1 - \lambda_2)$ [17]. Here, λ_1 and λ_2 are the largest and the second largest Lyapunov exponent, respectively. This ambiguity in the definition of the finite time Lyapunov exponent can be avoided by integrating the equations of motion backwards for a time t_- longer than τ_r starting from the initial condition \mathbf{x}_0 . If the equations of motion for the displacement vector $\delta\mathbf{x}$ are then integrated forward starting from \mathbf{x}_{-t_-} with an arbitrary orientation of the displacement vector and following the reference trajectory, the displacement vector has oriented into the direction of fastest growth when \mathbf{x}_0 is reached. Then, the displacement vector has a well defined orientation at $t = 0$ and the definition of the finite time Lyapunov exponent for the trajectory from \mathbf{x}_0 to \mathbf{x}_t is unique. Since the reorientation time τ_r may be large, this procedure can require the computation of long additional trajectory segments causing large computational costs.

An alternative way to quantify the chaoticity of individual finite length trajectories consists in determining the *Relative Lyapunov Indicator* (RLI) [18, 19], originally introduced to detect chaotic dynamics in planetary systems. This measure has been proven particularly useful to distinguish regular from chaotic trajectories in systems that are only weakly chaotic. The main idea of the RLI is to exploit the fact that in the chaotic regions of phase space, finite time Lyapunov exponents vary discontinuously as a function of the initial condition, i.e., adjacent points can have very different local expansion rates [20, 21]. The RLI is defined as the magnitude of the difference $\Delta\lambda(\mathbf{x}_0, t)$ between the finite time Lyapunov exponents of two trajectories separated by a small but finite amount $\Delta\mathbf{x}_0$,

$$\Delta\lambda(\mathbf{x}_0, t) = |\lambda(\mathbf{x}_0 + \Delta\mathbf{x}_0, t) - \lambda(\mathbf{x}_0, t)|. \quad (1.8)$$

It has been shown that the RLI is insensitive both to the separation $\Delta\mathbf{x}_0$ as well as to the initial infinitesimal phase space displacement $\delta\mathbf{x}(0)$ used to calculate the finite time Lyapunov exponents $\lambda(\mathbf{x}_0, t)$. To reduce fluctuations, one can average the RLI over time,

$$R(\mathbf{x}_0, t) = \overline{\Delta\lambda(\mathbf{x}_0, \Delta t)} = \frac{1}{t/\Delta t} \sum_{i=1}^{t/\Delta t} \Delta\lambda(\mathbf{x}_0, i\Delta t), \quad (1.9)$$

where Δt is the time step used for the numerical integration of the equations of motion. In the following we will use this smoothed version of the RLI to characterize the chaoticity of individual trajectories in various dynamical systems.

1.3. Numerical determination of finite time Lyapunov exponents

Due to the finite precision of computer floating point arithmetic Eq. (1.7) cannot be used to calculate Lyapunov exponents. Since every deviation grows exponentially, even the smallest possible number ($|\delta\mathbf{x}_0| = 10^{-15}$ for double precision) would exceed characteristic length scales within short times. To overcome this issue the Lyapunov exponent can be defined as sum over local Lyapunov exponents

$$\lambda_f(\{\mathbf{x}_n\}, t) = \frac{1}{t} \sum_{n=1}^{t/\Delta t} \lambda_l(\mathbf{x}_n, \mathbf{x}_{n-1}, \Delta t), \quad (1.10)$$

where $\{\mathbf{x}_n\}$ is the vector of all visited phase space points and

$$\lambda_l(\mathbf{x}_n, \mathbf{x}_{n-1}, \Delta t) = \frac{1}{\Delta t} \ln \frac{|\delta\mathbf{x}_n|}{|\delta\mathbf{x}_{n-1}|}. \quad (1.11)$$

Since we are only interested in the stretching factor of the deviation vector $\delta\mathbf{x}$ between two time steps, we can normalize $\delta\mathbf{x}_n$ after each time step. Calculating the finite time Lyapunov exponent incorporates the following steps:

- (a) Choose an arbitrary point in phase space \mathbf{x}_0 and a randomly orientated unit vector $\delta\mathbf{x}_0$ as initial values.
- (b) Integrate the differential equations governing the time evolution of the system (Eq. 1.1) for one time step Δt .
- (c) Integrate the linearized equations (Eq. 1.4).
- (d) Determine the local Lyapunov exponent λ_l .
- (e) Renormalize the deviation vector.
- (f) Repeat steps (b) to (e) until desired trajectory length t is reached.
- (g) Finally, calculate λ_f by summing over all local Lyapunov exponents λ_l .

A general way to determine the Jacobian for systems with only pairwise interactions is given in Appendix A.

1.4. Lyapunov weighted trajectory ensemble

As outlined in the Introduction, the goal of the work presented in this chapter is to identify trajectories that have particular stability properties. For instance, one

might be interested in locating regions of phase space that are populated by regular trajectories or in finding those pathways that are most chaotic. To do that, we start by defining an ensemble of trajectories including an additional weight that favors trajectories with the desired chaoticity properties. We assume that the dynamics generate a stationary distribution $\rho(\mathbf{x})$. Since we consider only deterministic systems here, we represent trajectories of length t by their initial phase space point \mathbf{x}_0 and define the *Lyapunov weighted path ensemble* (LWPE) as

$$\rho_L(\mathbf{x}_0, t) = \frac{1}{Q} \rho(\mathbf{x}_0) e^{\alpha t R(\mathbf{x}_0, t)}, \quad (1.12)$$

where the factor $Q = \int d\mathbf{x}_0 \rho(\mathbf{x}_0) e^{\alpha t R(\mathbf{x}_0, t)}$ normalizes the distribution. Here, the parameter α , which can be viewed as conjugate to the chaoticity indicator $R(\mathbf{x}_0, t)$, controls how strongly the weight of initial condition \mathbf{x}_0 is changed according to the chaoticity of the trajectory evolving out of \mathbf{x}_0 . An analogous ensemble of trajectories can be easily defined using finite time Lyapunov exponents if they can be calculated accurately (simply replacing $R(\mathbf{x}_0, t)$ with $\lambda_f(\mathbf{x}_0, t)$ in the above equation). Large positive values of α favor strongly chaotic trajectories with a large chaoticity indicator. For negative α , on the other hand, weakly chaotic or regular trajectories with a small chaoticity indicator are given a larger weight in the ensemble. Note that a similar ensemble of trajectories can easily be constructed also for stochastic dynamics and appropriately defined Lyapunov exponents.

1.5. Sampling trajectories with TPS

We sample the Lyapunov weighted path ensemble with a technique borrowed from transition path sampling [6, 8, 9], a method originally developed to simulate rare but important transitions between long-lived stable states as they occur, for instance, in protein folding, chemical reactions and first order phase transitions. In a transition path sampling simulation a biased random walk is carried out in the space of trajectories in a way such that trajectories are sampled according to their weight in the desired ensemble. This is accomplished using a Monte Carlo (MC) procedure in which a trial trajectory is generated from the current trajectory and then accepted according to the Metropolis rule. Iterating this basic step, a set of trajectories with the correct probability is generated. A particularly efficient way to generate trial pathways is the so called shooting algorithm [22, 23], also used in the present work.

In this approach, a new trajectory is generated from an old one by first randomly selecting a point on the old trajectory, and then integrating the equations of motion starting with perturbed momenta. The magnitude of the perturbation of the momenta controls how different the new trajectory is from the old one and, therefore, also controls the average acceptance probability of the Monte Carlo procedure.

In more detail, the path sampling procedure of the Lyapunov weighted path ensemble is carried out in the following way. The first trajectory is created by integrating the equations of motion starting from an arbitrary initial condition x_0 . From this trajectory one then selects a point at random. At this so-called shooting point, the momenta are slightly changed by addition of a small perturbation drawn from a Gaussian distribution. The new trajectory is then obtained by integrating the equations of motion forward to time t and backward to time 0. The new trajectory with initial condition $\mathbf{x}_0^{(n)}$ and chaoticity indicator $R(\mathbf{x}_0^{(n)}, t)$ is accepted with probability

$$p_{\text{acc}} = \min \left\{ 1, \frac{\rho(\mathbf{x}_0^{(n)})}{\rho(\mathbf{x}_0^{(o)})} e^{at[R(\mathbf{x}_0^{(n)}, t) - R(\mathbf{x}_0^{(o)}, t)]} \right\}. \quad (1.13)$$

where $\mathbf{x}_0^{(o)}$ and $R(\mathbf{x}_0^{(o)}, t)$ denote the initial point and the chaoticity indicator of the old trajectory, respectively. If the new trajectory is accepted, the procedure will be repeated with this trajectory. Otherwise the old trajectory is kept as the current one. The acceptance probability of Eq. (1.13) is derived from the detailed balance condition and guarantees that trajectories are harvested according to the Lyapunov weighted path ensemble. Note that to obtain Eq. (1.13) we have assumed a momentum perturbation that leads to a symmetric generation probability. If this is not the case, an appropriate factor must be taken into account in the acceptance probability. The shifting algorithm of transition path sampling [22, 23] can be adapted in a similar way to sample the Lyapunov weighted path ensemble. In the next section we discuss the application of this method to various chaotic dynamical systems.

1.6. Results

In this Section we use the method outlined above to identify particularly stable and unstable trajectories in various dynamical systems with dimensionality ranging from two to several hundred. For better comparison, we mostly follow Ref. [5] in our choice of examples.

1.6.1. Standard map

The standard map is a representation of the dynamics of a free rotor kicked at regular intervals with an impulsive force in a given direction [1, 24]. For a kicking period of 1 and a kick strength of k , the standard map is given by

$$\begin{aligned}\omega_{n+1} &= \omega_n - \frac{k}{2\pi} \sin(2\pi\varphi_n), \\ \varphi_{n+1} &= \varphi_n + \omega_{n+1},\end{aligned}\tag{1.14}$$

where ω_n and φ_n are the angle and the angular momentum of the rotor immediately after the n -th kick, respectively. Due to the periodicity of the motion, both variable ω and φ are considered on a torus (by taking ω and φ modulo 1). The standard map is area preserving and, depending on the value of k , displays different degrees of chaos. For vanishing k , the dynamics reduces to the motion of a free rotor and the system is integrable. Accordingly, the largest Lyapunov exponent vanishes. As the parameter k is turned on, some chaos develops in particular regions of the two-dimensional phase space, while other regions originating from KAM-tori remain regular resulting in a phase space structure consisting of islands of stability embedded in a chaotic sea [1, 24]. As k is increased, the stable regions shrink and for large values of k only a very small fraction of initial conditions lead to regular trajectories. In the following we will sample the Lyapunov weighted path ensemble to find these rare regular trajectories.

To sample trajectories of the standard map we use the standard shooting algorithm, in which a new trajectory is obtained from the current one by first selecting a phase space point on the current trajectory. Then, the selected point is slightly perturbed by addition of a random displacement drawn from a Gaussian distribution with width σ_G to both φ and ω . Starting from this perturbed initial condition, the new trajectory is obtained by carrying out an appropriate number of iterations of the standard map in forward direction and of the inverse map in backward direction. Finally, the new trajectory is accepted with the acceptance probability of Eq. (1.13).

Using the shooting algorithm we have generated 10^5 trajectories of length $n = 10^4$ with $\sigma_G = 0.05$ for a kicking strength of $k = 7.7$. In this case, the chaotic sea covers almost the entire phase space. The magnitude of initial point deviation for the RLI calculation was $|\Delta\mathbf{x}_0| = 10^{-12}$ and the probability density $\rho(\mathbf{x}_0)$ of initial conditions was assumed to be uniform. To find the rare regular trajectories a negative value of the control parameter $\alpha = -4$ was used. The right choice of this parameters is

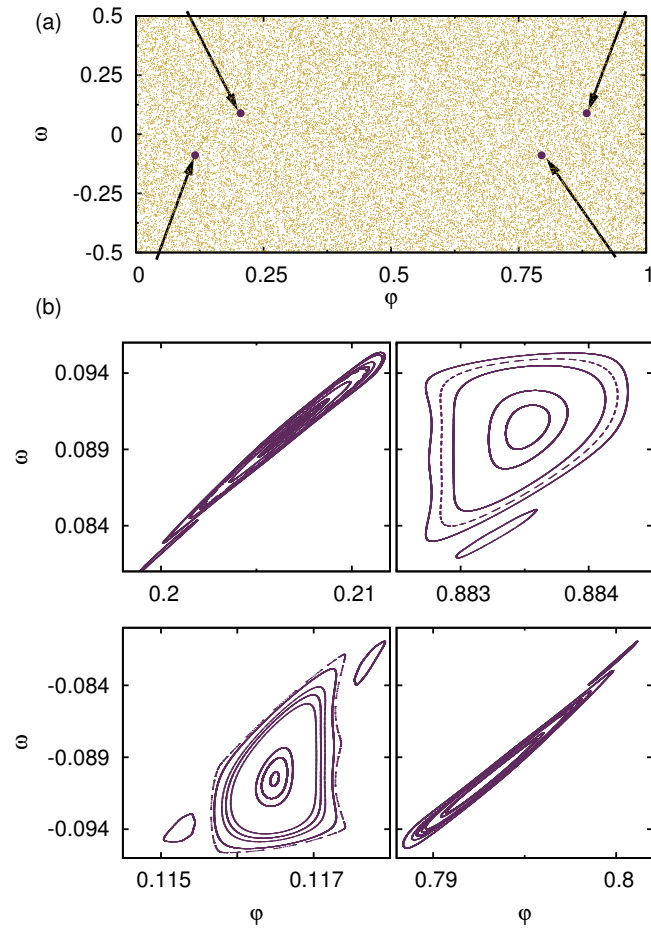


Figure 1.1.: (a) Phase space plot of the standard map for $k = 7.7$. The arrows indicate the locations of the stability islands, which are not visible at the scale of the figure. (b) Enlarged phase space portraits of the regular trajectories found by the Lyapunov weighted path sampling algorithm.

crucial as it controls how phase space is sampled in a way that is analogous to the effect of the inverse temperature in a regular Monte Carlo simulation. A very large negative value of α favors regular trajectories very strongly such that the simulation gets trapped very easily in local minima of the RLI and the most regular trajectories are not found. A small negative value of α , on the other hand, does not generate a sufficiently strong bias towards the atypical regular trajectories such they may not be found in this case either. Using these parameters, several rare regular trajectories were found in the simulation as displayed in Fig. 1.1. These regular trajectories correspond to the four stable islands found also in Ref. [5]. For the stable orbits the RLI values ranged from 10^{-14} to 10^{-12} compared to values of 10^{-4} for typical trajectories in the chaotic sea. As can be inferred from Fig. 1.1, the regular islands cover only a very small part of phase space. The fact that regular trajectories are nevertheless found in the simulation indicates that the landscape of the chaoticity indicator must have a global funnel-like shape that attracts the simulation towards the regions of highest regularity.

1.6.2. Spring pendulum

We next consider the spring pendulum evolving according to Hamilton's equation of motion. This two-dimensional system consists of a point of mass m exposed to a constant force of magnitude g in negative y -direction attached to a fixed pivot by a harmonic spring such that both angle and length of the pendulum can change in time. The Hamiltonian of the spring pendulum is given by

$$\mathcal{H} = \frac{p^2}{2m} + \frac{k}{2}(r - R)^2 + g y, \quad (1.15)$$

where $r = \sqrt{x^2 + y^2}$ is the distance of the mass point to the pivot, $p^2 = p_x^2 + p_y^2$ is the squared magnitude of the momentum, k is the spring constant and R is the equilibrium length of the spring [21, 25]. In all following calculations, the mass m , the equilibrium length R and the force constant k are set to unity and the force strength to $g = 2$.

For this model, we have carried out a Lyapunov weighted path ensemble simulation for two different values of the parameter α . In both cases, the total energy was $E = 2$ and the equations of motion are integrated with a time step of $\Delta t = 10^{-3}$ using the symplectic time-reversible Forest-Ruth algorithm of fourth order [26] yielding good energy conservation. The shooting algorithm was carried out in the usual way by

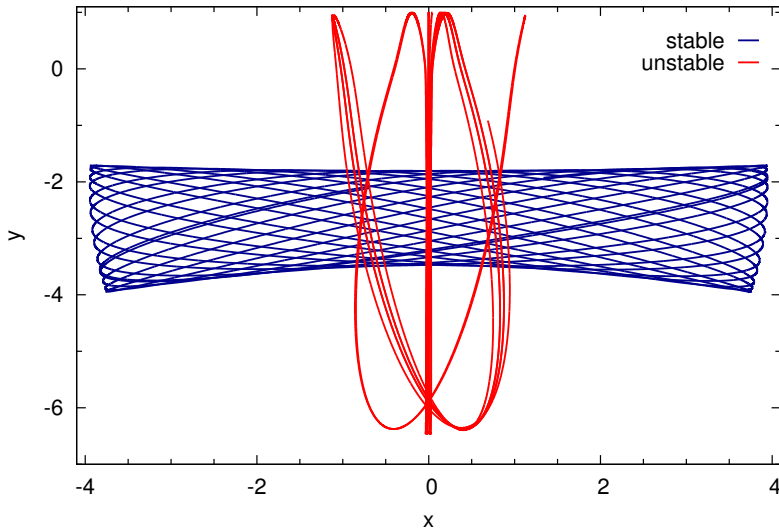


Figure 1.2.: Very stable and unstable trajectories of the spring pendulum traced out in configuration space. In both cases the energy is $E = 2$.

adding perturbations drawn from a Gaussian distribution to the momenta at the shooting point. Results of these simulations are displayed in Fig. 1.2. The very stable trajectory of length $\tau = 100$ was obtained after 4000 iterations of the path sampling algorithm with $\alpha = -5 \times 10^{11}$ favoring regular trajectories. In this calculation the magnitude of the shooting displacement was $\sigma_G = 0.5$. This trajectory has an RLI of $\sim 2 \times 10^{-14}$, a value which is about four orders of magnitude smaller than that of a typical trajectory.

The unstable trajectory of Fig. 1.2 has been found after 3000 iterations carried out with $\alpha = 10^6$ and a shooting displacement of magnitude $\sigma_G = 5 \times 10^{-4}$. This trajectory has an RLI of $\sim 6 \times 10^{-3}$, which is about 6 orders of magnitude larger than that of typical trajectories. The time evolution of the RLI for both trajectories is plotted in Fig. 1.3. The qualitative difference between the two trajectories of Fig. 1.2 is remarkable. While the stable trajectory has large amplitude in the angular degree of freedom, the unstable one displays pronounced stretching movements with smaller angular oscillations.

To highlight this behavior we have plotted a Poincaré section of the pendulums phase space, where each point is colored depending on its local Lyapunov exponent (see Eq. (1.11)). This was done by calculating the local Lyapunov exponent for a

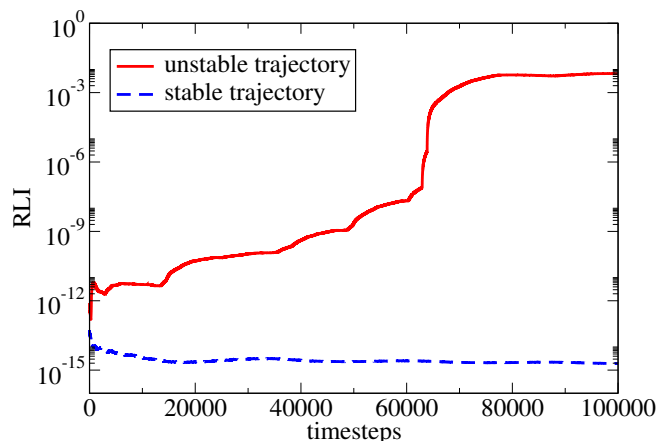


Figure 1.3.: Time evolution of the RLI for a stable and an unstable trajectory, respectively.

fine-meshed $x - y$ grid every time $p_x = 0$ occurs for a very long trajectory of $\tau = 10^9$. Since we have performed constant energy integration, the phase-space of our system is $d = 3$. Thus, a Poincaré section ($d - 1$) is two-dimensional for this system.

1.6.3. Lorentz gas

In 1963 Yakov G. Sinai has studied a dynamical system theoretically, where a disc is trapped in area with hard walls and a scatterer in its center [27]. This so-called Sinai billiard and very similar systems have been the topic of many studies in the field of dynamical system and deterministic chaos since. When extended and considered as a model for a classical gas, such a system is referred to in literature as the Lorentz gas [28, 29].

Usually modeled with hard discs, here the scatterers are implemented using soft potentials in order to perform Hamiltonian dynamics, where the Hamiltonian is given by

$$\mathcal{H} = \frac{\mathbf{p}^2}{2m} + \sum_i \Phi(|\mathbf{r} - \mathbf{r}_i|). \quad (1.16)$$

Here \mathbf{p} is the momentum and \mathbf{r} the position vector, respectively. The scatterers are described by a repulsive potential Φ centered at position \mathbf{r}_i . We model the Lorentz gas on a hexagonal lattice, where a cell consisting of one scatterer in its origin is replicated using periodic boundary conditions. Thus, in Eq. (1.16) the sum

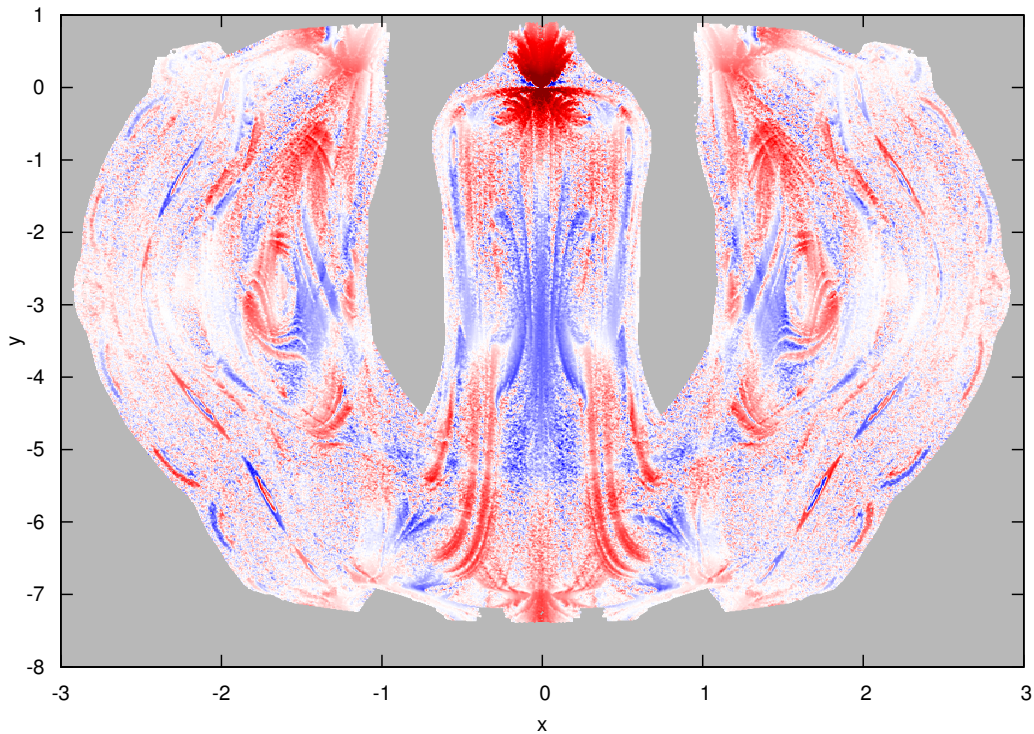


Figure 1.4.: Poincaré section of the spring pendulum. The color code represents the size of the largest local Lyapunov exponent, where blue corresponds to negative values and red to positive values, respectively. Gray colored areas were not visited during the simulation.

goes from $i = 0, \dots, 3$ and the r_i are the corners of the box (see Fig. 1.5). We have used the geometry of a perfect hexagonal lattice with box length $a = 1$ and height $c = \sqrt{3}/2$. As scattering potential we used

$$\Phi(r) = 100 (r_{\text{cut}}^2 - r^2)^2, \quad (1.17)$$

where $r = |\mathbf{r}|$ and the cutoff $r_{\text{cut}} = (a - 0.025)/2$. As for the pendulum we have employed the Forest-Ruth algorithm to integrate the equations of motion as well as the linearized equations of motion using the time step $\Delta t = 10^{-3}$. We have propagated the system over a time period $\tau = 12.5$.

In Fig. 1.5 three different single trajectories are plotted which differ significantly in the chaotic behavior. The stable trajectory features an RLI of $\sim 10^{-10}$ and was reached after sampling roughly 300,000 trajectories. The shooting displacement

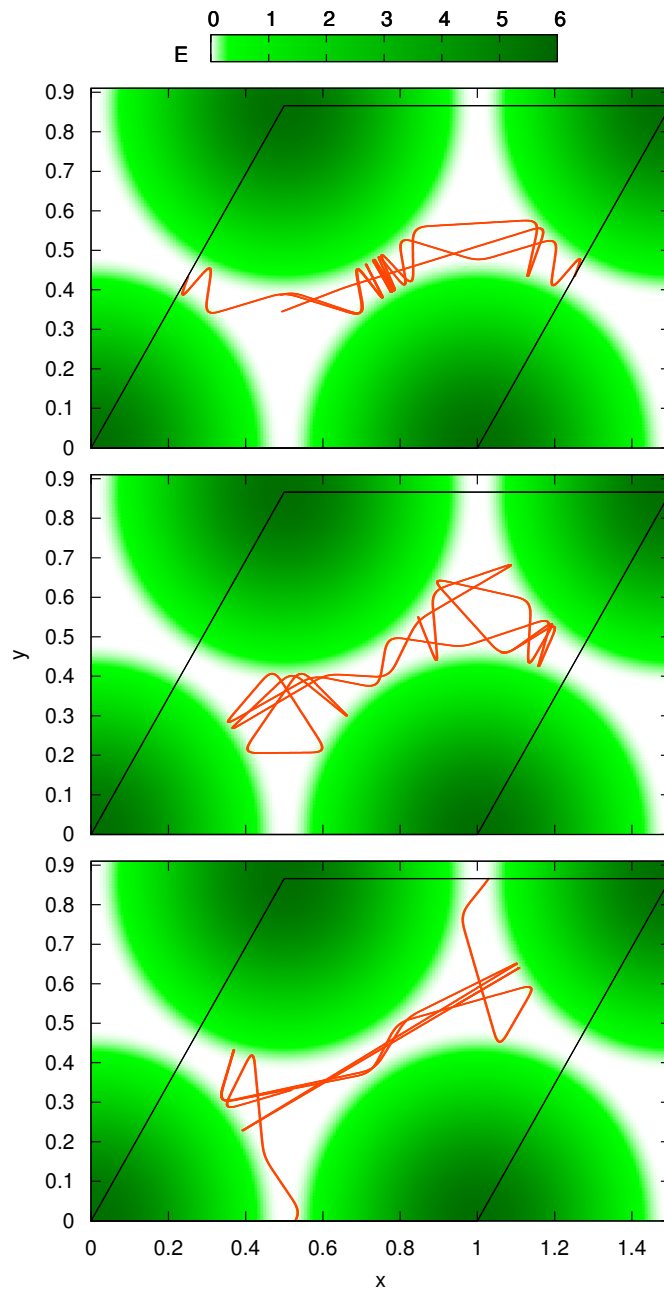


Figure 1.5.: Trajectories of the Lorentz gas: (top) Very chaotic trajectory, (middle) a typical trajectory, sampled with no bias added, (bottom) stable trajectory.

was chosen as $\sigma_G = 10^{-14}$ and $\alpha = -10^9$. The chaotic trajectory was harvested after about 250,000 iteration steps of our TPS procedure. Here, the parameters are $\sigma_G = 10^{-6}$ and $\alpha = 500$ leading to an RLI of ~ 0.3 . It seems that mainly the number of collisions a trajectory is exposed to determines the degree of chaos. So, in the chaotic case the particle bounces with a high frequency within the narrowest corridor of the scatterer, while in the stable case this corridor is freely passed.

1.6.4. Fermi-Pasta-Ulam chain

As an example of a system with higher dimensionality, we search for particularly stable trajectories of the Fermi-Pasta-Ulam (FPU) chain, originally concocted to study the thermalization of oscillatory modes in solids [30, 31]. This model consists of a one-dimensional chain of N point particles with mass m located at positions x_i . The particles are coupled by harmonic springs to which a weak anharmonic part in form of a quartic potential is added leading to the Hamiltonian

$$\mathcal{H} = \sum_i \frac{p_i^2}{2m} + \sum_i \frac{k}{2}(x_{i+1} - x_i)^2 + \frac{\beta}{4}(x_{i+1} - x_i)^4. \quad (1.18)$$

Here, k is the spring constant of the harmonic spring and β is a parameter controlling the strength of the quartic potential. Below, we use units in which $m = 1$, $k = 1$ and consider the case $\beta = 0.1$ with fixed boundary conditions.

Depending on initial conditions, the FPU-chain displays different types of motion. Starting from a state in which all the energy is concentrated in a high frequency mode, the system evolves into a so-called breather moving chaotically with the energy strongly localized in space before equilibration eventually sets in on very long time scales [32]. Other initial conditions lead to only weakly chaotic solitonic modes, in which a kink moves through the system with constant speed and a preserved shape of its sharp front [31, 33]. Here, we use our algorithm to find these weakly chaotic solitons by using a parameter $\alpha = -5 \times 10^8$ highly favoring regular trajectories. Note that this strongly negative value of α was necessary since chaos in the FPU-chain in this regime is very weak and it is difficult to distinguish between more and less chaotic trajectories. Particle traces for a system of $N = 32$ particles at a total energy of $E = 32$ are shown in Fig. 1.6. The equations of motion were integrated with a time step of $\Delta t = 0.05$ for trajectories of length $\tau = 5000$. The trajectory shown in Fig. 1.6 was obtained after a couple of thousand iterations of the path sampling scheme with shooting displacements in momentum space of magnitude $\sigma_G = 0.5$.

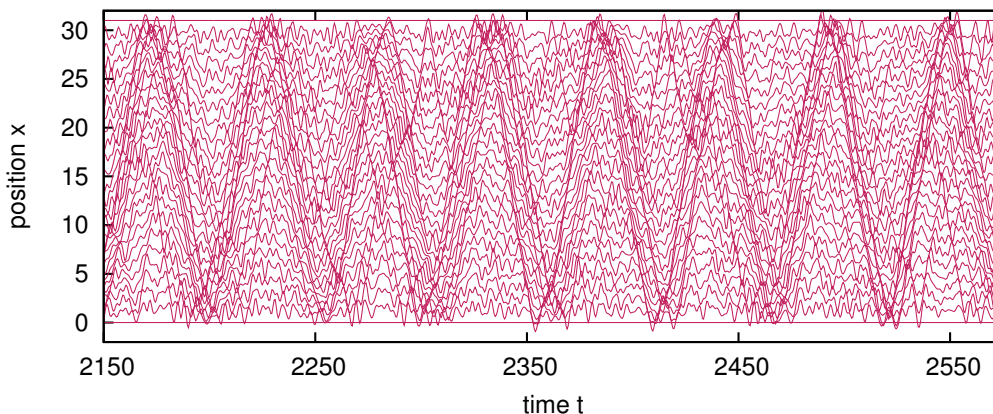


Figure 1.6.: Particle positions of a FPU-chain with $N = 32$ as a function of time along part of a trajectory sampled by the Lyapunov weighted path sampling algorithm. Particle positions have been displaced vertically for better visibility. The trajectory was obtained after a couple of thousand iterations with $\alpha = -5 \times 10^8$ favoring particularly stable trajectories.

Kinks wandering through the chain at constant velocity and bouncing back and forth between the chain ends are clearly visible, indicating a solitonic mode of motion.

1.6.5. Double well system

To test whether Lyapunov biased path sampling can be used to find reactive trajectories in systems with multiple stable states separated by barriers, we have studied a simple double well system in one dimension. The dynamics of the system is governed by the Hamiltonian

$$H(x, p) = \frac{p^2}{2m} + k(x^2 - 1)^2, \quad (1.19)$$

corresponding to a particle of mass m moving on a energy surface with minima at $x = \pm 1$ and a maximum at the origin. The potential energy barrier separating the two stable states has a height of k . We imagine that the system is in contact with a heat bath with temperature T , such that the distribution of initial conditions of the trajectories is canonical, $\rho(x, p) \propto \exp\{-\beta H(x, p)\}$. Here, $\beta = 1/k_B T$ is the reciprocal temperature and k_B is the Boltzmann constant. Thus, all initial conditions of the system are in principle accessible in this ensemble, albeit with different statis-

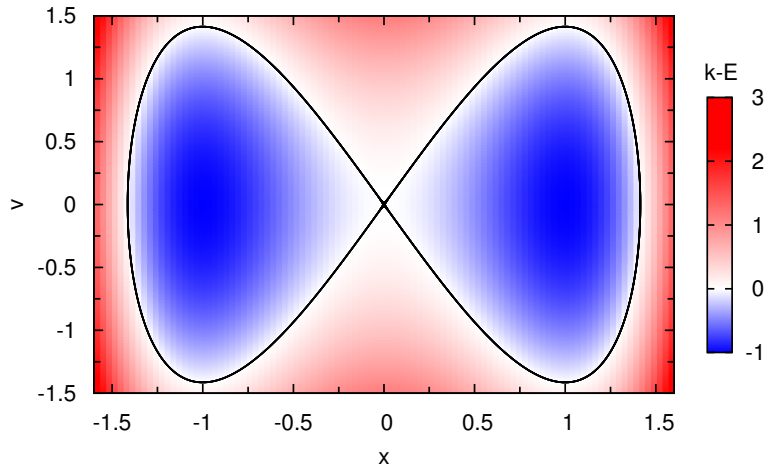


Figure 1.7.: Phase space plots of a particularly chaotic trajectory crossing the saddle point in the double well system. Note that at the origin there is a gap between the upper and the lower branch of the periodic trajectory, but the gap is too small to be visible at the scale of the figure. The color code gives the energy difference to the barrier height k .

tical weight. This system is integrable and hence its Lyapunov exponent vanishes. Nevertheless, finite length trajectories diverge strongly near the barrier top.

Although a canonical distribution of initial conditions implies a coupling of the dynamics to the degrees of freedom of the heat bath, we assume that this coupling is so weak that it does not affect the dynamics of the system on the time scale of the length τ of the trajectories. Hence, each individual trajectory evolves at constant total energy. Under these conditions, the acceptance probability of the path sampling procedure is given by

$$p_{\text{acc}} = \min \left\{ 1, e^{\alpha\tau[R(n,\tau)-R(o,\tau)]} e^{-\beta[H(n)-H(o)]} \right\}, \quad (1.20)$$

where $H(n)$ and $H(o)$ are the energies of the new and the old trajectories, respectively, and $R(n, \tau)$ and $R(o, \tau)$ are the respective RLIs. The above acceptance probability takes into account possible energy changes due to the momentum perturbation applied at the shooting point.

Since we are interested in reactive trajectories that cross the energetic barrier between the stable states and the phase space structures near saddle points which lie at origin of chaos [1], we sample the Lyapunov weighted path ensemble procedure

with a large value of $\alpha = 5 \times 10^8$ strongly favoring chaotic trajectories. The equations of motion are integrated with a time step of $\Delta t = 10^{-2}$ and trajectories have a total temporal length of $\tau = 10^2$. Units were chosen such that $m = 1$ and $k = 1$ and the temperature was set to $\beta = 1$. The magnitude of the shooting displacement to the momenta was $\sigma_G = 0.05$. Starting from a trajectory of energy $E = 0.05$ oscillating about the bottom of one well, after a few hundred path sampling steps reactive trajectories connecting the two wells were obtained. The phase space plot of a reactive trajectory with total energy $E = 1.0000019$ (just slightly above the barrier height of $k = 1.0$) crossing the barrier in close proximity of the saddle point is shown in Fig. 1.7.

1.6.6. Double well dimer in a solvent

As exemplified by the results of the previous section, the dynamical character of pathways crossing barriers in the vicinity of saddle points in the potential energy surface strongly differ from that of trajectories fluctuating around minima [3]. Such pathways connecting stable states are, for instance, relevant in the context of activated chemical reactions and there is intense interest in computational methods for finding such rare barrier crossing pathways along which chemical reactions occurs [9]. In this section we will study if the Lyapunov weighted path sampling method can be used to identify reactive trajectories based on their chaoticity. In particular, we will address the question whether such an approach can be successful for reactions occurring in solution, where the chaoticity of the reactive subsystem may be overshadowed by that of the solvent.

We study this issue using a simple two-state model dimer embedded in a soft-sphere solvent [34, 35]. This three-dimensional model consists of N particles of mass m evolving according to Hamilton's equations of motion in a cubic box of volume V and periodic boundary conditions. All particles interact pairwise via the purely repulsive Weeks-Chandler-Andersen (WCA) potential [36],

$$V_{\text{WCA}}(r) = \begin{cases} 4\varepsilon \left[\left(\frac{\sigma}{r}\right)^{12} - \left(\frac{\sigma}{r}\right)^6 \right] + \varepsilon & \text{for } r \leq r_c, \\ 0 & \text{for } r > r_c. \end{cases} \quad (1.21)$$

Here, r is the interparticle distance, σ is the interaction radius, ε is the strength of the potential, and $r_c = 2^{1/6}\sigma$ is the cutoff radius. In addition, the two particles

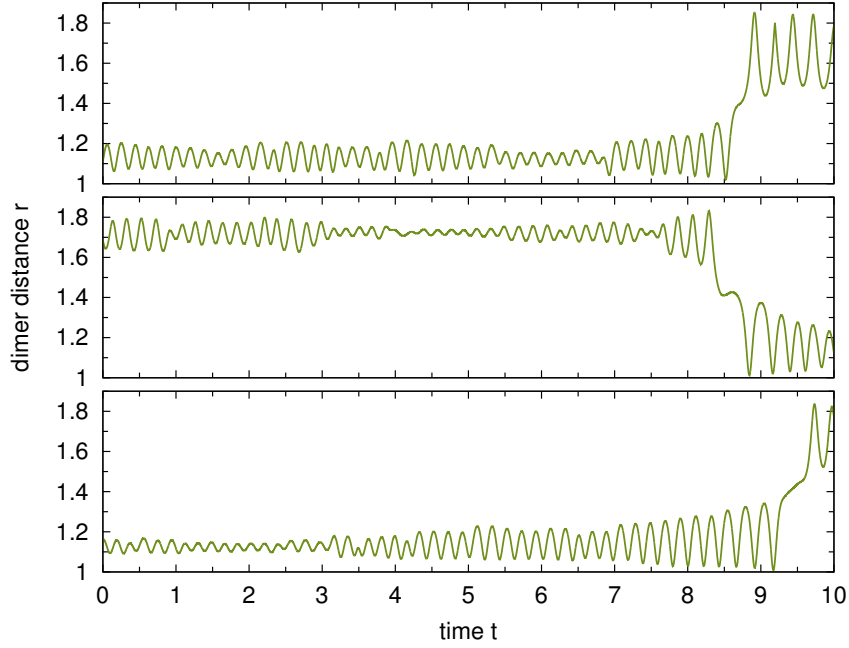


Figure 1.8.: Interatomic distance r of the double well dimer as a function of time t along reactive trajectories found by the Lyapunov weighted path sampling procedure for particle numbers $N = 22$ (top), $N = 32$ (center), and $N = 108$ (bottom). In all three trajectories a transition between the contact and the extended state occurs as evidenced by the sudden change of r towards the end of the trajectory.

forming the dimer are bonded through the double well potential

$$V_{\text{dw}}(r) = h \left[1 - \frac{(r - r_c - w)^2}{w^2} \right]^2, \quad (1.22)$$

where h and w are constants determining the height and the width of the barrier, respectively. The distance between the two minima of the double well potential is $2w$. For low temperatures, i.e., for $h \gg k_B T$, the dimer mainly exists in two states. In one state, the contact state, the interatomic distance of the dimer fluctuates about r_c . In the other state, the extended state, the dimer has a bond length of about $r_c + 2w$. Thermally activated transitions between these two states occur very rarely and are separated by long permanence times in the wells.

In all our simulations we use reduced units in which $\sigma = 1$, $\varepsilon = 1$, and $m = 1$. We

study this system for particle numbers $N = 22$, $N = 32$ and $N = 108$ at a density of $\rho = N/V = 0.5$ and at a total energy per particle of $E/N = 1.0$ corresponding to a temperature of about $T = 0.55$. The dimer barrier height was set to $h = 6.0$ and its width to $w = 0.3$. Trajectories of total length $\tau = 10$ were integrated with a time step of $\Delta t = 10^{-3}$. In the path sampling procedure, different parameters α and different magnitudes σ_G of the shooting displacements were used. While for the smallest system $\alpha = 170$ and $\sigma_G = 0.2$ were employed, we chose $\alpha = 160$ and $\sigma_G = 0.25$ for the system of intermediate size and $\alpha = 600$ and $\sigma_G = 0.05$ for the largest system. Starting from non-reactive trajectories, the Lyapunov weighted path sampling algorithm carried out with these parameters succeeded in finding reactive trajectory. Examples of the interatomic distance as a function of time are shown in Fig. 1.8 along reactive trajectories for various system sizes. While for all system sizes studied here the Lyapunov weighted path sampling simulation converged towards reactive trajectories, the number of iterations before observing the first reactive path increased with system size. While for particle number $N = 22$ the first reactive event occurred after about 400 path sampling steps, the first reactive trajectory was found after 1000 iterations for $N = 32$ and after 2900 iterations for $N = 108$. These results indicate that the pronounced chaoticity of barrier crossing trajectories can be used to identify reactive pathways even for systems with hundreds of degrees of freedom. Note, however, that not all reactive trajectories are strongly chaotic. During our simulations it happened repeatedly that reactive pathways were rejected because their relative Lyapunov indicators were too small. Along these trajectories the chaoticity associated with the saddle point crossing is apparently compensated by a particularly stable dynamics of the solvent.

1.7. Conclusions

In this chapter, we have presented a flexible numerical method to find particularly chaotic or regular trajectories in dynamical systems. The basic idea of the method, inspired by the work of Tailleur and Kurchan [5] and called Lyapunov weighted path sampling, is to first define an ensemble of trajectories weighted by a measure of their chaoticity, for instance their finite time Lyapunov exponent. In this trajectory ensemble a parameter, which can be viewed as conjugate to the Lyapunov exponent, can be tuned to favor either very chaotic or very regular trajectories. The trajectory ensemble is then sampled with methods adopted from transition path sampling.

Other chaoticity indicators besides finite time Lyapunov exponents can be easily integrated into the algorithm as well. Since the calculation of finite time Lyapunov exponents can be computationally demanding, we have, for instance, used *relative Lyapunov indicators* (RLI) to bias trajectories according to their level of chaos. These indicators are particularly sensitive and are capable of distinguishing weakly chaotic trajectories from regular ones. While in this paper we have used Lyapunov weighted path sampling to study only systems evolving deterministically, the method can be applied as easily to stochastic dynamics provided an appropriate chaoticity indicator is available.

The complexity of the examples studied here ranges from a simple one-dimensional double well system to the FPU-model and a bistable dimer in a solvent with hundreds of degrees of freedom. In all cases, the Lyapunov weighted path sampling algorithm successfully identified trajectories with atypical chaoticity properties. While for the FPU-model we used Lyapunov weighted path sampling to find weakly chaotic solitonic modes of motion, we concentrated on highly chaotic trajectories for the dimer in solution. The results obtained for this simple model of a chemical reaction indicate that it is possible to use Lyapunov weighted path sampling to find rare reactive trajectories that pass through saddle points in the potential energy surface as they connect long-lived stable states with each other. Further studies will be necessary to clarify to which degree identifying such trajectories is made difficult by the chaos arising from degrees of freedom not directly coupled to the reaction (for instance solvent degrees of freedom) and possibly eclipsing the dynamical instability of the reactive subsystem.

It will also be interesting to investigate whether chaoticity indicators such as the maximum Lyapunov exponent, the Kolmogorov-Sinai entropy or the relative Lyapunov indicators used in the present study correlate with the measures of mobility used by Chandler and collaborators to link the glass transition with a first order phase transition in trajectory space [12]. In their work, these authors started from the equilibrium distribution of pathways and added to it a bias that favors trajectories with low dynamical activity. Chandler and coworkers demonstrated numerically that this transition displays all the features of a first-order transition occurring in trajectory space. It would be interesting to study if an analogous bias based on chaoticity indicators also leads to an equivalent first order transition in path space. In such research it may be fruitful to combine Lyapunov weighted path sampling with advanced equilibrium simulation methods such as umbrella sampling [37], metady-

namics [38], or parallel replica sampling [39] directly acting on chaoticity indicators.

Chapter 2.

Structure detection using neural networks

The accurate identification and classification of local ordered and disordered structures is an important task in atomistic computer simulations. Here, we demonstrate that properly trained artificial neural networks can be used for this purpose. Based on a neural network approach recently developed for the calculation of energies and forces, the proposed method recognizes local atomic arrangements from a set of symmetry functions that characterize the environment around a given atom. The algorithm is simple and flexible and it does not rely on the definition of reference frame. Using the Lennard-Jones system as illustrative example, we show that the neural networks developed here detect amorphous and crystalline structures with high accuracy even in the case of complex atomic arrangements, for which conventional structure detection approaches are unreliable. *

*The main part of this chapter has been submitted as an article to the *Journal of Chemical Physics* with the title "Neural networks for local structure detection in polymorphic systems".

2.1. The problem of detecting local structures

Atomistic simulations carried out on high performance computers provide a wealth of detailed information on condensed matter processes. While visualization of these processes using computer graphics can yield important insights and stimulate our imagination, a true understanding of the underlying physical mechanisms requires a quantitative and automated analysis of the generated data. Such an analysis often involves the detection of particular atomistic structures based on their local environment. In the simulation of the crystallization of a supercooled liquid, for instance, it is necessary to differentiate between atoms that are part of the growing crystal and atoms that belong to the liquid. Similarly, in studying the microscopic mechanism of structural phase transitions it is crucial to be able to tell apart different crystal structures on a local level. Also when one investigates the structure and dynamics of defects in solids it is necessary to recognize particular atomic arrangements and to follow their motion in time.

The ability to distinguish and classify local atomistic structure is not only important to analyze the output of computer simulation a posteriori, but also to steer computer simulations towards interesting regions of configuration space using biasing schemes such as umbrella sampling [37, 40] or metadynamics [38] and to define long-lived states in path sampling simulations [41, 42]. Furthermore, automatic local structure detection schemes are also useful for the analysis of experimental data obtained with high resolution imaging techniques [43].

Computational methods for structure recognition are usually formulated in terms of order parameters that, ideally, satisfy several important criteria:

- (a) For a given phase, the order parameter should include all configurations belonging to that phase and exclude all others (avoiding mis-assignments is particularly important, if the order parameter is used to drive a transition).
- (b) Structures should be assigned accurately not only in a perfect crystal, but also in the presence of thermal fluctuations or mechanical distortions.
- (c) The order parameter should be local with a well defined and controllable sensitivity region.
- (d) The order parameter should be able to distinguish all stable and metastable phases of a material over a wide range of conditions across the phase diagram.

- (e) The method should recognize defect structures, for instance arising from imperfect crystallization, and structures forming at surfaces and interfaces.
- (f) The order parameter should be invariant with respect to global rotations and translations as well as to permutations of identical atoms.
- (g) The method should be flexible such that it can be easily adapted to work for other substances or unexpected phases.
- (h) Finally, the method should be computationally inexpensive and easy to implement.

During the past decades several computational approaches have been developed for automatic structure detection, which fulfill some but not all of the criteria specified above. In the *common neighbor analysis* (CNA) method, originally developed to distinguish emerging structures in freezing Lennard-Jones clusters [44] and later used to detect crystalline regions as well as defects in various systems [45, 46], local structures of individual atoms are assigned based on an analysis of the environment shared by neighboring atoms. In the *centro-symmetric deviation* method (CSD), introduced to study the nucleation and motion of dislocations in centro-symmetric materials such as fcc-metals [47], the local distortion caused by defects is assessed by computing a parameter sensitive to the angle formed by opposite bond vectors. A similar, but more general approach is followed in the *bond angle distribution* (BAD) method, in which the distribution of angles formed by nearest neighbor bonds is used as characteristic feature to distinguish different crystal structures [48]. The most versatile (and currently most popular) class of methods for local structure recognition are, however, based on the Steinhardt local bond order parameters [49–52]. In this approach, explained in more detail later in this thesis, the particular symmetries of local structures are picked up by combinations of spherical harmonics that are made invariant against rotations, translations and permutations of identical particles and serve as characteristic structural fingerprints for different ordered and disordered structures.

While the methods mentioned in the previous paragraph have been successfully applied to a variety of problems, they often yield unreliable results particularly for complex open structures and in the presence of elastic deformations and thermal fluctuations. For instance, it is notoriously difficult to distinguish local configurations of liquid water and of the various forms of crystalline and amorphous ice [53].

The ability to do that, however, is needed to study the nucleation of ice in supercooled water. As discussed by Brukhno et al. [54], standard Steinhardt bond order parameters are ineffective in detecting hexagonal and cubic ice because oxygens with different tetrahedral hydrogen bonding pattern occur. To resolve this issue, these authors have introduced the maximum projection method, which is capable of distinguishing between liquid water and hexagonal and cubic ice, albeit at the price of introducing a preferred direction and thus breaking rotational invariance. To remedy this situation, Reinhardt et al. [55] suggested a parameter based on particular Steinhardt bond order parameters and used it to drive nucleation of ice in supercooled water. In these simulations it proved necessary to explicitly remove unphysical chain structures that were forced on the system by a bias on the order parameter. Another order parameter to distinguish liquid water from hexagonal and cubic ice was developed by Chau and Hardwick [56, 57] based on detecting local tetrahedral structures. None of the order parameters developed so far for water and ice, however, are capable of discriminating between all phases of ice and liquid water.

In this thesis, we treat the assignment of local structures as a pattern recognition problem that can be addressed with machine learning algorithms. We show how an appropriately trained neural network can be used to accurately detect local ordered structures and demonstrate the practical applicability of the algorithm by distinguishing the different phases of the Lennard-Jones system and of water in a broad range of conditions. Our approach is inspired by the neural network based method for representing potential energy surfaces for condensed matter systems recently developed by Behler and Parrinello [58, 59]. In this method, the total energy of the system is written as a sum of local contributions, each of which is determined by applying a neural network to a set of numbers characterising the local environment of individual atoms. The structural fingerprints used as input for the neural are provided by a collection of symmetry functions that are sensitive to distances and angles in a small region around the central atom and are furthermore invariant with respect to rotations, translations and permutations. In our neural network for structure recognition, we use similar symmetry functions but they are sensitive only to the positions of the atoms in a small and well defined region around a given particle. When properly trained using configurations with known structures, the neural network succeeds in recognizing structures even in polymorphic systems with rich phase diagrams, for which conventional structure assignment methods fail. The method

proposed here is flexible and can easily be adapted to a variety of substances.

The remainder of this chapter is organized as follows. In Sec. 2.2 we introduce the method and explain in detail how the neural network is constructed and trained. The neural network is then applied to a test case in Sec. 2.2.5, where we use it to distinguish between the various structures in the Lennard-Jones system and compare the performance of the neural network with that of Steinhardt bond order parameters. Additionally, we apply the neural network to the more challenging problem of distinguishing between the various phases of liquid water and ice over wide range of pressures and temperatures in Chapter 4 in the second part of this thesis. Using the neural network, we compute the free energy for the nucleation of an ice crystal in supercooled water. Subsequent to this application a discussion of the strengths and weaknesses of the method is provided in Sec. 4.6.

2.2. Neural network for structure recognition

Our approach for assigning local structures is based on the *neural network* method for energy and force calculations recently put forward by Behler and Parrinello [58, 59]. In this method, which provides the accuracy of density functional theory at a fraction of its cost, the total energy of the system is expressed as a sum of contributions from local regions centered around individual atoms. Each region is characterized by a set of generalized coordinates, called symmetry functions, which are functions of the atomic coordinates and serve as input for a feed-forward neural network. Based on these structural fingerprints, the neural network then predicts the local energy contribution of each atom, essentially by interpolation. Here, we adopt this approach and use the information encoded in the symmetry functions to detect local atomic structures. In the following sections, we first describe the neural network, then discuss the definition of the symmetry functions, which are designed to be sensitive to the local environment of a given atom, and finally explain how the neural network is trained.

2.2.1. Feed-forward neural network

A neural network can be viewed as a complex non-linear (scalar- or vector-valued) function that depends on a set of input variables and a possibly very large set of parameters, which can be tuned to obtain the desired behavior. Inspired by systems

of biological neurons such as the brain, the basic concept of a neural network is depicted in Fig. 2.1. A feed-forward network such as the one used in our work consists of three parts: The input neurons, one or more calculation layers and the output nodes. The input interface receives the external information and corresponds to the part of a biological neural network in which sensory stimuli are converted into signals. The information is then passed to the calculation layers, where the input signals are weighted and processed. The last part of the neural network is the output interface, where the final data processing step occurs and the information is converted into the desired output form. The size and topology of a neural network is specified using the notation $I \times H \times H \times O$, where I , H , and O denote the number of nodes in the input, hidden and output layers, respectively.

Based on this network topology, the structure recognition works as follows. Consider a given system configuration $r = \{r_1, r_2, \dots, r_N\}$ consisting of the Cartesian coordinates of all N atoms. For simplicity we assume that there is only one atom species in the system, but we emphasize that the method can easily be generalized to more atoms species. To determine the local structure around atom i one first computes a set of I symmetry functions $\{G_l^{[i]}(r)\}$, which depend on the Cartesian coordinates of the atoms in the vicinity of atom i . The symmetry functions, explained in detail below, are designed to characterize the local environment of a given atom. The symmetry functions are then turned over to the first layer where for each of the neurons of this layer a weighted sum, $\sum_l w_{ml}^{(1)} G_l$, over the input (i.e., the symmetry functions) is computed. Here, the synaptic weight $w_{ml}^{(1)}$ connects the input neuron l with the neuron m of the first hidden layer, which has H neurons. Each sum is then shifted by a bias (or threshold) $b_m^{(1)}$ and then passed through an activation function $\varphi(x)$, thus yielding the output of the first hidden layer of neurons,

$$a_m^{(1)} = \varphi \left(\sum_{l=1}^I w_{ml}^{(1)} G_l + b_m^{(1)} \right). \quad (2.1)$$

The output of the first hidden layer is then propagated to the second hidden layer and processed in a similar way using the weights $w_{nm}^{(2)}$ and biases $b_n^{(2)}$,

$$a_n^{(2)} = \varphi \left(\sum_{m=1}^H w_{nm}^{(2)} a_m^{(1)} + b_n^{(2)} \right). \quad (2.2)$$

Finally, the output of the neural network, given in form of the vector

$$y = \{y_1, y_2, \dots, y_O\}$$

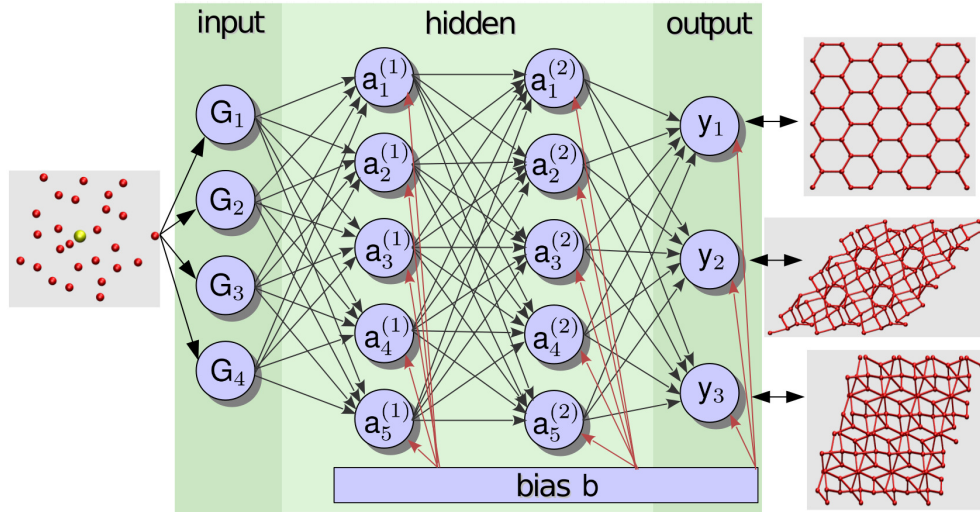


Figure 2.1.: Four layer feed-forward neural network with $I \times H \times H \times O$ topology for local structure identification. Here, I , H , and O refer to the number of neurons in the input layer, the hidden layers and the output layer, respectively. For a given configuration r , depicted schematically on the left hand side with the central atom shown in yellow, a set of symmetry functions $\{G_l(r)\}$ is computed. These symmetry function serve as input for the first layer of the neural network, from which the data are passed to the hidden layers. Each neuron, or node, in the calculation layers takes the values of the neurons of the previous layer, as indicate by the black arrows, and performs a weighted sum over them. The weights, assigned during the training phase, define the relative importance of the connections between neuron pairs. After the sum is formed, a bias is added to the value of each neuron as indicated by the red arrows. Also the bias values are determined during the training of the network. For each node, the result is then fed into an activation function, which determines how active a neuron is, i.e., how much it contributes to the output. Finally, the output layer converts the processed information into a vector in which each component signals the occurrence of one of the possible structures.

of O components, is obtained by carrying out another set of weighted sums, shifting them by the biases $b_p^{(3)}$ and feeding the results into the activation function $\tilde{\varphi}$,

$$y_p = \tilde{\varphi} \left(\sum_{n=1}^H w_{pn}^{(3)} a_n^{(2)} + b_p^{(3)} \right). \quad (2.3)$$

While we use the hyperbolic tangent as activation function for all neurons in the hidden layer, $\varphi(x) = \tanh(x)$, the identity function $\tilde{\varphi}(x) = x$ is employed as a activation function for the output neurons. This choice of activation functions was found to work well in the case of the neural networks for energy computation [60]. The output vector y has one component for each of the O possible structures the network is trained to recognize. If the network detects structure i , component y_i is large, while all another components are small. The complete action of the neural network on the symmetry functions G_l can be written as

$$y_p = \tilde{\varphi} \left(\sum_n w_{pn}^{(3)} \varphi \left(\sum_m w_{nm}^{(2)} \varphi \left(\sum_l w_{ml}^{(1)} G_l + b_m^{(1)} \right) + b_n^{(2)} \right) + b_p^{(3)} \right). \quad (2.4)$$

Due to the form of the activation function $\varphi(x)$, the output values y_p of the neural network depend on the input G_l in a complex non-linear way. The large number of weights and biases provides the neural network with the flexibility required to reproduce with high accuracy a given functional dependence of the output from the input. In the training phase, carried out as explained below, the weights and biases are adjusted such that the neural network correctly classifies the training set consisting of configurations with known structures.

2.2.2. Symmetry functions

The information about the spatial arrangement of the atoms within a certain cutoff of a given atom i is encoded in the so-called symmetry functions $\{G_l^{[i]}(r)\}$, which depend on the Cartesian coordinates of the atoms in this region. The functions, which are constructed to be invariant with respect to rotations, translations and the permutation of identical atoms, need to be defined carefully such that they carry sufficient details to reliably detect and classify structures. By tuning the parameters of these functions, they can be made sensitive to the various symmetries the environment of atom i can have. The following types of symmetry-functions have been proven sufficient for accurate structure detection in the two test cases

studied in this work:

$$G_1^{[i]}(r) = \sum_{j \neq i} f_c(R_{ij}), \quad (2.5)$$

$$G_2^{[i]}(r) = \sum_{j \neq i} e^{-\eta(R_{ij}-R_s)^2} f_c(R_{ij}), \quad (2.6)$$

$$G_3^{[i]}(r) = \sum_{j \neq i} \cos(\kappa R_{ij}) f_c(R_{ij}), \quad (2.7)$$

$$G_4^{[i]}(r) = \frac{1}{2\zeta} \sum_{j,k \neq i} (1 + \lambda \cos \theta_{ijk})^\zeta \\ \times e^{-\eta(R_{ij}^2 + R_{ik}^2 + R_{jk}^2)} f_c(R_{ij}) f_c(R_{ik}) f_c(R_{jk}), \quad (2.8)$$

$$G_5^{[i]}(r) = \frac{1}{2\zeta} \sum_{j,k \neq i} (1 + \lambda \cos \theta_{ijk})^\zeta \\ \times e^{-\eta(R_{ij}^2 + R_{ik}^2)} f_c(R_{ij}) f_c(R_{ik}), \quad (2.9)$$

$$G_6^{[i]}(r) = \frac{1}{2\zeta} \sum_{j,k \neq i} (1 + \lambda \cos \theta_{ijk})^\zeta f_a(R_{ij}) f_a(R_{ik}), \quad (2.10)$$

$$G_7^{[i]}(r) = \frac{1}{2} \sum_{j,k \neq i} \sin[\eta(\theta_{ijk} - \alpha)] f_c(R_{ij}) f_c(R_{ik}), \quad (2.11)$$

$$G_8^{[i]}(r) = \frac{1}{2} \sum_{j,k \neq i} \sin[\eta(\theta_{ijk} - \alpha)] f_b(R_{ij}) f_b(R_{ik}). \quad (2.12)$$

Here, the summation indices run over all neighboring atoms within a certain cutoff of the central atom i . As illustrated in Fig. 2.2, R_{ij} is the distance from particle i to j and θ_{ijk} is the angle spanned by the triplet of atoms i , j , and k . The quantities R_s , α , η , λ , and κ are tunable parameters, which need to be carefully chosen in order to reflect the symmetries characterizing the possible local structures. While symmetry functions $G_1^{[i]}(r)$ to $G_5^{[i]}(r)$ were adopted from Ref. [61], where they were introduced for energy calculation, we developed functions $G_6^{[i]}(r)$ to $G_8^{[i]}(r)$ specifically for structure recognition.

Since one usually wants to detect structures in the immediate surrounding of a given atom, it is important that the symmetry functions are only sensitive to atomic position in a small and well defined region. We therefore use cutoff functions that are sharper than the soft cosine-cutoff used in neural networks for energy calculations

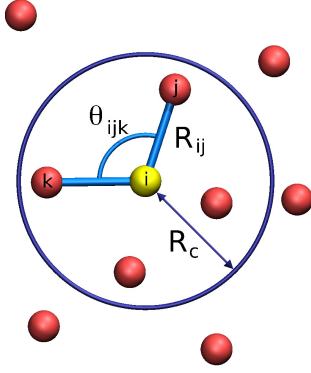


Figure 2.2.: The symmetry functions $G_i^{[i]}(r)$ around atom i , shown in yellow, are constructed using combinations of atomic distances R_{ij} and angles θ_{ijk} . Only atoms within a certain cutoff R_c contribute to the symmetry functions of the region centered around atom i .

[58]. The Fermi cutoff function

$$f_c(R) = \begin{cases} [1 + \exp\{\alpha_c(R - R_c + \epsilon_c)\}]^{-1} & \text{if } R < R_c, \\ 0 & \text{else,} \end{cases} \quad (2.13)$$

is close to unity for small arguments and then decreases from 1 to 0 in an interval of width $1/\alpha_c$ centered at $R_c - \epsilon_c$. In the limit of large values of α_c the cutoff function $f_c(R)$ turns into a step function with the step located at $R_c - \epsilon_c$. In addition, we defined the cutoff functions

$$f_a(R) = \begin{cases} \cos^2[\eta(R - \mu)] & \text{if } \mu - \frac{\pi}{2\eta} < R < \mu + \frac{\pi}{2\eta}, \\ 0 & \text{else,} \end{cases} \quad (2.14)$$

and

$$f_b(R) = \begin{cases} \cos^2[\nu(R - a_l)] & \text{if } a_l - \frac{\pi}{2\nu} < R < a_l, \\ 1 & \text{if } a_l < R < a_r, \\ \cos^2[\nu(R - a_r)] & \text{if } a_r < R < a_r + \frac{\pi}{2\nu} \\ 0 & \text{else,} \end{cases} \quad (2.15)$$

which are used in the angular symmetry functions $G_6^{[i]}(r)$ and $G_8^{[i]}(r)$. Here, η , μ , ν , a_l and a_r are free parameters that can be adjusted to make the cutoff functions sensitive only to specific distance ranges. Some symmetry functions with typical parameters are shown in Fig. 2.3.

For the neural network to work accurately, the parameters of the symmetry functions need be selected such that the symmetry functions carry a maximum amount of structural information about the environment of a given atom. To select appropriate

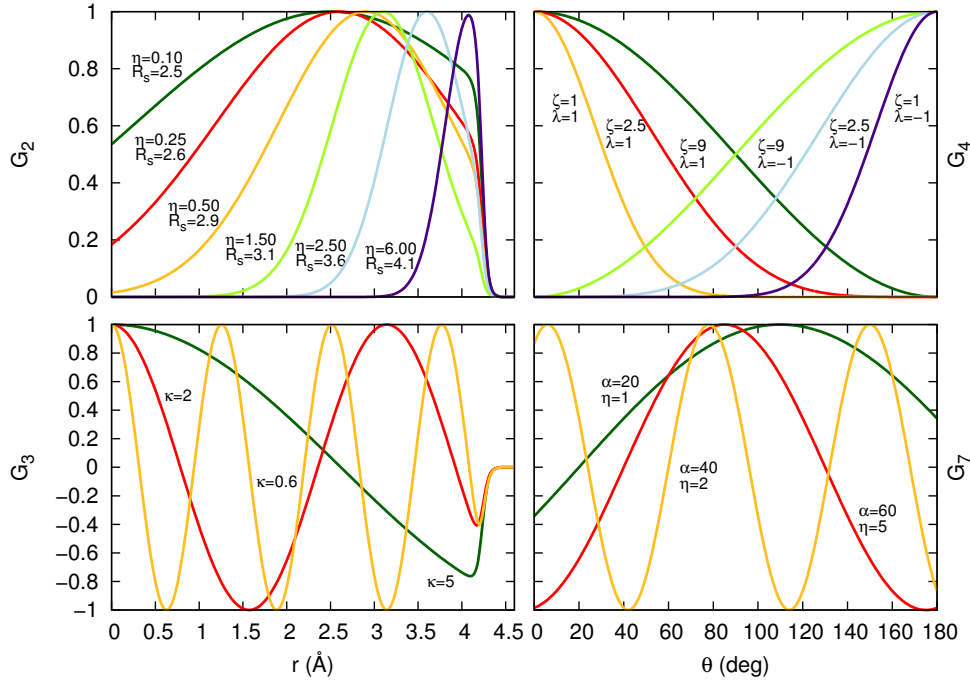


Figure 2.3.: Various symmetry functions with typical parameter values. The two left panels show the distance dependence of the terms in the two purely radial symmetry functions G_2 and G_3 . The two panels on the right side show the angular parts of G_4 and G_7 . The cutoff function parameters $\epsilon_c = 0.2$, $\alpha_c = 30$ and $R_c = 4.43352$ were used.

parameters while keeping the number of symmetry functions low, we first compute the distribution of many symmetry function candidates for the various phases of interest. Then, for each symmetry function, we determine the overlap between the distributions obtained for the different phases and finally select the symmetry functions which best differentiate between the phases, i.e., those corresponding to small overlaps. The symmetry functions are also scaled to the best working range of the neurons, which is from -1 to 1 for the activation functions used in our work.

From the set of symmetry functions determined in this way it is possible to eliminate redundant information by carrying out a *sensitivity analysis* of the neural network [62–64]. For this purpose, one determines the derivative of the output of the network with respect to its input. A derivative close to zero then indicates that

the corresponding input node has little effect on the output and can be eliminated without compromising the accuracy of the network. Typically, we remove input nodes with a derivative smaller 0.1, % to 1% of the largest value. After the removal of the redundant symmetry functions the neural network needs to be retrained. Using this approach it is possible to reduce the number of symmetry functions required to fully characterize local structures to about 30 – 40.

2.2.3. Training the neural network

Once the symmetry functions are defined, the neural network needs to be trained to recognize and distinguish the desired structures. During the training procedure, the weights and biases are tuned based on the information contained in a training set, which consists of a large number of atomic configurations with known structure. Thus, each entry of the training set \mathcal{T} consists of a configuration r and the corresponding structure vector \tilde{y} ,

$$\mathcal{T} = \left\{ r^{(\tau)}, \tilde{y}^{(\tau)} \right\}, \quad (2.16)$$

where the superscript τ numbers the entries in the training set. The structure vector $\tilde{y}^{(\tau)}$, which corresponds to the output vector of the neural network, encodes the information about the type of structure of configuration $r^{(\tau)}$. If configuration $r^{(\tau)}$ is of structure type p , the component $\tilde{y}_p^{(\tau)}$ of the structure vector is assigned the value $\tilde{y}_p^{(\tau)} = +0.9$ and all other components p' are assigned the value $\tilde{y}_{p'}^{(\tau)} = -0.9$.

The training set can be prepared by running straightforward molecular dynamics (MD) simulations for the various phases and extracting local atomic environments from configurations sampled along the MD trajectories. Assuming that during a particular MD run the system remains in the phase from which the simulation has been started, all atomic arrangements taken from that run can be assigned the same structure. Since in the course of the MD run the system can, in principle, turn into a different phase and change its structure, it is important to verify whether the original structure still exists at the end of the simulation. This can be done by visual inspection or by the calculation of some global order parameter for the entire system. In the unlikely case that a transition to a different phase has occurred, configurations from this simulation should not be included in the training set. To make sure that the training set is sufficiently diverse, training configurations for a particular phase should be sampled from several MD simulations carried out at

different pressures and temperatures. Also, it has proven to be important to avoid correlations between entries in the training set. Thus, local environments extracted from the same trajectory should be significantly separated in time. Typically, the training set comprises tens of thousands of entries. Training sets of this size are necessary to guarantee that most thermal fluctuations typical for each phase are included in the training set.

Based on the information contained in the training set \mathcal{T} , the network is then trained such that for the configurations in the training set the output vectors y of the neural network best match the corresponding structure vectors \tilde{y} . The training procedure can be viewed as an optimization problem, in which the weights $w_{nm}^{(k)}$ and the biases $b_n^{(k)}$ are tuned to minimize the deviation of the predicted structures from the known structures. The target function for the minimization can be expressed as the mean square deviation

$$\chi^2 = \frac{1}{N_{\text{set}}O} \sum_{\tau=1}^{N_{\text{set}}} \sum_{p=1}^O \left[y_p(r^{(\tau)}) - \tilde{y}_p^{(\tau)} \right]^2, \quad (2.17)$$

where the sum over the index τ runs over all N_{set} entries of the training set and $y(r^{(\tau)})$ is the output of the neural network evaluated for structure $r^{(\tau)}$.

We have tested several machine learning methods to minimize χ^2 including *back-propagation* [65] and a nonlinear least squares algorithm [66]. We found, as Behler and Parrinello did [58, 59], that the *extended Kalman filter* (EKF) [67, 68] converges quickly and does not easily get trapped in local minima. This learning method originates from signal processing theory, where it is used to filter out noise of signals, and has been widely and successfully used for neural network training [69–71]. The main idea of the *extended Kalman filter* is to introduce an error covariance matrix, which is then improved iteratively. The iteration is stopped when the mean square deviation χ^2 is sufficiently converged. Finally, the predictive quality of the neural network is tested by computing the mean square deviation between predicted and true structure vectors for an independent test set, typically of size similar to that of the training set. For a detailed discussion of the Kalman filter see Refs. [67, 68].

2.2.4. Implementation details

In implementing the *extended Kalman filtering* method several precautions must be taken to obtain an accurate and robust neural network for structure prediction.

The *Kalman filter* learning technique is an online learning scheme, implying that each basic iteration step, in which one entry of the training set is processed, leads to an update of the entire network state (weights and biases). After the learning procedure has cycled through all entries of the training set, i.e., after on *epoch*, and before the next iteration starts, the order of the entries of the training set is randomly permuted to avoid correlations. The predictive quality of the network can be improved by a modification of the training scheme called *multistreaming* [68]. In this technique, the entries of the training set are bundled into batches consisting of N_{batch} entries each. The *Kalman filter* is then applied to entire batches rather than to individual training set entries. While this method improves the outcome of the training of the *Kalman filter*, it also increases the computational effort required for the training procedure* .

It is well known that the extended Kalman filter method suffers from numerical rounding errors, which may lead to a rapid divergence at some point in the learning procedure. Two common approaches exist to overcome this instability [68]. The first method updates the square root of the error covariance matrix rather than the covariance matrix itself, producing a very robust iteration prescription. Here, we follow a much simpler approach and introduce some artificial noise in form of a constant that is added to all diagonal elements of the error covariance matrix at each iteration. This makes the algorithm not only more stable, but also prevents the networks from getting trapped in local minima of the target function.

To accelerate the training procedure in the starting stage, the initial values of the weights are not assigned at random but are pre-conditioned following an extension of the method proposed in Ref. [72] for neural networks with two hidden layers [73].

* This can be seen by comparing the matrix sizes of the usual EKF with the ones of the multi-stream EKF. Computationally, the most time consuming operations of the usual EKF are the following two operations: the multiplication of a $W \times W$ with a $W \times O$ matrix and of a $W \times O$ with an $O \times W$ matrix. Here W is the number of weights and biases of the network and O the number of output neurons. On the other side, when *multistreaming* is applied then each matrix dimension O is increased by a factor N_{batch} , thus, instead of multiplying a $W \times O$ with an $O \times W$ matrix, the matrix dimensions $W \times (ON_{\text{batch}})$ and $(ON_{\text{batch}}) \times W$ have to be considered.

2.2.5. Application to Lennard-Jones systems

In this section we demonstrate the application of the neural network for structure recognition using the Lennard-Jones system as example.

For the Lennard-Jones system conventional order parameters based on spherical harmonics [49–52] provide an accurate way to distinguish between the liquid and the various crystalline phases. We first apply the neural network approach to this system for comparison. All quantities are given in reduced Lennard-Jones units, i.e., distances are given in units of σ , energies in units of ϵ and time in units of $\sqrt{m\sigma^2/\epsilon}$, where ϵ and σ are the Lennard-Jones parameters and m is the particles mass.

Training set

Depending on temperature and pressure, the Lennard-Jones system can exist in the liquid state as well as several crystalline states including the hexagonal close packed structure (hcp), the face centered cubic structure (fcc), the body centered cubic structure (bcc), and a recently discovered distorted bcc-structure (I-43d) [74]. In order to obtain a neural network that reliably distinguishes between these phases in all regions of the phase diagram where they are at least metastable, a training set including all typical local configurations and the fluctuations around them is required.

In Fig. 2.4 isotherms for the investigated structures are plotted. The main purpose of studying the isotherms is to find the region of stability of a particular phase. Otherwise, one could generate initial configurations of a certain phase, which accidentally transform to another phase during the simulation. To calculate the isotherms we performed simulations in the NVT ensemble and calculated the average pressure for a given temperature and particle density. We plot only phase-space points where no transition to a phase other than the initial one occurred. An exception is bcc, where domain formation as well as transitions into I-43d occur. This mainly happens for lower densities and temperatures and is indicated by the bend of the bcc-isotherm at $\rho \approx 1.04$ for $T = 0.92$ and $\rho \approx 0.95$ for $T = 0.6$. For each isotherm we calculated NVT trajectories of length $\tau = 300$ for 50 different densities.

Following each crystalline phase isotherm to lower densities, the system rapidly melts into a liquid. Liquid Lennard-Jonesium freezes into bcc at increasing densities, whereas for lower densities cavitation takes place (see for example [75]), i.e., the system exhibits either vacuum cavities or gaseous bubbles.

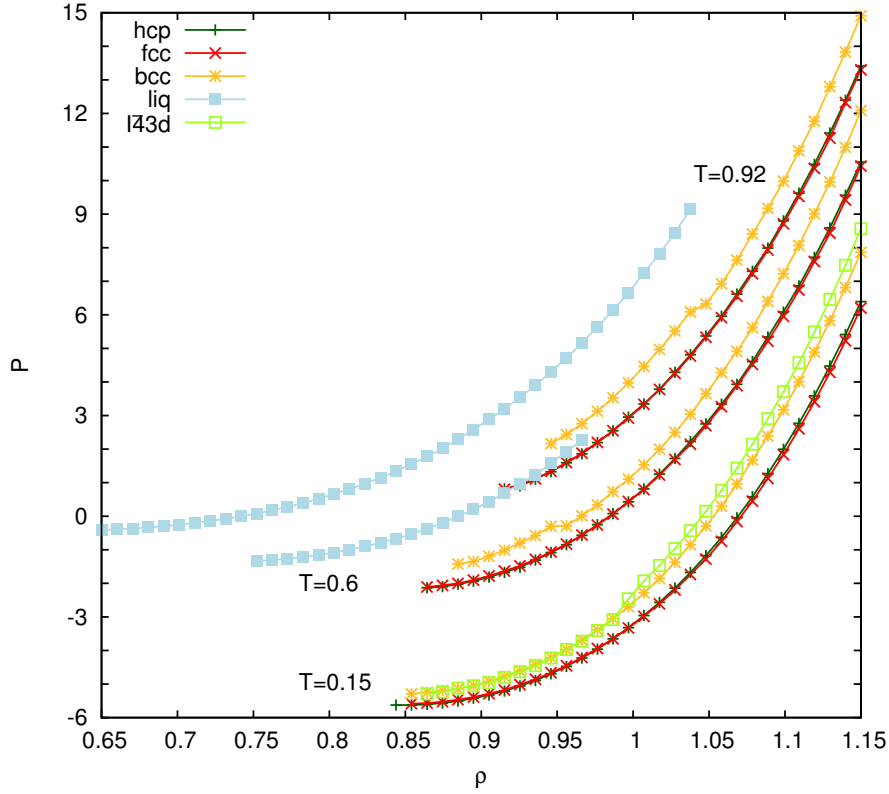


Figure 2.4.: Isotherms for hcp, fcc, bcc, liquid and I-43d structures of Lennard-Jonesium in their region of mechanical stability are plotted for three different temperatures .

For the isotherms at $T = 0.15$ all configurations which were initially in the liquid phase transform rapidly into a crystalline phase. For densities lower than $\rho \approx 1.0$ the pressure at a given density is identical for both bcc and I-43d and a mixture of both phases occurs. Above $\rho \approx 1.0$, a clear separation between the pressures of these phases can be observed.

We have generated the training set by carrying out molecular dynamics simulations for various densities and temperatures both in the NVT and NPT ensembles with periodic boundary conditions and a cutoff of 2.6 for the Lennard-Jones pair interaction. The dynamics of the system was followed with time-reversible integrators using a Nosé Hoover chain thermostat [76, 77] and a time step of $\Delta t = 5 \times 10^{-3}$. In the simulations in the NPT ensemble, we only allowed the rectangular simula-

tion box to fluctuate isotropically, i.e., all box vectors are scaled equally keeping their angle fixed. The system sizes were chosen such that a perfect crystal of the desired structure fits in the simulation box. In particular, these particle numbers are $N_{\text{hcp}} = 1440$, $N_{\text{fcc}} = 1372$, $N_{\text{bcc}} = 1458$, $N_{\text{I-43d}} = 2000$ and $N_{\text{liq}} = 1450$. For each phase, we computed roughly 20 trajectories of length $\tau = 1.5 \times 10^3$ at different pressures and temperatures. To obtain an accurate neural network it has proven particularly important to train the network with information obtained for a broad range of pressures/densities. Here we use configurations obtained at $T = 0.15$ and $T = 0.92$ and pressures ranging from $P = -5$ to $P = 15$.

From these molecular dynamics simulations we picked 30,000 local configuration for each phase and to avoid correlations between them we used only every 100th MD step. From each configuration we extracted only a few local environments to further reduce correlations. Each local environment is then assigned the structure of the simulated phase. The assigned structure is encoded in the structure vector as described in Sec. 2.2. If, for instance, the assigned structure is hcp, the corresponding structure vector is given by $\tilde{y} = \{0.9, -0.9, -0.9, -0.9, -0.9\}$, and other structures correspond to a different positive component. Note that the value of 0.9 rather than 1.0 is selected, because the activation functions of the neural network are normalized to return values in the interval from -1 to 1. In total, the training set includes 150,000 local configurations with respective structure vectors. This particular way of assigning the structure type to the local configurations implicitly assumes that during the entire length of the molecular dynamics simulation there is no phase change, not even locally or transiently. We have verified, both by visual inspection and by monitoring the energy and other quantities, that indeed no phase transitions take place in our simulations. From the same MD simulations we also extracted a test set of 22,000 configurations in total.

Symmetry functions

An accurate neural network for the recognition of local configurations relies on symmetry functions that carry sufficient information on the geometric features of local atomic arrangements. Appropriate symmetry functions can be constructed based on the distributions of distances and angles in the local environment of a given atom as depicted in Fig. 2.5. The positions and widths of the maxima and minima of the radial distributions functions shown in panel (a) guide the selection of the parameters

governing the radial part of the symmetry functions (in particular the symmetry functions of type 2 and 3). For instance, a symmetry function sensitive to particles a distance $R = 1.55$ should provide information to distinguish between hcp and fcc from liquid and bcc. Similarly, symmetry functions responsive to distances of $R = 1.9$ should carry important information because the radial distribution functions of all crystalline phases have a maximum at this position, which is also the distance at which the local environments of fcc and hcp start to differ. The angular distributions of the first and second shell around the central atoms, shown in panels (b) and (c) of Fig. 2.5, supply useful information for the definition of the angular parts of the symmetry functions. In the first shell, angles $\alpha = 115^\circ, 120^\circ$ and 150° appear to be important while in the second shell the angles $\alpha = 50^\circ, 80^\circ, 130^\circ$ and again 115° should be considered. Based on such considerations we have defined a set of 45 symmetry functions designed to detect the geometrical features of the various structures. In practice a sub set of the symmetry functions given in subsection 2.2.2 is sufficient for structure detection. The parameters of these symmetry functions are listed in Tab. 2.1 at the end of this chapter. For the cutoff function given in Eq. (2.13) we have used $\epsilon_c = 0.2\sigma$ and $\alpha_c = 30\sigma^{-1}$.

Neural network training

Based on the training set and the symmetry functions described above, we have determined the weights and bias values for a $45 \times 35 \times 35 \times 5$ network using the Kalman filtering technique. In this learning procedure, which takes a few days of computation time using a highly parallelized CUDA [78] program running on a cluster of GPUs, a total of 3050 parameters are optimised. The number of output nodes is given by the number of phases one would like to distinguish and the number of input nodes is equal to the number of symmetry functions. We selected the number of hidden nodes to be of the same order of the number of input nodes. We have also tried neural networks with different number of hidden layers and a different number of nodes in these layers, but have found that the topology given above results in the most accurate structure prediction.

In the Kalman filtering technique we used for the learning procedure, the parameters of the neural network are adapted iteratively. The iteration is stopped when the root mean square error (RMSE) between the predicted and the target structure vectors does not change by more than a certain threshold in subsequent iterations,

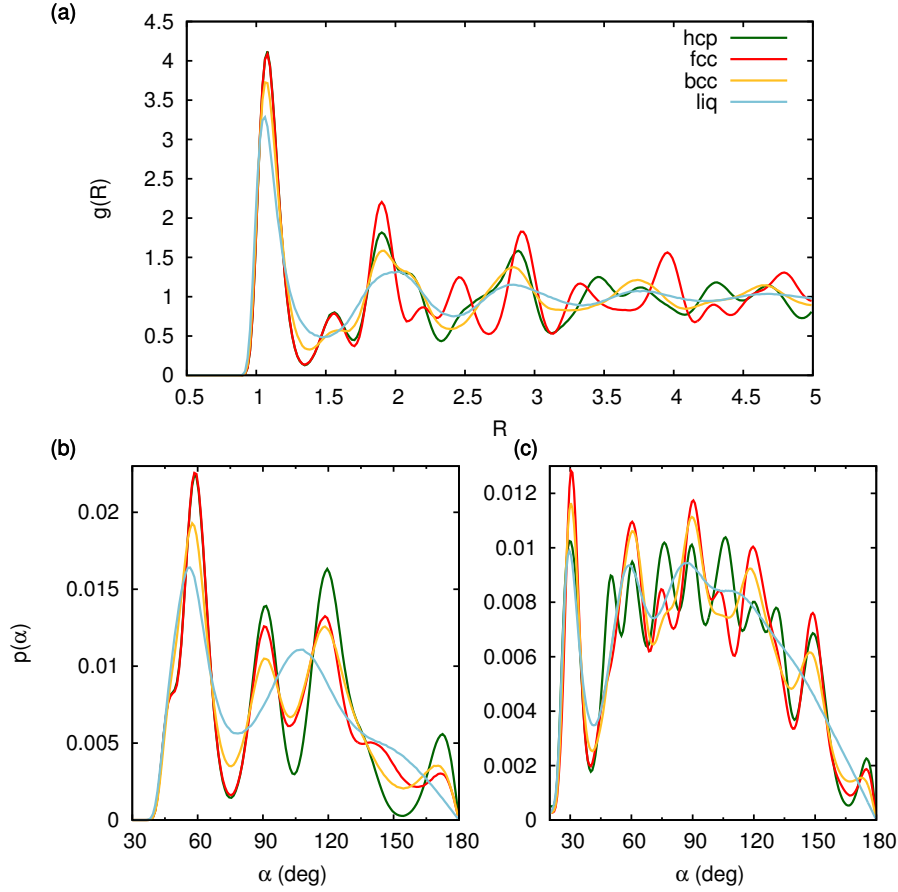


Figure 2.5.: Several spatial distribution functions for different phases of the Lennard-Jones system. (a) Radial distribution functions $g(R)$, (b) angular distribution functions for particles within a cutoff of $R_{\max} = 1.5$, (c) angular distribution functions in the shell with distance between $R_{\min} = 1.5$ and $R_{\max} = 2.42$. Simulations of 3×10^4 equilibration and 3×10^4 production steps were carried out in the NPT ensemble at $T = 0.92$ and $P = 5.68$.

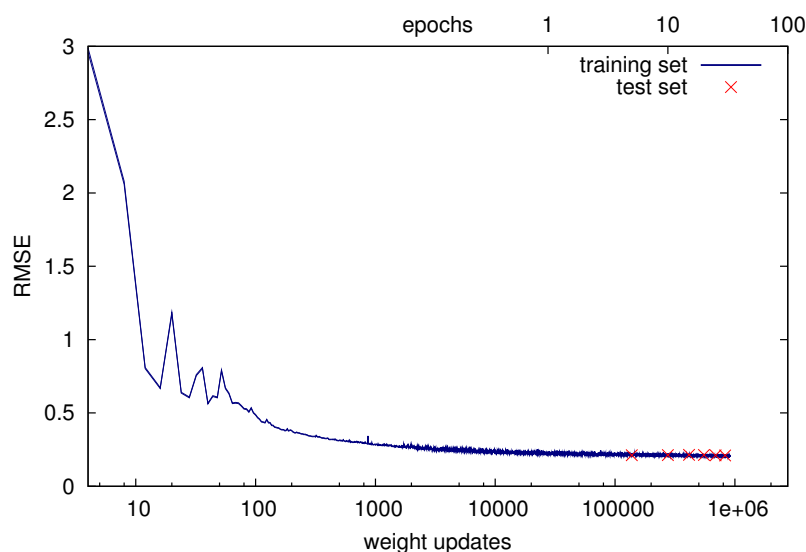


Figure 2.6.: Typical learning curve of a neural network used to detect different phases in the Lennard-Jones system. The root mean square error (RMSE) between the predicted and target structure vectors of the training set (blue curve) and the test set (red crosses) are shown as functions of the number of parameter updates in the Kalman filter learning procedure. The number of epochs, i.e. the number of times the procedure has looped over the entire training set, is displayed on the x -axis at the top.

or epochs, of the Kalman filtering procedure. The iteration is also stopped if overfitting takes place, which may occur if due to the large number of parameters the learning algorithm tries to generate a unique path through the network for each entry in the training set, instead of doing this for a class of entries. One knows that overfitting takes place, if the RMSE of the training set continues to decrease in the course of the iteration while the RMSE for the test set increases. A typical learning curve of the neural network, i.e., the RMSE as a function of the number of parameter updates, is shown in Fig. 2.6. As can be inferred from the figure, the RMSE converges to a finite value rather than to zero due to the selected symmetry functions, which do not contain sufficient information for a perfect structure assignment. The RMSE of the test set and the training set are essentially identical, i.e., no over fitting occurs.

Structure detection

Results for the structure assignment carried out with the neural network for the Lennard-Jones system are shown in Fig. 2.7. The color-coded bars in this figure indicate the fraction of structures that have been assigned a particular type. The colours of the bars indicate to which type a structure is assigned and the labels on the x -axis indicate the phase from which the structure is taken. As can be inferred from the figure, the results obtained for the test set (left) are of the same quality as the results for the training set (right), indicating that no *over-fitting* has occurred in training the network. For all phases, structures are assigned with an accuracy better than 90%. The fraction of misassigned structures is particularly small for structures from the liquid phase and the I-43d phase, while for the hcp and bcc phases a few percent of the structures are assigned the wrong type, probably because at lower densities the local structures can deviate considerably from the perfect crystalline arrangement due to thermal fluctuations.

2.2.6. Comparison to Steinhardt bond order parameters

For comparison, we have also determined local structure types for the Lennard-Jones system using Steinhardt bond order parameters constructed from spherical harmonics [49]. More specifically, we use the bond order parameters \bar{q}_4 and \bar{q}_6 obtained from the Steinhardt bond order parameters q_4 and q_6 by averaging over the first neighbor shell [52] (see below). As shown previously, these order parameters provide a practical and accurate way to distinguish between all phases occurring in the Lennard-Jones system.

Given the distance vectors of the N_b neighbors of particle i , $\{\mathbf{r}_{ij}\}$ we can define the complex vector

$$q_{lm}(i) = \frac{1}{N_b(i)} \sum_{j=1}^{N_b(i)} Y_{lm}(\mathbf{r}_{ij}), \quad (2.18)$$

where $Y_{lm}(\mathbf{r})$ are the spherical harmonics. In order to provide a rotationally invariant quantity, which is also real and a scalar we average over m :

$$q_l(i) = \sqrt{\frac{4\pi}{2l+1} \sum_{m=-l}^l |q_{lm}(i)|^2}. \quad (2.19)$$

The best choice for the neighbor cutoff is roughly the radius of the first solvation shell. Instead of calculating only the single $q_l(i)$'s, Lechner and Dellago [52] proposed

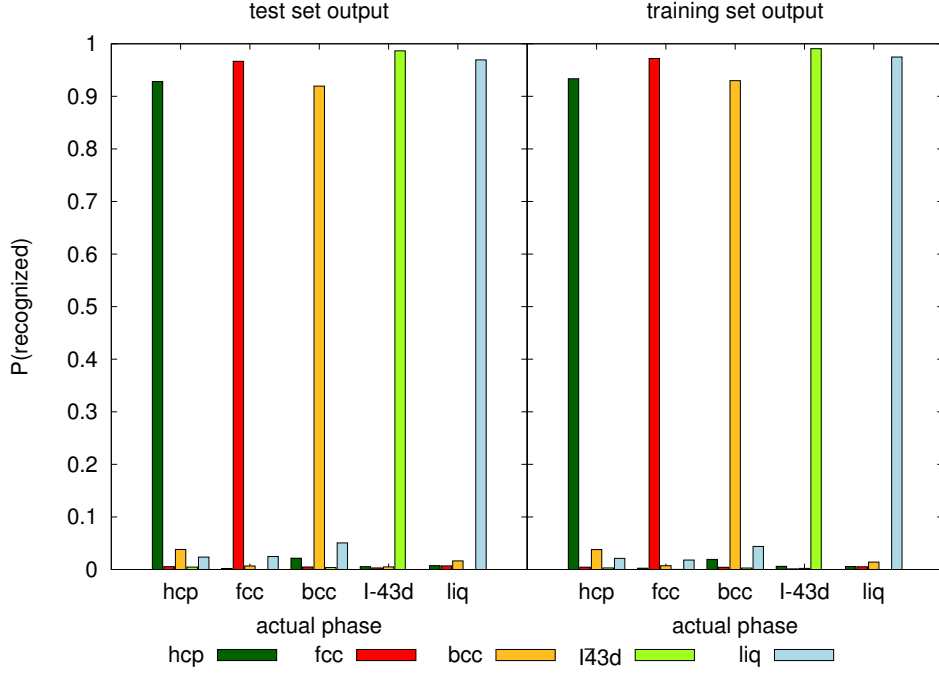


Figure 2.7.: Distribution of structures assigned by the neural network for the test set (left) and the training set (right) for the Lennard-Jones system. For each of the different phases indicated on the x -axis, the heights of the colour-coded bars correspond to the fractions of structures that have been assigned the type specified by the color at the bottom.

averaging over the first solvation shell. This is done in the following way: Instead of the average in Eq. (2.19) one can first average the q_{lm} over all neighboring particles

$$\bar{q}_{lm}(i) = \frac{1}{N_b(i) - 1} \sum_{k=0}^{N_b(i)} q_{lm}(k), \quad (2.20)$$

and then apply the usual average given in Eq. (2.19)

$$\bar{q}_l(i) = \sqrt{\frac{4\pi}{2l+1} \sum_{m=-l}^l |\bar{q}_{lm}(i)|^2}. \quad (2.21)$$

A scatter plot of the order parameters \bar{q}_4 and \bar{q}_6 computed for the configurations in the training set of the neural network is shown in Fig. 2.8. The dots in the scatter

plot are colored according to the phase from which the respective configurations were taken. To distinguish between the various structures, we divided the (\bar{q}_4, \bar{q}_6) -plane in regions as denoted by the lines in Fig. 2.8. Each configuration is then simply assigned the structure corresponding to the region in which the respective pair of \bar{q}_4 and \bar{q}_6 is located. (An alternative way to assign structure types consists in determining the frequency at which (\bar{q}_4, \bar{q}_6) -pairs occur in the various phases and then selecting the phase with the highest frequency [42].) Results of the structural analysis carried out in this way for the training set of the neural network are shown in Fig. 2.9. While liquid and fcc structures are recognized very accurately, the structure assignment is less accurate for hcp and, in particular, for bcc and I-43d structures. Thus, the order parameters \bar{q}_4 and \bar{q}_6 do not contain sufficient information on these structures as is also evident from the pronounced overlap of the hcp, bcc and I-43d phases in the (\bar{q}_4, \bar{q}_6) -plane. In comparison to the structure assignment based on \bar{q}_4 and \bar{q}_6 , the neural network yields a roughly uniform accuracy for all phases with a higher precision on the average.

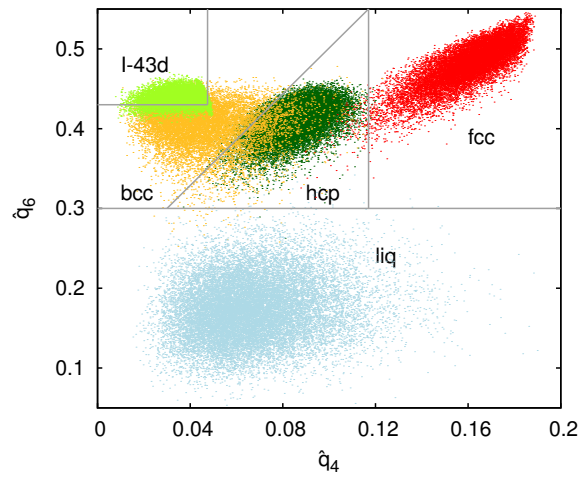


Figure 2.8.: Scatter plot in the (\bar{q}_4, \bar{q}_6) -plane of local structures taken from the different phases of the Lennard-Jones system. The lines delimit the regions used for the structure assignment.

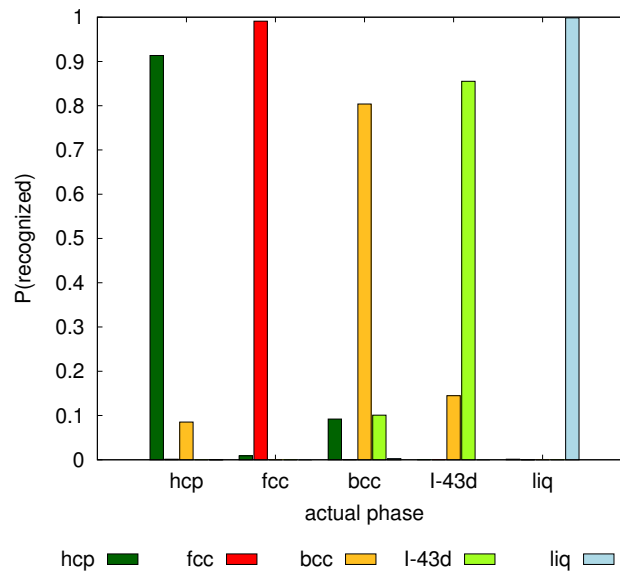


Figure 2.9.: Distribution of structures assigned based on \bar{q}_4 and \bar{q}_6 . For each of the different phases indicated on the x -axis, the heights of the colour-coded bars correspond to the fractions of structures that have been assigned the type specified by the color at the bottom.

2.2.7. Parameters of symmetry functions

In this section we list the parameters of the symmetry functions for the Lennard-Jones system (Tab. 2.1). Note that the additional use of G_4 , G_5 and G_8 type symmetry functions did not increase the accuracy of structure detection. Hence, these symmetry functions were omitted for the sake of computational efficiency.

Table 2.1.: Parameters of the symmetry functions for the Lennard-Jones system. The cutoff parameters used in this case are $R_c = 2.6\sigma$, $\alpha_c = 30\sigma^{-1}$, and $\epsilon_c = 0.2\sigma$. The integers in the first column of each table number the symmetry functions.

| G_2 | $\eta (\sigma^{-2})$ | $R_s (\text{\AA})$ | G_3 | $\kappa (\sigma^{-2})$ | G_7 | $\alpha (1)$ | $\eta (1)$ |
|-------|----------------------|--------------------|-------------|------------------------|---------------------|--------------|------------|
| 1 | 1.38889 | 1.310 | 20 | 0.5 | 34 | 0.2 | 9.0 |
| 2 | 2.00000 | 1.820 | 21 | 1.5 | 35 | 0.6 | 8.4 |
| 3 | 3.12500 | 1.745 | 22 | 2.0 | 36 | 0.6 | 4.8 |
| 4 | 3.12500 | 2.180 | 23 | 3.5 | 37 | 0.8 | 9.9 |
| 5 | 4.08163 | 1.970 | 24 | 4.5 | 38 | 0.9 | 9.0 |
| 6 | 8.00000 | 1.940 | 25 | 6.5 | 39 | 1.3 | 7.8 |
| 7 | 8.00000 | 2.030 | 26 | 8.5 | 40 | 1.4 | 9.6 |
| 8 | 8.00000 | 2.075 | 27 | 10.5 | 41 | 2.0 | 9.6 |
| 9 | 12.5000 | 1.115 | 28 | 12.0 | 42 | 2.3 | 8.7 |
| 10 | 12.5000 | 1.880 | 29 | 14.5 | 43 | 2.7 | 8.7 |
| 11 | 12.5000 | 2.030 | 30 | 18.0 | 44 | 2.8 | 13.2 |
| 12 | 12.5000 | 2.570 | | | 45 | 2.9 | 18.0 |
| 13 | 22.2222 | 2.090 | | | | | |
| G_6 | $\eta (\sigma^{-2})$ | | $\zeta (1)$ | $\lambda (1)$ | $\mu (\sigma^{-1})$ | | |
| 14 | 50.0000 | 2.150 | 31 | 2.50000 | 7 | -1 | 1.95 |
| 15 | 50.0000 | 2.375 | 32 | 2.85714 | 16 | -1 | 1.10 |
| 16 | 50.0000 | 2.600 | 33 | 3.33333 | 12 | 1 | 2.00 |
| 17 | 200.000 | 2.300 | | | | | |
| 18 | 200.000 | 2.510 | | | | | |
| 19 | 800.000 | 2.420 | | | | | |

Part II.

Application: Simulation of ice

On earth, under atmospheric conditions water can exist in three states of aggregation: vapor, liquid and ice. All these states are of crucial importance for life and have been topic of scientific studies since the earliest civilizations in ancient times. Nevertheless, many questions are still unanswered, for instance the mechanism of freezing liquid water into ice. Depending mainly on the pressure applied to the system, different solid phases can be produced, ranging from the well-known low density hexagonal ice Ih and cubic ice Ic to the very dense ice X. Currently, sixteen crystalline ice polymorphs and various non-crystalline amorphous structures are known to exist.

In this part of the thesis we show computational results for different properties of ice, such as radial distribution functions and infrared spectra for different ice phases, a nucleation study of low pressure ice and discuss technical aspects of the simulation of water.

Chapter 3.

Proton ordering of cubic ice

It has been discovered that the rich phase diagram of water ice features two types of first order phase transitions: a transition in which the underlying symmetries of the molecular lattice undergoes structural changes, and a second type, in which the molecular lattice remains essentially the same, but a reorientation takes place such that the lattice symmetries also include the hydrogen atoms. Thus many of the crystal lattices that ice adopts appear twice in the phase diagram; once with proton order and once without. We have studied the proton ordered phase of cubic ice, a phase of particular interest which exists on earth under atmospheric conditions. So far, only proton disordered cubic ice has been observed, whilst the experimental evidence of the proton ordered counterpart is missing. We conducted simulations* to predict the characteristic IR spectrum of proton ordered cubic ice so as to provide a tool by which to detect the presence of this phase in experiments[†], thereby observing proton ordered cubic ice the first time.[‡]

* *Ab initio* simulations were performed by Markus Macher of the group of Prof. Georg Kresse at the Faculty of Physics of the University of Vienna.

[†] All experiments were done by Jürgen Bernard, Josef N. Stern and Thomas Lörting from the Institute of Physical Chemistry of the University of Innsbruck.

[‡] The main part of this chapter has been submitted as an article to *Physical Review B* with the title "Proton ordering of cubic ice Ic: spectroscopy and computer simulations".

3.1. Introduction

Despite its simple molecular structure, water has a remarkably complex phase diagram. Application of pressure produces a variety of different solid ice phases with densities considerably higher than that of ordinary hexagonal ice, ice Ih. To date, sixteen thermodynamically stable or metastable crystalline phases (labeled with Roman numerals as Ih, Ic, II, III, ..., XV) [79–81] and several amorphous phases [82–84] have been discovered. While in some crystalline ice structures, including ice Ih as well as cubic ice, ice Ic, only the oxygen atoms form a regular lattice and the protons are disordered, in other ice phases, such as ice II, also the protons are arranged in a regular way. Indeed, there exist pairs of ice structures, such as ice Ih and its protonically ordered counterpart ice XI, which have nearly identical oxygen sub-lattices but differ in their proton order. Recently, Salzmann and collaborators have identified experimentally [80, 81] several previously unknown ice phases, completing the pairings V/XIII, XII/XIV and VI/XV, which differ only in proton ordering.

For all ice phases, in which water molecules remain intact and are tetrahedrally coordinated, the arrangement of protons in the protonically disordered structures is essentially governed by the so-called ice rules, or Bernal-Fowler rules [79]. These rules posit that (1) there are exactly two protons in proximity to each oxygen atom, to which they are covalently bonded, and (2) there is exactly one proton between two oxygen atoms, corresponding to a hydrogen bond between the neighboring molecules. According to the ice rules, all hydrogen configurations satisfying these two requirements are equally probable, implying that the interactions between non-neighboring molecules are not sufficient to stabilize a particular protonic arrangement. In this approximation, the ground state is thus strongly degenerate leading to the residual entropy of ice [79]. At very low temperatures, however, the difference in free energy between proton ordered and proton disordered configurations can lead to a phase transition to the proton ordered phase.

Experimentally, proton ordering transitions in crystalline ices are known to take place at low temperature and to be severely hampered by slow transformation kinetics. The highest ordering transition temperatures have been found for ice VII and ice III, which order below $T \sim 270$ K at $p > 2$ GPa to ice VIII [86] and below $T \sim 170$ K at $p \sim 0.3$ GPa to ice IX [87, 88], respectively. These two hydrogen ordering transitions in ice are the only ones known to take place in the absence of a catalyst. Other ordering transitions in the intermediate pressure regime at $p \sim 0.5 - 1.5$ GPa

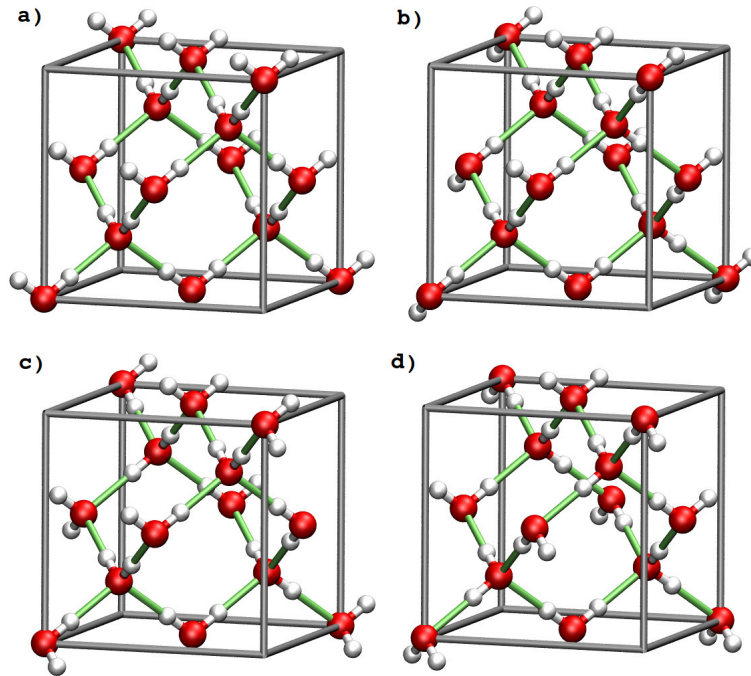


Figure 3.1.: Four distinct proton arrangements in a unit cell of cubic ice containing 8 water molecules [85]. Green sticks denote hydrogen bonds and the boundaries of the unit cell are shown as gray lines. Each configuration is a representative of one of the four symmetry inequivalent proton arrangements with different Coulomb energies that exist in a unit cell of this size. According to the calculations of Lekner [85], the fully ferroelectric configuration (a) has the highest energy and the anti-ferroelectric configuration (d) the lowest energy. Configurations (b) and (c) are weakly ferroelectric and have intermediate electrostatic energies.

take place at about $T = 100 - 150$ K, namely ice V \rightleftharpoons ice XIII [80], ice VI \rightleftharpoons ice XV [80] and ice XII \rightleftharpoons ice XIV [80]. These three transitions take place at an observable rate by using HCl as a dopant, which increases the reorientation rates of individual water molecules in the ice lattice, presumably by producing rotational Bjerrum L-defects [79]. Ambient pressure hexagonal ice, ice Ih, shows the lowest experimentally found ordering transition temperature of $T \sim 72$ K [89–96]. Such proton ordered ice XI is typically produced from ice Ih using hydroxide doping, e.g., by freezing a 0.1 M KOH solution.

While several protonically ordered ice phases have been prepared and analyzed in the laboratory, the proton ordered counterpart of cubic ice Ic has not been observed to date. In ice Ic, which is metastable, the oxygen atoms are arranged on a diamond lattice corresponding to a ABCABC... stacking of the puckered layers of hexagonal rings orthogonal to the c -axis. (In hexagonal ice, ice Ih, the stacking sequence is ABABAB... leading to a Wurtzite-like arrangement of the oxygen atoms.) The first coordination shell, however, is identical for both ice Ih and Ic such that one may expect ice Ih and ice Ic to proton order under similar conditions.

To study the energetics of proton arrangements in ice Ic, Lekner computed the electrostatic energies of all 90 proton configurations satisfying the ice rules in a periodically replicated unit cell of 8 water molecules [85, 97]. Due to the degeneracy of the Coulomb energy, there are only four classes of configurations with different energies, examples of which are shown in Fig. 3.1. Out of these, the perfectly ordered anti-ferroelectric proton configuration has the lowest electrostatic energy while the ferroelectric structure has the highest electrostatic energy. Weakly ferroelectric configurations have intermediate energies. This general trend is confirmed by calculations for larger unit cells such that, based on these results, thermodynamically one expects a transition to an anti-ferroelectric phase for ice Ic at sufficiently low temperatures. The purely electrostatic calculations of Lekner, however, are contrasted by recent *ab initio* (density functional theory) calculations, according to which the ferroelectrically ordered structure is the energetically most stable one. Similar differences between *ab initio* results and calculations based on empirical force fields have been reported also for the energetic ordering of various proton ordered forms of hexagonal ice [98]. Most likely, such discrepancies are due to polarization effects [99], which are fully taken into account in *ab initio* calculations but are neglected by most empirical potentials. While the energetics of proton ordering plays an important role for the low temperature proton ordered phases of ice, it may be their kinetic

accessibility that determines which structures are observed in the experiments.

In this chapter, we investigate the proton ordering of ice Ic using a combination of spectroscopic experiments and computer simulations. As discussed in detail below, the shape of the librational band of the IR-spectra measured in our work, interpreted on the basis of computed IR-spectra, indicates that hydroxide doped ice Ic partially proton orders following an experimental protocol similar to that used previously to proton order ice Ih. Interestingly, the combination of experiment and theory suggests that cubic ice indeed shows a tendency to ferroelectric proton order, however, kinetics may strongly influence the ordering transition.

The remainder of this chapter is organized as follows. In Sec. 3.2 we explain the computational model and methods used to carry out the simulations and report their results. Experimental procedures and results are described in Sec. 3.3 and discussed and interpreted in Sec. 3.4 based on the spectra computed in our simulations.

3.2. Simulations

In order to detect proton ordered cubic ice in the laboratory it is important to be capable of distinguishing the various degrees of protonic order that are consistent with the ice rules. One possible way to do that is via the signature of proton order on the vibrational spectrum obtained in infrared (IR) or Raman spectroscopy experiments, methods that have been employed before to study proton order in ice [100–102]. In the present work, we used molecular dynamics simulations complemented with *ab initio* calculations to study the structural and dynamical properties of various proton ordered ice Ic polymorphs. In particular, we determined radial distribution functions and IR spectra for different proton ordered cubic ice candidates and compared them to the ones for hexagonal ice Ih and its proton ordered counterpart, ice XI. In doing so, we focused on translational and librational modes, as these modes carry the most information about proton ordering and provide the basis for the interpretation of the experimental IR-spectra presented in Sec. 3.3.

3.2.1. Model and Methods

All our molecular dynamics simulations are performed using the TIP4P/ice model [103], developed to reproduce the properties of the various ice phases and, specifically, the phase diagram of ice. This model is described in detail in Sec. 5.1. Since

the TIP4P/Ice model water molecules are rigid, only motions that do not involve intramolecular vibrations can be studied such that our IR-spectra are limited to the low frequency bands corresponding to translational and librational modes. To investigate the higher frequency part of the spectrum a model with flexible water molecules would be required [104] (comprehensive studies of dielectric properties of liquid water using different rigid as well as flexible potential models are presented in Refs. [105, 106]).

To follow the dynamics of the system, we integrated the equations of motion with a quaternion based integrator as described in Sec. 5.3 that maintains the rigid geometry of the water molecules. Electrostatic interactions were treated with Ewald summation [40] following the implementation details outlined in Sec. 5.4.

The initial configurations of the different proton ordered phases were generated by periodically replicating the unit cells given in Ref. [85] for cubic ice and Refs. [91, 98] for ice XI, respectively. The proton disordered counterparts were set up employing a method suggested by Rahman and Stillinger [107] and modified by Ayala and Tchijov [108], which is briefly described in section 5.2.

To quantify the structural and dynamical diversity of various degrees of proton order, we have calculated energies, pair correlation functions as well as infrared absorption spectra. The pair correlation function $g_{AB}(r)$ measures the conditional probability to find an atom of species B at distance r from an atom of species A relative to the same probability in a hypothetical ideal gas with the same density and composition. In the present case we consider the pair correlation functions $g_{OO}(r)$, $g_{HH}(r)$, and $g_{OH}(r)$ between pairs of oxygen atoms, pairs of hydrogen atoms, and oxygen and hydrogen atoms, respectively. All of these functions can be extracted from data obtained in neutron diffraction experiments [109].

Infrared absorption spectra are calculated in the classical approximation [110, 111] as the Fourier transform of the time auto-correlation function $\langle \mathbf{M}(0) \cdot \mathbf{M}(t) \rangle$ of the total dipole moment \mathbf{M} ,

$$I(\omega) \propto \int_0^\infty dt \langle \mathbf{M}(0) \cdot \mathbf{M}(t) \rangle \cos \omega t, \quad (3.1)$$

where ω is the vibrational frequency and angular brackets $\langle \dots \rangle$ indicate a time or ensemble average. The dipole-dipole correlation function can be written in terms of the dipole moments $\boldsymbol{\mu}_i$ of individual water molecules, which are determined by the magnitude, sign and location of the charges on the TIP4P/Ice molecules as well as

by their orientation,

$$\langle \mathbf{M}(0) \cdot \mathbf{M}(t) \rangle = \sum_{i,j} \langle \boldsymbol{\mu}_i(0) \cdot \boldsymbol{\mu}_j(t) \rangle. \quad (3.2)$$

Note that while the cross correlation terms $\langle \boldsymbol{\mu}_i(0) \cdot \boldsymbol{\mu}_j(t) \rangle$, $i \neq j$, which quantify the correlations between the dipole moments of different water molecules, are negligible for high frequency modes associated with intramolecular stretching and bending motions, they play an important role for the form of the spectrum in the range characteristic for translations and librations involving collective motions of multiple molecules [106, 112].

In general, the calculation of dielectric properties in simulations, as for instance the dielectric constant of ice, is difficult. In contrast to liquid water, where the H-bond network is rapidly rearranged, ice structures change only at very long time scales. In order to sample all important fluctuations an extension of straightforward molecular dynamics or MC integration has to be employed (see MacDowell and Vega [113]). Since we are only interested in faster fluctuations of the dipole moment and not in the computation of the dielectric constant, our calculation of the time autocorrelation function (ACF) is not affected by this complexity and we could gather all data from conventional MD trajectories.

We complemented the results of our simulations based on the TIP4P/Ice model with energies and spectra computed *ab initio* using the Vienna *ab initio* simulation package (VASP)* and PAW [114] potentials in the implementation of Kresse and Joubert [115]. The outermost core radii for the O and H potentials are 1.52 and 1.1 a.u., respectively (corresponding to the standard potentials distributed with the VASP package). All calculations were performed using the Perdew-Burke-Ernzerhof (PBE) functional [116], as well as using van der Waals density functional theory (vdW-DFT) [117]. We specifically used the vdW-DFT of Klimeš et al. termed “optPBE” (optimized PBE) [118, 119]. The Brillouin zone was sampled at $6 \times 6 \times 6$ k -points. To determine the equilibrium volume of each structure, all internal parameters (including relative lattice parameters) were optimized at seven volumes around the equilibrium volume, and the energy vs. volume curve was fitted using an equation of state. At the equilibrium volumes (at $T = 0$ K), the vibrational frequencies were evaluated using finite differences: all symmetry inequivalent atoms were

* *Ab initio* calculations were performed by Markus Macher of the group of Prof. Georg Kresse at the Faculty of Physics of the University of Vienna.

displaced along symmetry inequivalent directions, and the interatomic force constant matrix was completed using symmetry considerations [120]. The vibrational frequencies were determined at the Γ -point by diagonalization of the force constant matrix. The dipole activity was calculated from Born effective charge tensors for oxygen and hydrogen, respectively. For consistency with the molecular dynamics simulations and to account for thermal expansion, the vibrational frequencies were evaluated at the average densities computed in the MD simulations. The vdW-DFT equilibrium volumes (at $T = 0$ K) are, however, only 3 – 4 % smaller than the average MD volumes.

3.2.2. Simulation results

To investigate the structure of ice Ih and ice Ic, we calculated radial distribution functions using NpT molecular dynamics simulations of $N = 1000$ (for the parental cubic ice) and $N = 896$ (for the parental hexagonal ice) water molecules with orthogonal simulation boxes at temperature $T = 170$ K and pressure $p = 0.1$ bar. The proton ordered counterparts were calculated using the same simulation boxes, but are of lower space group symmetry, e.g., orthorhombic symmetry in case of ice XI. Similarly, proton ordering of cubic ice Ic leads to configuration that are not cubic but display a lower symmetry. When we speak about cubic and hexagonal ordered structures in the following, we always refer to the symmetry of the disordered parent structure. For the proton disordered configurations we also carried out simulations at $T = 70$ K, the temperature to which ice Ic is cooled in the experiments. Note that at a temperature of $T = 170$ K initially proton ordered configurations immediately disorder on the experimental time scale. In the simulations, however, no proton disordering is observed during the entire simulation because the simulation time is shorter than the time scale of proton disordering. In all simulations, a time step of 2 fs and a Lennard-Jones cutoff of 3σ were used. The same cutoff was used for the real space part of the Ewald summation, where for the reciprocal space 1152 k -vectors were employed.

All simulations were performed for a hydrogen mass of $m_{\text{H}} = 1$ and an oxygen mass of $m_{\text{O}} = 16$, except for the IR spectra at 170 K, where also the deuterium mass $m_{\text{D}} = 2$ was used. The total length of the simulations was 5 ns in each case. Average densities and energies computed in these MD simulations are listed in Tab. 3.1 alongside with the electrostatic energies computed by Lekner [85, 97] as well as the

Table 3.1.: Average densities $\langle\rho\rangle = m_{\text{H}_2\text{O}}N/\langle V\rangle$ and average potential energies per molecule $\langle E_{\text{pot}}\rangle$ for the cubic and hexagonal ice phases at temperatures $T = 70\text{ K}$ and $T = 170\text{ K}$, respectively, and pressure $p = 0.1\text{ bar}$. Also shown are the Coulomb energies E_{Coul} calculated by Lekner [85, 97] and the cohesive energies $E_{\text{coh}}/E_{\text{RPA}}$ per molecule computed using density functional theory at $T = 0\text{ K}$ and $p = 0\text{ bar}$. All energies are stated with respect to the corresponding energy of the structure ice Ic (ord. d). The statistical errors were calculated by block average analysis [40] and are given as single numbers in round brackets, which correspond to the error in the last digit.

| ice phase | $\langle\rho\rangle_{70\text{K}}$ ($\frac{\text{kg}}{\text{m}^3}$) | $\langle\rho\rangle_{170\text{K}}$ ($\frac{\text{kg}}{\text{m}^3}$) | $\langle E_{\text{pot}}\rangle_{70\text{K}}$ ^a ($\frac{\text{kJ}}{\text{mol}}$) | $\langle E_{\text{pot}}\rangle_{170\text{K}}$ ^a ($\frac{\text{kJ}}{\text{mol}}$) | E_{Coul} ^b ($\frac{\text{kJ}}{\text{mol}}$) | E_{coh} ^c ($\frac{\text{kJ}}{\text{mol}}$) | E_{RPA} ($\frac{\text{kJ}}{\text{mol}}$) |
|--|---|--|---|--|--|---|--|
| ice Ih | 930.17 (2) | 919.00 (3) | 0.0098 (2) | 0.0169 (5) | | | |
| ice XI (Cmc2 ₁) | 930.31 (3) | 919.12 (2) | 0.0471 (2) | 0.0547 (5) | 0.750 | -0.492 | |
| ice XI (Pna2 ₁) | 929.95 (2) | 919.25 (3) | -0.0195 (2) | -0.0250 (5) | -0.032 | -0.096 | |
| ice Ic | 932.11 (2) | 919.89 (2) | 0.0449 (2) | 0.0524 (4) | | | |
| ice Ic (a, I4 ₁ md) | 929.32 (2) | 918.39 (2) | 0.2319 (2) | 0.2299 (5) | 0.816 | -0.531 | -0.521 |
| ice Ic (b, Pna2 ₁) | 932.29 (2) | 920.66 (3) | 0.0364 (2) | 0.0333 (4) | 0.408 | -0.261 | -0.212 |
| ice Ic (c, P4 ₁) | 932.24 (2) | 920.51 (2) | 0.0277 (1) | 0.0261 (5) | 0.204 | -0.106 | -0.068 |
| ice Ic (d, P4 ₁ 2 ₁ 2) | 932.57 (3) | 920.63 (3) | 0.0000 | 0.0000 | 0.000 | 0.000 | 0.000 |

^a The total average potential energy per molecule of the reference structure (d) at $T = 70\text{ K}$ is $\langle E_{\text{pot}}\rangle_{70\text{K}} = -67.0872 (2)\text{ kJ/mol}$ and at $T = 170\text{ K}$ $\langle E_{\text{pot}}\rangle_{170\text{K}} = -64.3298 (3)\text{ kJ/mol}$.

^b Relative Coulomb energies calculated by Lekner [85, 97] for a simplified model at $T = 0\text{ K}$ for the parameters $q = 0.5\text{ e}$, $R = 2.75\text{ \AA}$, $q^2/R \approx 1.309\text{ eV}$ and $f=0.35$ in Lekner's notation.

^c The cohesive energy per molecule of the reference structure (d) with respect to infinitely separated water molecules is $E_{\text{coh}} = -63.813\text{ kJ/mol}$.

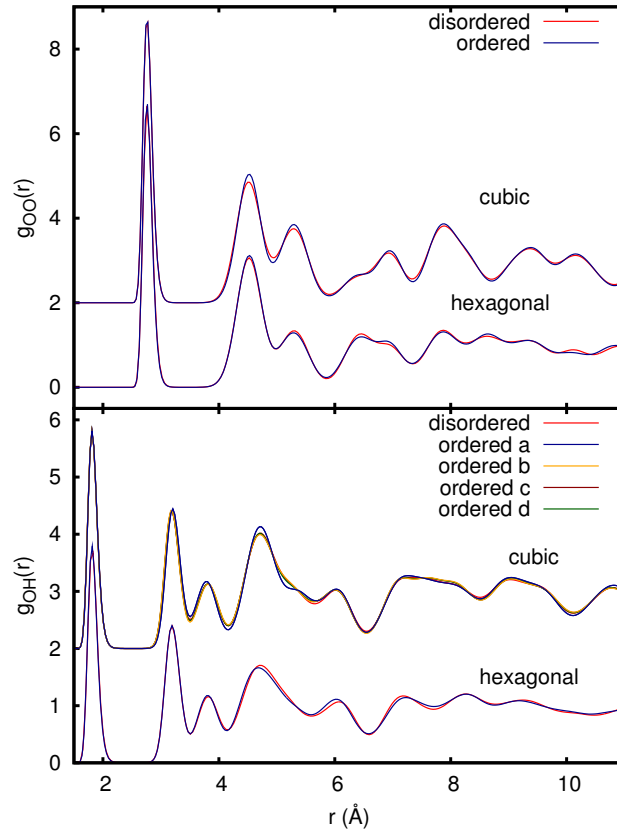


Figure 3.2.: Radial distribution functions $g_{OO}(r)$ and $g_{OH}(r)$ for proton disordered hexagonal and cubic ice as well as their proton ordered counterparts at $T = 170$ K. Both the oxygen-oxygen as well as the oxygen-hydrogen radial distribution functions are nearly identical in all cases including proton ordered and disordered configurations. The curves labeled a, b, c, and d correspond to the proton orderings shown in Fig. 3.1. Note that the peaks corresponding to the intramolecular OH- and OO-distances lie outside the range of the figure.

energies determined in our *ab initio* simulations. The electrostatic calculations for the idealized structures and the MD simulations were carried out at $T = 170$ K and at $T = 70$ K. They agree in the energetic ordering of the various structures both finding that the anti-ferroelectric structure (d) has the lowest energy and the ferroelectric structure (a) has the highest energy, while structures (b) and (c) have intermediate

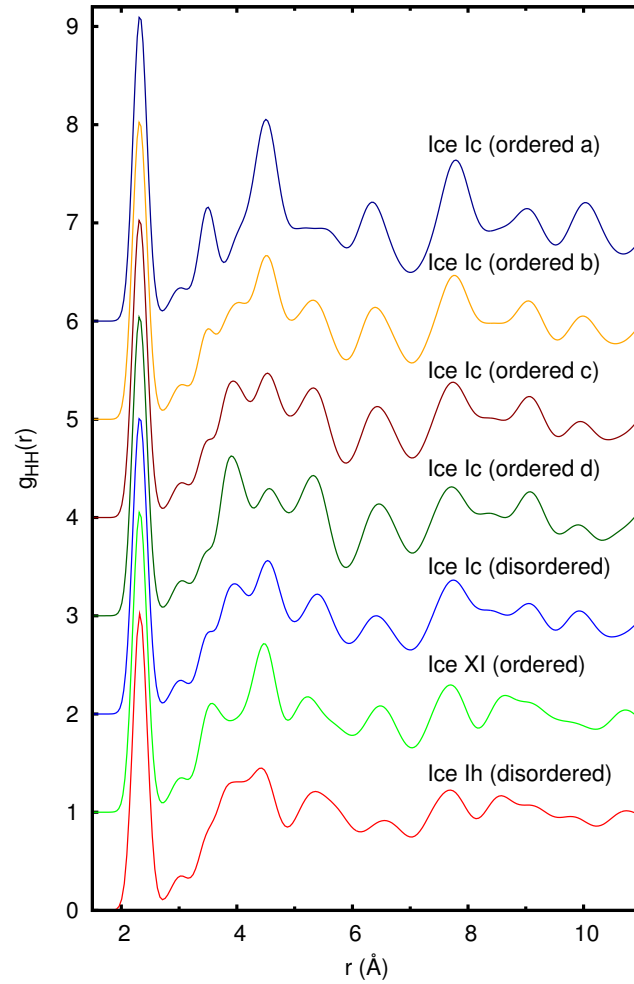


Figure 3.3.: Radial distribution functions $g_{HH}(r)$ for the different cubic and hexagonal ice polymorphs at $T = 170$ K. The labeling a, b, c, and d refers to the various proton ordering patterns shown in Fig. 3.1.

energies. The energies obtained using density functional theory, however, display the reverse energetic order but agree well with energies computed previously using DFT methods [121] (for the sake of comparison, we note that the structures (a),(b),(c) and (d) correspond to the space groups $I4_1md$, $Pna2_1$, $P4_1$, $P4_12$, respectively). To double check the density functional theory data, we performed more accurate calculations using exact exchange and the random phase approximation (EXX-RPA) for the correlation energy [122, 123]. These calculations were also extended to ice II, VIII, for which highly accurate diffusion Monte Carlo results are available [124]. In these cases (ice II, ice VIII, ice Ih), we found excellent agreement with the published diffusion Monte Carlo validating the EXX-RPA. The EXX-RPA results confirmed the order of the cubic phases predicted by density functional theory: The ferroelectric structure (a) has the lowest energy the anti-ferroelectric structure (d) has the highest energy, and the structures (b) and (c) have intermediate energies. This discrepancy, observed before for hexagonal ice [98], is probably due to the neglect of polarization effects in the TIP4P/ice, which are expected to be particularly pronounced in ferroelectric structures leading to a lowering of their energy. We would like to emphasize that predicting the correct energetic ordering is known to be difficult in case of proton ordered ices. Vega et al. [125] have shown that SPC/E, TIP4P and TIP5P predict a transformation from ice Ih to the anti-ferroelectric $Pna2_1$ structure [126] below 70 K. The ferroelectric $Cmc2_1$ structure, which is obtained in experiments, is predicted to be the lowest lying H-bond isomer only in the model by Nada and van der Eerden (NvdE) [127].

The radial distribution functions of proton disordered hexagonal ice, ice Ih, and its proton ordered counterpart, ice XI, as well as disordered cubic ice, ice Ic, and its four proton ordered candidates are given in Figures 3.2 and 3.3. As expected, the oxygen-oxygen radial distribution functions $g_{OO}(r)$ feature no significant differences for all the order/disorder ice polymorph pairings. In addition, the oxygen-hydrogen radial distribution function $g_{OH}(r)$ show only minute deviations and only the hydrogen-hydrogen radial distribution function $g_{HH}(r)$ differ appreciably. However, these differences are small making it exceedingly difficult to distinguish between different variants of protonically ordered cubic ice based on the comparison of pair correlation functions determined experimentally from X-ray or neutron diffraction data [109].

More detailed structural information on proton ordering is encoded in vibrational spectra. For the calculations of the IR spectra using MD simulations we have set

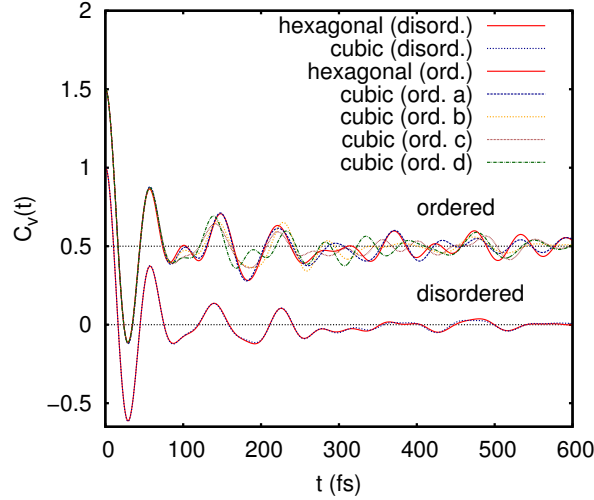


Figure 3.4.: Normalized velocity ACF of the hydrogen atom for different ice structures. The correlation functions for the proton ordered systems are displaced vertically for greater clarity.

up cubic and hexagonal lattices consisting of $N = 1000$ and $N = 896$ molecules, respectively. The time step was set to 2 fs, dipole-dipole time correlation functions were calculated for times up to 20 ps, and in total each system was propagated for 40 ns using a Nosé-Hoover NVT integrator. Here, the Lennard-Jones cutoff and the Ewald summation real space cutoff were chosen to be 3σ . The densities for the different arrangements of hexagonal and cubic ice were set according to Table 3.1.

In order to speed up the convergence of the calculated IR spectra one can use an approximation of Eq. (3.1), where the total dipole-dipole correlation function is replaced by a sum over the single molecule velocity auto-correlation functions $\langle \mathbf{v}_O(0) \cdot \mathbf{v}_O(t) \rangle$, $\langle \mathbf{v}_H(0) \cdot \mathbf{v}_H(t) \rangle$ and $\langle \mathbf{v}_O(0) \cdot \mathbf{v}_H(t) \rangle$ [106]. In the librational region the main contribution comes from the hydrogen-hydrogen correlation function, thus all other ACFs can be neglected. The auto-correlation functions

$$C_v(t) = \frac{\langle \mathbf{v}_H(t) \mathbf{v}_H(0) \rangle}{\langle |\mathbf{v}_H(0)|^2 \rangle}$$

for all studied phases are plotted in Fig. 3.4. While the Fourier transform of the total dipole moment ACF (Eq. (3.1)) was used to generate all IR spectra shown below, the approximation described here yields almost identical results. The influence of

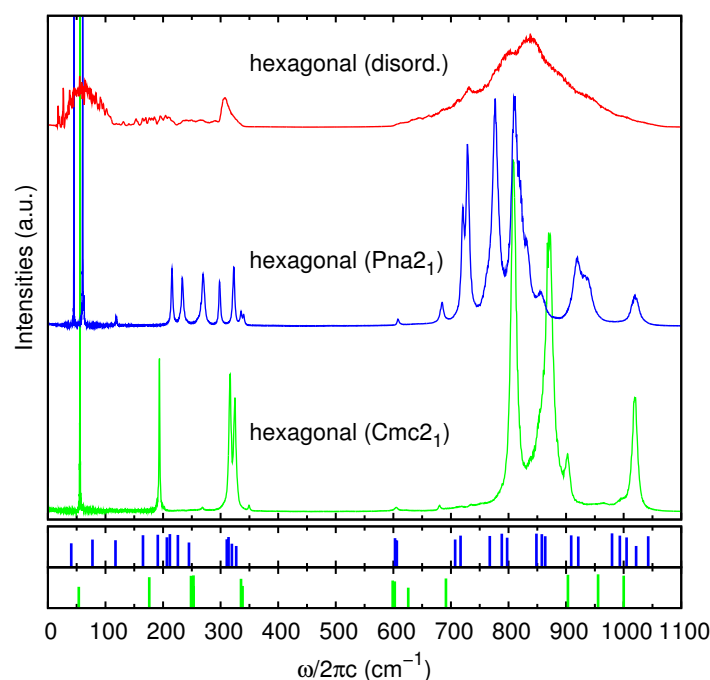


Figure 3.5.: IR spectra for various proton ordered and disordered forms of hexagonal H_2O ice obtained from molecular dynamics simulations at $T = 70$ K. Vertical bars in the bottom plots indicate the results of *ab initio* simulations at $T = 0$ K and are plotted on a logarithmic scale.

the particular correlation functions on different IR frequency bands in the case of liquid water is discussed in more details in Ref. [106].

Figures 3.5 and 3.6 show the computed IR spectra (using Eq. 3.1) for hexagonal and cubic ice, respectively. In general, the computed spectra are in reasonable agreement with experimental spectra. The broad librational band near 850 cm^{-1} is in good agreement with experimental spectra of both cubic and hexagonal ice (see dashed line in Fig. 3 of Ref. [128]). Also in the far-infrared ($0 - 400\text{ cm}^{-1}$) the agreement is reasonable, even though there are some discrepancies especially regarding the band intensities. Hexagonal ice shows three broad bands in this area [129], which are centered at 160 , 230 and 370 cm^{-1} . In our simulations there are three broad bands centered at 70 , 195 and 310 cm^{-1} . The absorption spectra of the proton disordered forms of hexagonal and cubic ice are clearly distinguishable from those of the various proton ordered phases, which split up in several bands,

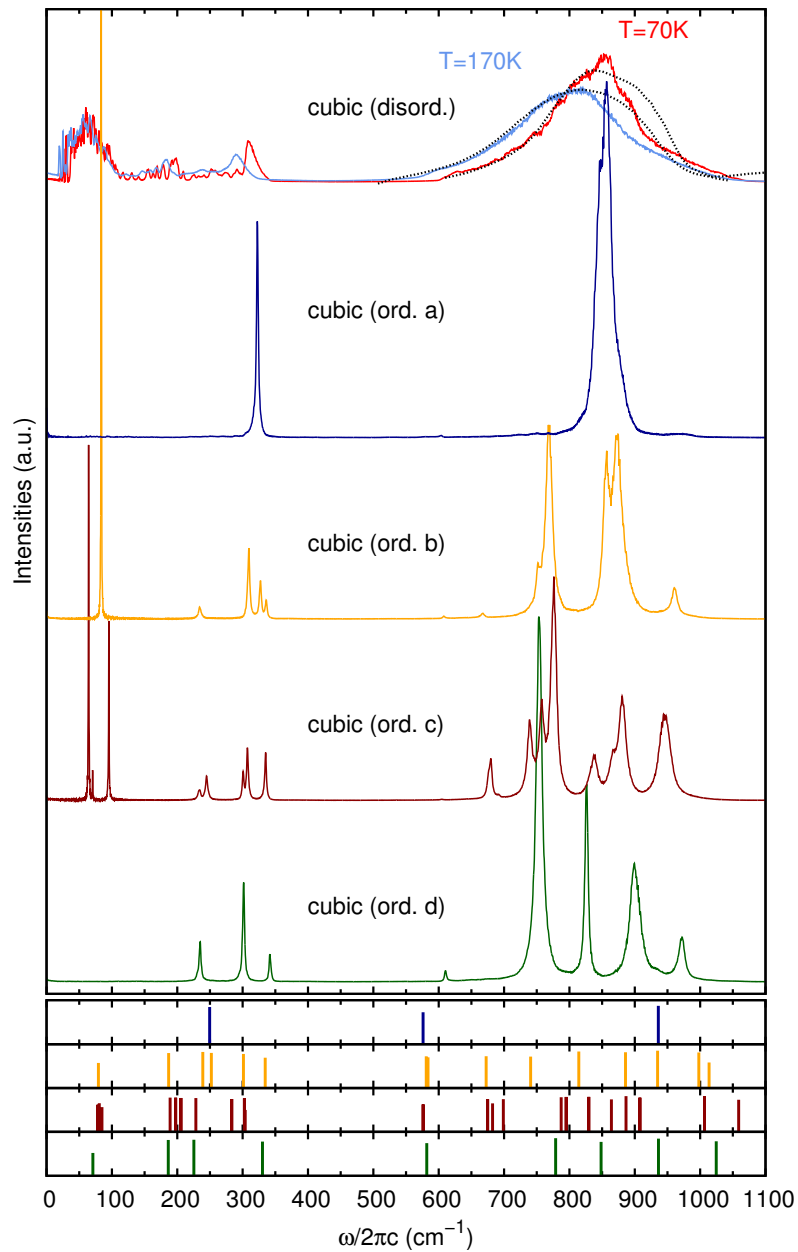


Figure 3.6.: IR spectra for various proton ordered and disordered forms of cubic H₂O ice. Lines indicate results from the MD simulations carried out at $T = 70\text{K}$. In the topmost plot we also show results for disordered cubic ice at $T = 170\text{K}$ and the experimental spectra (black dotted lines, given also in Fig. 3.9). Vertical bars in the bottom plots indicate the results of *ab initio* simulations at $T = 0\text{K}$.

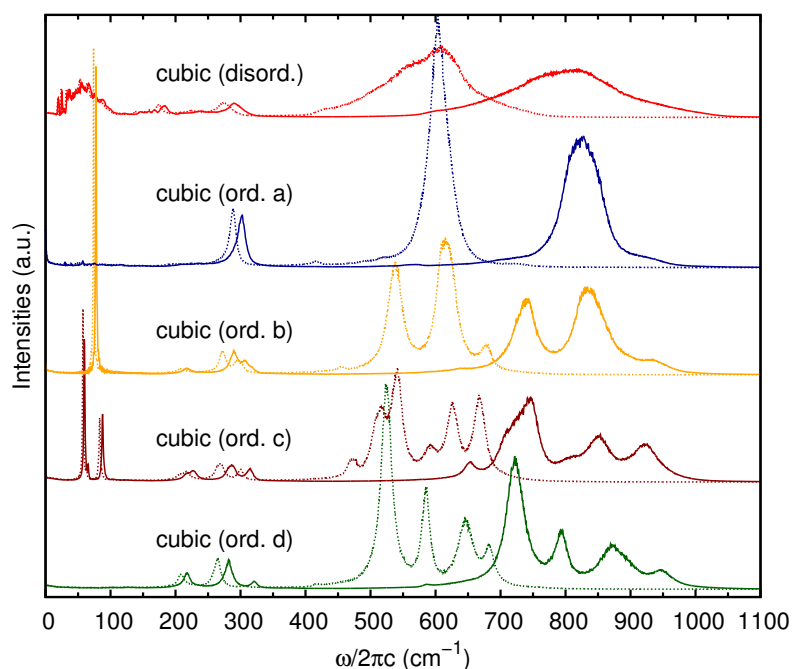


Figure 3.7.: IR spectra for various proton ordered and disordered forms of cubic H₂O (solid) and D₂O ice (dotted), respectively. All MD simulations were carried out at $T = 170$ K.

the number and position of which depend on the particular proton ordering pattern. Thus, these spectra provide a means of detecting the presence of proton order experimentally. IR spectra computed by density functional theory for proton ordered cubic ice at $T = 0$ are shown in Fig. 3.6 as vertical bars and confirm this conclusion. The length of each bar shown in Fig. 3.6 corresponds to the dipole activity of the corresponding mode. Since the *ab initio* spectra were determined using a harmonic approximation, finite temperature broadening of the individual peaks is entirely absent. The overall structure of the *ab initio* spectra is, however, fairly similar to the spectra obtained from the MD simulations, although in the density functional theory calculations the librational band ($550 - 1100 \text{ cm}^{-1}$) is shifted by about 100 cm^{-1} to higher frequencies. For instance, for structure (a) a single librational band at 930 cm^{-1} is predicted using density functional theory, whereas a 20 cm^{-1} broad peak at 856 cm^{-1} is observed in the molecular dynamics simulation. Likewise four peaks are predicted for structure (b), which correspond well to the four

peak structure observed in the molecular dynamics simulations. A further noteworthy difference between the *ab initio* and the MD results is that the average frequency calculated *ab initio* shifts significantly to the blue with increasing ferroelectric ordering. We find average frequencies of 930, 900, 880 and 850 cm^{-1} for cubic ice with ordering (a) (ferroelectric), (b) (weakly-ferroelectric), (c) (weakly-ferroelectric) and (d) (anti-ferroelectric), respectively. In the MD simulations the shift is smaller with frequencies of 849, 833, 826 and 816 cm^{-1} for the four phases. The difference is most likely related again to the neglect of polarization effects in the MD simulations using the TIP4P/ice model.

In addition to the spectra shown in Fig. 3.6, which were obtained for H_2O at 70 K, in Fig. 3.7 we present also 170 K spectra for H_2O and D_2O . While for heavy water a clear shift to lower frequencies in the librational region can be observed, the qualitative form of the spectra remains the same.

We have also investigated the possibility to probe proton order based on the OH-stretching band using a recently developed computational method [130, 131] that relates the OH-frequency to the electric field acting on the proton. Such an analysis can therefore be carried out also for rigid water molecules, in which the geometrical constraints prevent the OH-bond from vibrating. To first order approximation, the Raman frequency shift is proportional to the electric field $\Delta\omega \propto E$, where E is the electric field measured at the hydrogen position and projected onto the O-H bond axis. Thus, using the electric field distributions one can easily calculate the corresponding Raman spectrum in the O-H stretching region. E -field distributions and auto-correlation functions for all our structures are plotted in Fig. 3.8. The system and simulation parameters were the same as described above for the simulations to calculate the pair correlation functions. The normalized correlation function

$$C_E(t) = \frac{\langle E(t)E(0) \rangle}{\langle E(0) \rangle^2}$$

was calculated up to 4 ps, where each whole trajectories spanned a period of 1 ns. The small deviations in these quantities suggest that the resulting spectra would not show significant differences between the studied structures. This is because the coupled OH-frequency is less suitable for probing proton ordering than the librational/translational bands and the decoupled OH- or OD-stretching modes for slightly deuterated H_2O samples or slightly hydrogenated D_2O samples [87, 132]. For this reason, we have not undertaken further efforts to calculate the Raman spectra in this frequency region.

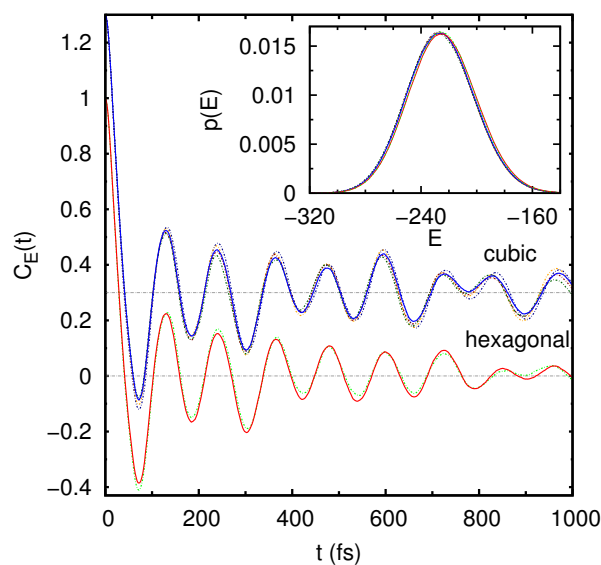


Figure 3.8.: Normalized ACF of the electric field. The electric field E is measured at the H atom and projected onto the O-H bond axis. The insert shows the distributions of the E-field for all studied structures.

3.3. Experiments*

As mentioned in the Introduction, ice Ih and ice Ic differ in their layer stacking but have an identical local structure. One would therefore expect that ice Ic shows a similar proton ordering transition as ice Ih. The experimental protocol to proton order ice Ih involves bringing the sample to ~ 50 K, which is thought to produce some ferroelectric ice XI seeds, and then waiting at $\sim 55 - 67$ K for several days or weeks, which allows the ice XI domains to grow [92–96]. Typically, about 50 – 60 % of the hexagonal ice sample orders using this procedure. Since the local ordering is identical in cubic and hexagonal ice, we anticipate that a similar protocol might allow for hydrogen ordering in cubic ice. To investigate this possibility we have carried out experiments on cubic ice. As discussed in detail below, our observations indicate partial proton ordering detected by comparison of the measured IR-spectra with the results of our simulations.

* This section describes experiments done by Jürgen Bernard, Josef N. Stern and Thomas Lörting from the Institute of Physical Chemistry of the University of Innsbruck.

To carry out our experiments, we prepared an aqueous 0.1 M KOH solution containing 2 mol% of D₂O. The use of a small fraction of D₂O allows for the observation of the decoupled OD-stretching mode in infrared spectra, in addition to the coupled OH-stretching mode. KOH introduces substitutional point defects in the ice lattice, which increase the proton mobility and hence reorientational dynamics drastically. We use 0.1 M KOH in order to reach a saturation level of these substitutional point defects. In principle, also lower concentrations such as 0.01 M KOH might be suitable for reaching this enhancement in the dynamics. Cubic ice was prepared by spraying droplets of this solution of about 3 μm in diameter into a vacuum-chamber containing a He-cryostated optical window, where the window was first kept at ~ 77 K. This procedure is known to produce hyperquenched glassy water (HGW), which crystallizes to cubic ice upon heating to ~ 160 K [133, 134]. Cubic ice prepared in this way shows a comparably low number of hexagonal stacking faults and high cubicity index as judged from the intensity of the X-ray reflexes corresponding to the hexagonal faults [134].

The crystallization from HGW to cubic ice was monitored by in situ FT-IR spectroscopy, and the librational band of cubic ice at ~ 160 K is depicted as the blue curve in Fig. 3.9. Cubic ice was then cooled to ~ 60 K for a few hours and then heated to 70 K for about 80 hours. The spectrum recorded after this procedure is depicted in red in Fig. 3.9. It can clearly be noted that the half-width decreases for all observed bands. The half-width of the decoupled OD-band at ~ 2420 cm⁻¹ (not shown in the figure) decreases from 52 to 23 cm⁻¹. The librational band depicted in Fig. 3.9 shows a decrease in the *full width at half maximum* (FWHM) from 251 cm⁻¹ to 196 cm⁻¹, i.e., to about 80 %. In addition to the narrowing also some structuring of the band is apparent such that it can no longer be understood as a single Gaussian band. The band also loses intensity between 500 and 600 cm⁻¹. From band decomposition analysis two intense Gaussian components at 837 cm⁻¹ and approximately 905 cm⁻¹, as well as a less intense band at 995 cm⁻¹ are needed to explain the observed band shape. Note that a similar band narrowing was observed in IR spectra of the partial ordering of hydrogen atoms in ice Ih [128]. However, while there is no difference between cubic ice and hexagonal ice at 160 K, shoulders emerge at different positions after partial hydrogen ordering, i.e., the hydrogen order pattern differs between proton ordered cubic ice and ice XI.

We now turn to the question whether the band changes seen in Fig. 3.9 are a result of a simple thermal effect or whether proton-ordering can be inferred from

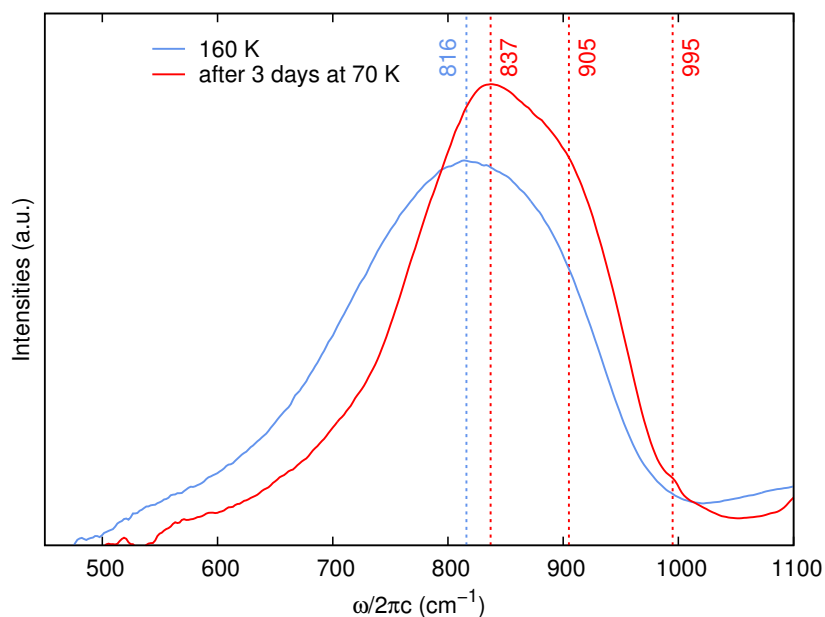


Figure 3.9.: Librational band of the IR spectra of cubic ice determined experimentally at $T = 160$ K (black line) and after 80 hours at $T = 70$ K (red line).

the data. Figure 3.10 shows the evolution of the librational band in KOH-doped ice Ic when changing the temperature step by step from 45 K to higher temperatures. The temperature-broadening of the band is best illustrated in the magnified inset of Fig. 3.10. It is quite small when increasing the temperature in the range 45 – 70 K (6 cm^{-1} per 25 K), but larger when changing the temperature from 70 K to 75 K (4 cm^{-1} per 5 K). Above 75 K the temperature broadening is again quite small (5 cm^{-1} per 25 K). This shows that an additional effect, besides thermal broadening, influences the change in half-width of the librational band between 70 K and 75 K, which we interpret to be proton-disordering of partially ordered cubic ice. The occurrence of the proton disordering temperature between 70 K and 75 K in cubic ice seen in Fig. 3.10 compares to the known proton-disordering temperature of 72 K in hexagonal ice [89–96]. This implies that the phase boundary between ordered and disordered cubic ice is located at almost the same temperature as the phase boundary between ordered and disordered hexagonal ice. The two thick lines

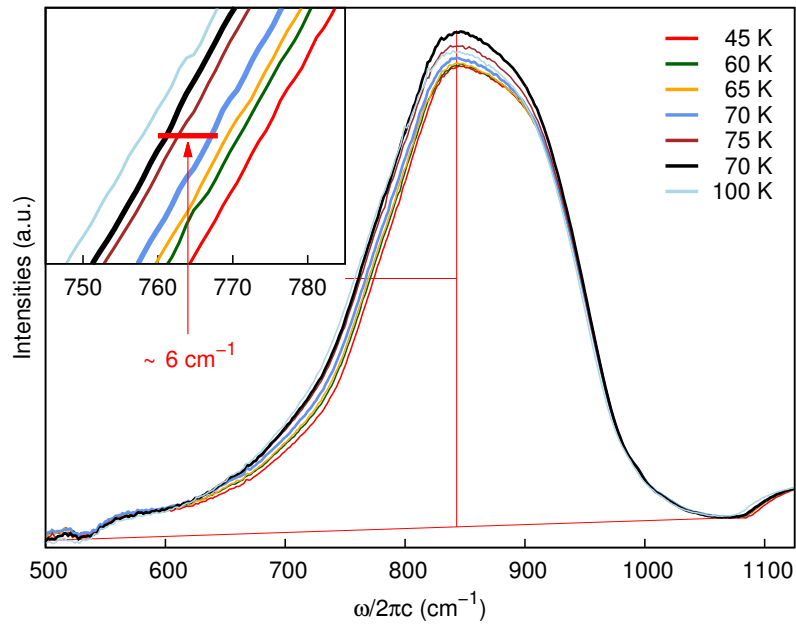


Figure 3.10.: Libration mode of ice Ic doped with KOH at different temperatures, recorded after the following steps. Ice Ic doped with KOH was prepared by vitrification of the aqueous solution (200.2 g 0.1 M KOH(aq) + 4.9 g D₂O) at 50 K using the technique of hyperquenching and subsequently crystallizing the amorphous deposit by bringing the sample holder for half an hour to 140 K. The following temperature protocol was then applied while continuously recording IR spectra: 14 h at 45 K; 2 h at 50 K; 20.5 h at 60 K; 7.5 h at 65 K; 22 h at 70 K; 23 h at 75 K; 7 h at 80 K; 2 h at 90 K and 2 h at 100 K. After these steps the temperature was decreased again to 70 K for 18.5 h. Selected spectra as marked are shown in the figure and magnified in the inset. The two thick lines show the librational mode after 22 h at 70 K (blue line), after the sample was kept at 45 – 65 K before, and after 18.5 h at 70 K (black line), after the sample was kept at 100 K before.

in Fig. 3.10 compare two librational bands recorded for KOH-doped ice Ic, both determined at 70 K after having kept the sample several hours at 70 K: the narrower band (blue line) was obtained after several days of waiting at temperatures below 70 K and then heating to 70 K, whereas the broader band (black line) was obtained after cooling from 100 K to 70 K, without any waiting time at temperatures below 70 K. In case of the proton-ordering transition from hexagonal ice to ice XI it was shown that the proton-ordered phase grows much faster at 70 K if it was nucleated before at temperatures below 70 K, e.g., at 60 K [89–96], whereas by cooling from 100 K to 70 K, without a prior nucleation step at lower temperature, the proton-ordering is much slower in case of KOH-doped hexagonal ice. We expect this to be similar in case of KOH-doped cubic ice. The difference in half-width at half-maximum of about 6 cm^{-1} between the two spectra taken at 70 K seen in Fig. 3.10 clearly demonstrates that this expectation is really seen in the spectra. Indeed, an effect other than motional narrowing is operative, which we explain as proton-ordering when the proton-ordered phase was nucleated by keeping the sample for several days between 45 K and 65 K.

Figure 3.11 shows a comparison of the two librational bands recorded at 70 K on KOH-doped cubic ice (black and blue traces, both taken from Fig. 3.10) and on undoped cubic ice (red trace), which was kept several days at 45 - 65 K before. Clearly, the librational band is narrower in the case of KOH-doped ice. In this case the difference in half-width is even about 10 cm^{-1} . This shows that KOH-doping is required to achieve proton-ordering in cubic ice, that a smaller degree of proton-ordering is also reached when cooling directly from 100 K to 70 K, without the nucleation step at 45 – 65 K, whereas in the case of undoped cubic ice proton-ordering cannot be inferred from the data. Further systematic studies about the dependence of the half-width of the librational band on the thermal history using much longer waiting times (on the order of months) are necessary to find conditions that might allow for a higher degree of proton-ordering, or even to access the fully proton-ordered state of cubic ice. Also an investigation of the influence of other dopants (e.g., NH_3 , HCl , etc.) is of interest in this context.

3.4. Discussion

Assuming that the band structuring and narrowing that is observed in addition to the pure thermal narrowing in our spectra indeed arises from partial hydrogen ordering

in cubic ice, we may now compare the observed band with the predicted spectra of Fig. 3.6. For protonically disordered cubic ice, the predicted librational band centered at $\sim 800 \text{ cm}^{-1}$ coincides almost perfectly with the experimentally observed librational band both in position and width, which is about $\text{FWHM} \sim 200 \text{ cm}^{-1}$. Our MD simulations predict that depending on the particular type of proton ordering this band splits into up to 6 bands, all of which show a FWHM of about $\sim 20 \text{ cm}^{-1}$. That is, the FWHM of the ordered forms is about 10% of the FWHM in case of the disordered form. In the experiment, the FWHM in the possibly ordered form of cubic ice is reduced to about 80%, thus suggesting that the degree of hydrogen

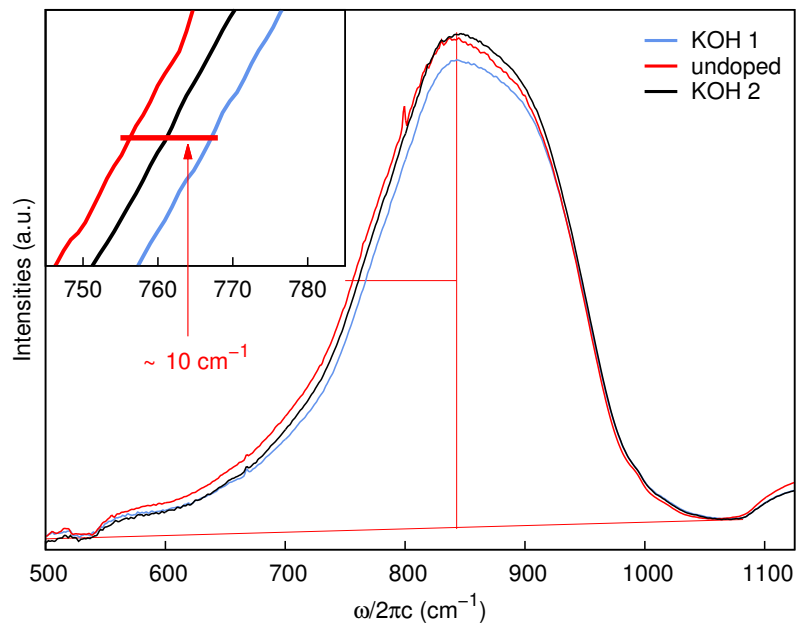


Figure 3.11.: Libration mode of ice Ic doped with KOH (preparation see caption of Fig. 3.10) compared with undoped ice Ic prepared using the same procedure. The following temperature protocol was then applied while continuously recording IR spectra for undoped ice Ic: 19 h at 45 K, 4 h at 50 K, 19 h at 60 K, 20 h at 65 K, 7 h at 70 K and 16 h at 75 K. The red line shows the librational mode of undoped ice after 7 h at 70 K and is compared to the two 70 K spectra of KOH-doped ice Ic from Fig. 3.10.

ordering achieved experimentally is no more than 20 %.

Band deconvolution suggests that three bands contribute to the experimental band shape. The main peak at 837 cm^{-1} is most likely related to the predominant disordered cubic ice and shifts only little compared to the original disordered cubic ice phase (816 cm^{-1}). This small shift of 20 cm^{-1} might be related to the lower temperature of 70 K compared to 160 K. While usually there is a blue shift when lowering temperature, here we observe a red shift, which is probably related to the anomalous temperature dependence of ice [79] and may also result in positive Grüneisen parameters for several modes [135]. Furthermore, in the experiment a distinct shoulder at 905 cm^{-1} is observed accounting for about one third of the integrated intensity.

This band structure of the partially ordered phase seems to be consistent with a more pronounced ferroelectric order, which both in the DFT calculations as well as in the MD simulations leads to a pronounced blue shift compared to anti-ferroelectric order. In particular, for the ferroelectric structure (a) DFT predicts a strong single peak at 930 cm^{-1} while the vibrational band of the anti-ferroelectric order (d) is shifted to the red by about 80 cm^{-1} on the average. In the TIP4P/ice simulations the dominant peak for cubic ice (a) as well as (b) is located at a lower frequency of 856 cm^{-1} , a difference of 70 cm^{-1} .

The experiment also shows a weak but clearly resolved shoulder at 995 cm^{-1} approximately 90 cm^{-1} above the main peak arising as a result of the conjectured partial proton order. This side peak is not accounted for by the ferroelectrically ordered structure (a), which shows only one single peak. Such side peaks are, however, present both in the cubic ordered variants (b) and (c), with structure (b) showing very similar ratios between the main peak and the higher frequency shoulder as in the experiment. In fact, the magnitude of the two band splittings is about 70 cm^{-1} and 90 cm^{-1} in the experiment, and thus quite similar to the splittings of 90 cm^{-1} and 90 cm^{-1} predicted for the ordered structure (b) (see Fig. 3.6). The other three ordered variants of cubic ice show quite different patterns and splittings. This might suggest that the transformation occurs into structural variant (b) and not the lowest energy structure ordered ice (a), so that the experimentally observed ordered form does not necessarily need to correspond to the thermodynamically most stable form, especially because kinetics is known to play an important role in the proton ordering transitions of ice, as for instance observed in ice XIV [80]. It is also possible that the experimental spectrum might develop into the spectrum of ordered ice (a)

with increasing time and increasing proton ordering instead of developing the peak splittings predicted for structure (b).

Interestingly, the ordered variants of cubic ice also show shifts and/or splittings of the acoustic and optical modes at $< 400 \text{ cm}^{-1}$ compared to disordered cubic ice according to our simulations (see Fig. 3.6). That is, investigation of acoustic and optical modes in the future by means of IR or Raman scattering seems to be a promising tool for critically testing the type of proton ordering obtained experimentally in cubic ice.

The temperature dependence of the librational band shape and width suggest that the proton-order-disorder transition in cubic ice takes place at about 70 – 75 K, which is very similar to the proton-order-disorder temperature of 72 K observed in case of hexagonal ice. Furthermore, the degree of proton-ordering and narrowing of the bands at 70 K is clearly enhanced when employing a “nucleation” step at temperatures of 45 – 65 K. Whereas we observe in our experiments on KOH-doped cubic ice at $T < 75 \text{ K}$ a band narrowing in addition to the narrowing caused by motional narrowing, we do not observe such an additional narrowing in case of undoped, pure cubic ice on the time scale of days.

Finally, we compare our result presented here with the result obtained by Suga [136], who was unable to observe the onset of proton ordering in cubic ice prepared in the presence of a mole fraction of 1.8×10^{-3} KOH by measuring heat capacity and enthalpy (i.e., the heat capacity divided by the temperature) in the temperature range 13 – 100 K. Suga suggests that his inability to observe proton ordering maybe related to his route of preparing cubic ice, namely by heating the high-pressure ice phase III/IX at ambient pressure to 160 K. In particular, the fact that “high-pressure forms of ice reject their ionic impurities from the specimen” is at the origin of the inability to produce proton-ordered cubic ice when going via high-pressure forms of ice. Suga hence concluded that “In order to realize the hypothetical ordered phase of Ic, the deposition method of atomized aerosol from a KOH aqueous solution will be worthy of trial”. This is exactly what we have done here, and so Suga’s expectation that proton-ordered cubic ice maybe accessible via a route, which does not involve high-pressure ice phases, has now turned out to be correct.

In summary, we have carried out FT-IR spectroscopy experiments combined with molecular dynamics and *ab initio* computer simulations to study the proton ordering transition of ice Ic. We find that the librational band of ice Ic displays some significant changes if the sample is subjected to an experimental protocol similar

to that used before to proton order hexagonal ice. By comparison with theoretical IR-spectra computed with the TIP4P/Ice model and using *ab initio* simulations we find that these changes are best explained by assuming that the ice Ic sample underwent a partial ordering transition. Based on a comparison of the computed and measured librational spectra no unique assignment of the type of protonic order is currently possible. While considering the intensity loss at low frequencies implies a partial ordering into a ferroelectric structure, the number and relative positions of the peaks obtained from deconvolution of the experimental data point to a weakly ferroelectric structure. Further experiments and simulations will be necessary to resolve this issue.

Chapter 4.

Detection of ice structures

In order to study phase transitions in water and ice under high pressure, such as the freezing from the liquid phase into high pressure ice phases, or solid-solid transitions between different ice structures, one requires an order parameter that clearly distinguishes between the involved phases. In this chapter, we demonstrate that our neural network detection method described in Chapter 2 can be used for this purpose. We have developed different types of feed forward neural networks to detect the ice phases Ih, Ic, II, III, V and liquid water. Furthermore, we apply our method to the study of nucleation of super-cooled liquid water into hexagonal ice Ih.*

*The main part of this chapter has been submitted as an article to the *Journal of Chemical Physics* with the title "Neural networks for local structure detection in polymorphic systems".

4.1. Motivation

As shown in Chapter 2, local bond order parameters based on spherical harmonics perform well in detecting the various simple crystalline structures such as those occurring in the Lennard-Jones systems. They are less accurate, however, when applied to more complex structures such as liquid water and the various phases of ice [54]. While modifications of these order parameters have been successfully used to distinguish hexagonal ice (ice Ih) from liquid water [137], the high pressure phases of ice (ice II, III, ...) are not separated sufficiently in this projection. Distributions of the Steinhardt bond order parameters q_4 , q_6 , q_8 and q_{10} calculated for the various

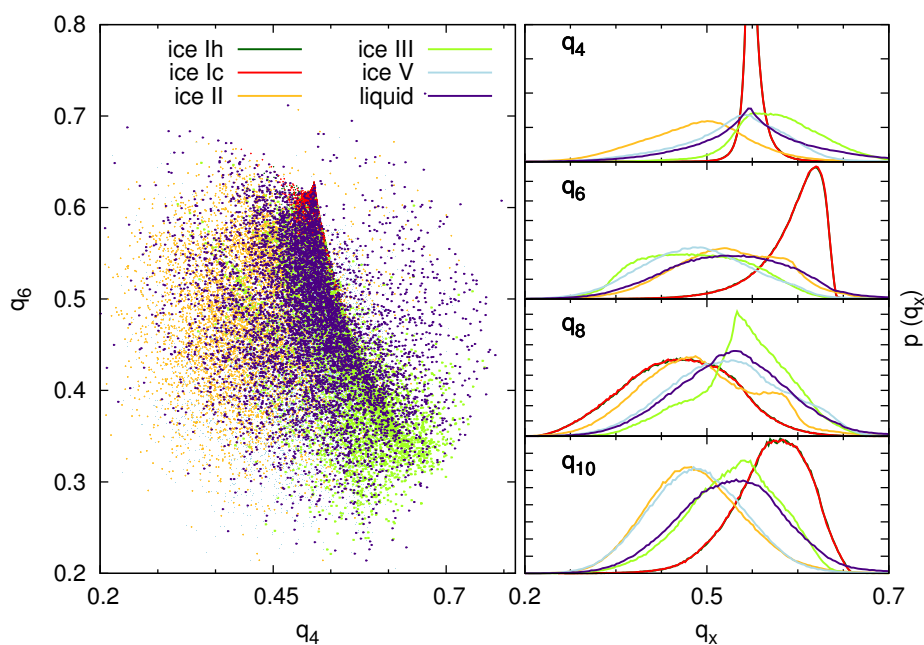


Figure 4.1.: (left) Scatter plot in the (q_4, q_6) -plane for structures taken from liquid water and from different phases of ice. To calculate the bond order parameters only the positions of the oxygen atoms were taken into account. All results are obtained from NVT simulations carried out at $T = 270$ K and densities $\rho_{\text{Ih}} = \rho_{\text{Ic}} = 910 \text{ kg/m}^3$, $\rho_{\text{II}} = 1145 \text{ kg/m}^3$, $\rho_{\text{III}} = 1115 \text{ kg/m}^3$, $\rho_{\text{V}} = 1210 \text{ kg/m}^3$ and $\rho_{\text{liq}} = 985 \text{ kg/m}^3$. (right) Distributions of q_4 , q_6 , q_8 and q_{10} obtained for the same systems.

phases of ice, and shown in the right panel of Fig. 4.1, display a pronounced overlap. The distributions do not separate even if they are spread out in two dimensions, as shown in the left panel of Fig. 4.1. Note that to generate the plots of Fig. 4.1 we have used configurations obtained for only a few temperatures and pressures, thus the distributions overlap becomes even stronger if wider regions in the P - T -plane are considered. One reason for the inability of the Steinhardt bond order parameters to distinguish between the high pressure forms of ice is that these phases include oxygens with different spatial environments. The unit cell of ice III, for instance, features two distinct oxygen positions and for ice V there are even four unique oxygen positions. For this reason using the averaged bond order parameters \bar{q}_4 and \bar{q}_6 leads to an even worse separation for the high pressure phases of ice.

In an effort to enhance the recognition for ice structures several techniques have been suggested. Chau and Hardwick [56] have developed an order parameter based on detecting the occurrence of local tetrahedral structures in ice. (A scaled version, which is defined in the range 0 to 1, is given in Ref. [57].) This method is very accurate for the distinction between hexagonal or cubic ice I from liquid water, but fails for the higher density forms of ice. Similarly, the maximum projection method of Brukhno et al. [54] can be used to distinguish between liquid water and hexagonal and cubic ice only. Here we demonstrate that an appropriately trained neural network can be used to distinguish locally between liquid water and several phases of ice (I_h, I_c, II, III, and V) over wide ranges of pressure and temperature.

4.2. Training set

All calculations for ice and liquid water were carried out with the TIP4P/Ice model [103], which is described in detail in Sec. 5.1. Using molecular dynamics simulations, we generated training and test sets that consist of configurations for the six studied water phases over a wide range of temperatures and densities, such that configurations of highly metastable structures are also included. We carried out simulations in the NVT and isotropic NPT ensembles using a Verlet-like integration scheme [76, 138, 139] as described in Sec. 5.3.

For each phase, we generated molecular dynamics trajectories at different pressures and densities encompassing the entire range of mechanical stability. System sizes were chosen such that the simulation box accommodates a defect-free crystal of the respective type. In particular, molecule numbers of $N_{\text{Ih}} = 896$, $N_{\text{Ic}} = 1000$,

$N_{\text{II}} = 960$, $N_{\text{III}} = 768$, $N_{\text{V}} = 756$ and $N_{\text{liq}} = 940$, were used for ice Ih, ice Ic, ice II, ice III, ice V, and the liquid, respectively. Initial configuration were taken from literature and prepared according to the methods described in Sec. 5.2.

Each molecular dynamics trajectory was 100 ps long and every 0.1 ps the environmental information of a randomly chosen oxygen atom was stored and used to generate an entry for the training or test set. A total of 100 trajectories were computed yielding 10^5 configurations. The training and test sets were then generated by computing the symmetry functions for each configuration and assigning to it the structure type of the simulated phase. This way to construct the training and test set relies on the assumption that during the molecular dynamics simulation the entire sample remains in the original phase and defects or excursions to other phases do not occur even transiently.

We calculated isotherms for each ice phase to identify the regions of mechanical stability. Results are presented in Fig. 4.2. For each data point we averaged the pressure over a period of 60 ps and 300 ps for the solid structures and the liquid, respectively. For these calculations smaller simulation boxes were used. In particular, the system sizes for ice Ih $N_{\text{Ih}} = 360$, for ice Ic $N_{\text{Ic}} = 512$, for ice II $N_{\text{II}} = 324$, for ice III $N_{\text{III}} = 324$, for ice V $N_{\text{V}} = 336$ and for the liquid systems $N_{\text{Liq}} = 350$ were used.

4.3. Symmetry functions

To define symmetry functions capable of capturing the important details of local structures we have computed radial distribution functions as well as the distributions of O-O-O angles for all phases considered here. The results of these calculations are shown in Fig. 4.3. As one can infer from Fig. 4.3b, for distances smaller than 3.25 \AA the angles $\alpha = 50^\circ, 72^\circ, 83^\circ, 105^\circ, 125^\circ, 154^\circ$ appear to be useful symmetry function parameters, where in the shell of distances between 3.5 \AA and 5.5 \AA $\alpha = 45^\circ, 61^\circ, 120^\circ, 136^\circ$ are good candidates. Based on these distribution functions, we have defined the symmetry functions listed in Tab. 4.1 in the last section of this chapter. For these symmetry functions we have used a neighbor cutoff of $R_c = 6 \text{ \AA}$ and the parameters $\epsilon_c = 0.2 \text{ \AA}$ and $\alpha_c = 30 \text{ \AA}^{-1}$, respectively. We have also prepared a set of symmetry function parameters for a much larger cutoff of $R_c = 8.234 \text{ \AA}$. In both cases, only the positions of the oxygen atoms are used to compute the symmetry functions. Including also hydrogen positions or, equivalently, information on dipole

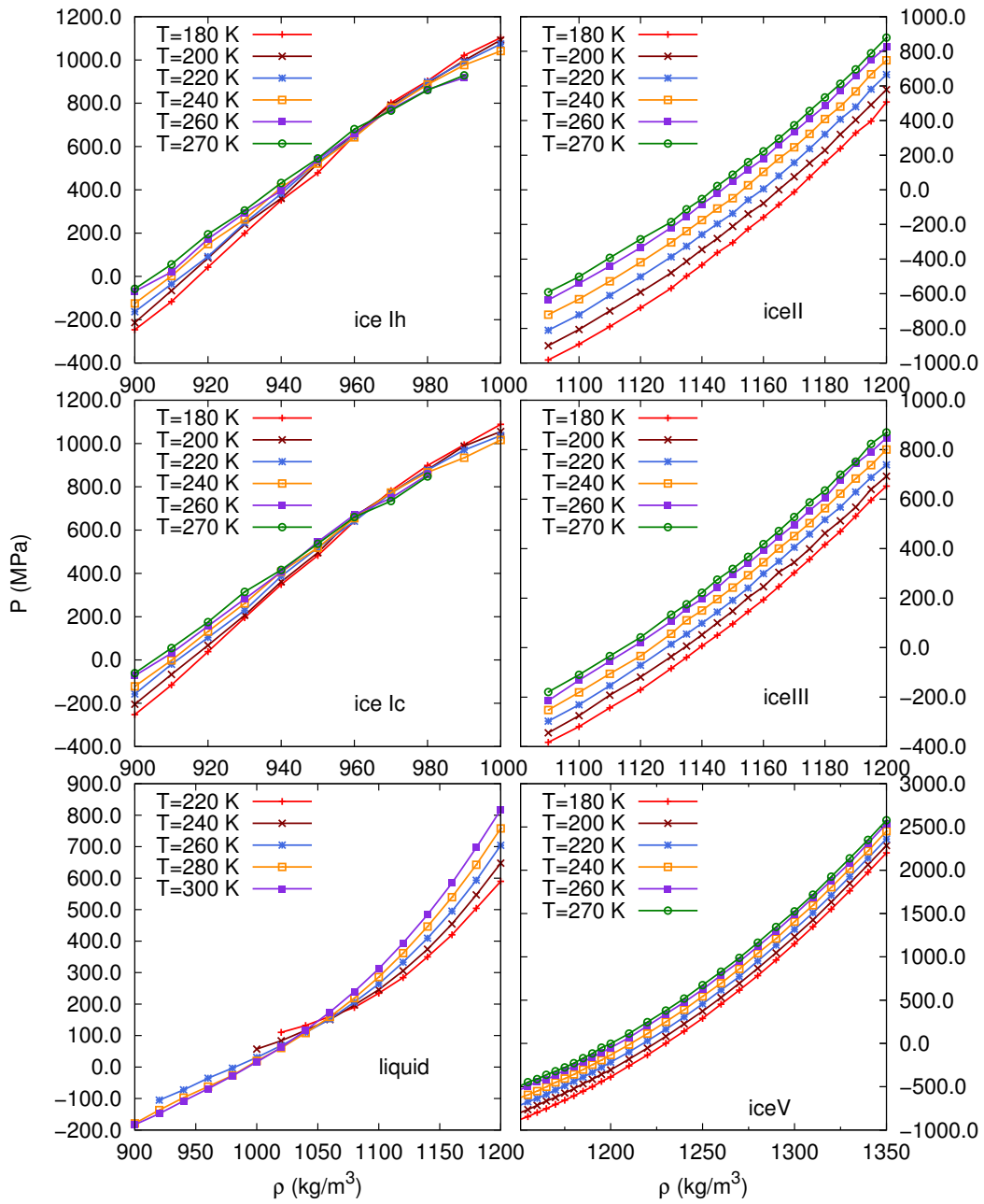


Figure 4.2.: Isotherms for the water polymorph ice Ih, Ic, II, III, V and liquid water for different temperatures.

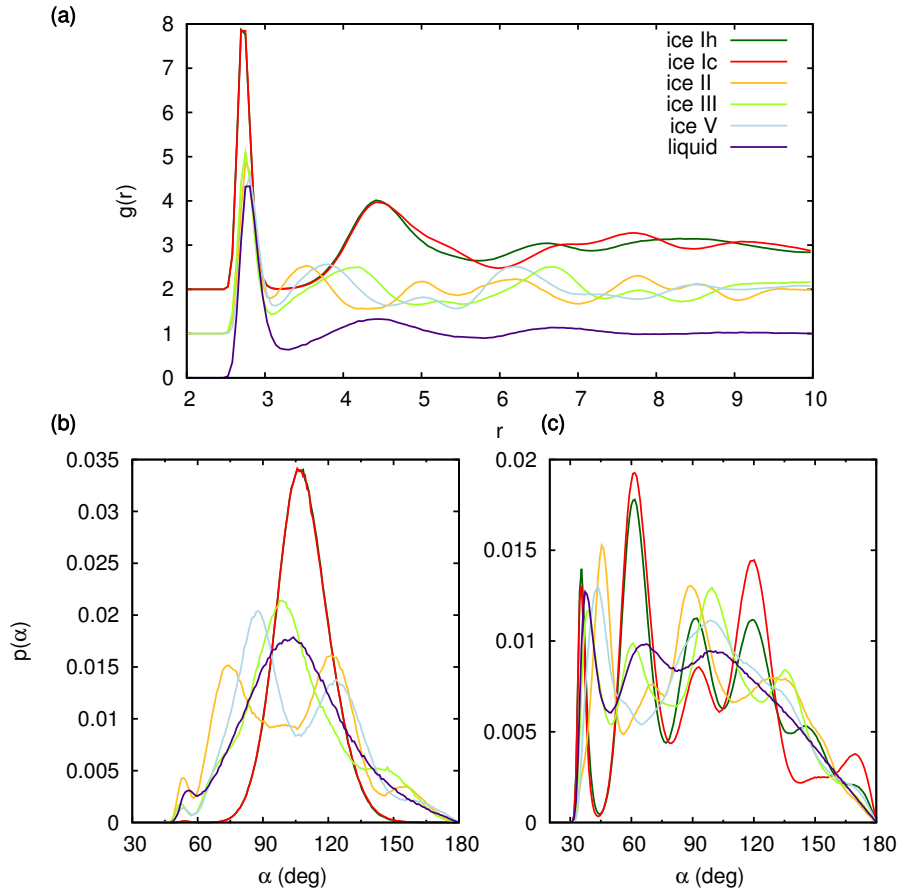


Figure 4.3.: Radial and angular distribution functions for different phases of water. (a) Oxygen-oxygen radial distribution functions $g_{\text{OO}}(R)$ for low density and high density forms of ice as well as liquid water. All curves except the one for liquid water are shifted for better readability. (b) Distributions of the OOO-angle for atoms within a distance of $R_{\text{cut}} = 3.25 \text{ \AA}$ from the central atom. (c) Distributions of the OOO-angle for atoms within the shell $3.5 \text{ \AA} \leq R \leq 5.5 \text{ \AA}$ around the central atom. All curves were determined in NVT simulations at temperatures $T_{\text{Ih}} = T_{\text{Ic}} = 210 \text{ K}$, $T_{\text{II}} = T_{\text{III}} = T_{\text{liq}} = 270 \text{ K}$ and $T_{\text{V}} = 240 \text{ K}$. For the densities the values $\varrho_{\text{Ih}} = \varrho_{\text{Ic}} = \varrho_{\text{liq}} = 1000 \text{ kg/m}^3$ and $\varrho_{\text{II}} = \varrho_{\text{III}} = \varrho_{\text{V}} = 1200 \text{ kg/m}^3$ were chosen.

orientations, may improve the accuracy of the detection further.

4.4. Neural network training and structure detection

Using the training set and the symmetry functions described in the previous section we have trained two different neural networks to distinguish local structures of ice Ih, Ic, II, III, V and of liquid water. The two networks differ on the network topology, $35 \times 30 \times 30 \times 6$ and $39 \times 35 \times 35 \times 6$, and also in the cutoff radius, $R_c = 6 \text{ \AA}$ and $R_c = 8.234 \text{ \AA}$. With these cutoffs the local regions encompass two and three neighbor shells, respectively. Results obtained with these two neural networks are shown in Fig. 4.4. For the smaller cutoff the detection accuracy is between 85% for ice V and 98% for ice III. With the larger cutoff the detection accuracy is nearly 100% for all phases. The spatial resolution, however, is reduced with the larger cutoff.

4.5. Crystallization of supercooled water

In order to demonstrate the practical applicability of the neural network for structure detection, we have used it to study the freezing of supercooled water to hexagonal ice. The free energetics of this nucleation process has been studied previously using metadynamics [140] and umbrella sampling [53, 54, 141]. Here, we determine the free energy of the system using the size n of the largest crystalline cluster as order parameter. To compute this order parameter for a particular configuration, first all water molecules are assigned a structure type by applying the neural network. Then, crystalline molecules are grouped into connected clusters and the order parameter is given by the number n of molecules in the largest of these crystalline clusters. Two molecules are considered to be connected if their oxygen atoms are closer than 3.8 \AA .

In these simulations we have used a neural network for structure detection trained specifically to distinguish only liquid water from ice I, without discriminating between hexagonal ice Ih and cubic ice Ic. Furthermore, a cutoff radius of $R_c = 4.43352 \text{ \AA}$ was used, implying that only information from the first neighbor shell was included in computing the symmetry functions. In order to improve the accuracy of the structure detection near the surface of the crystalline nucleus, we have also included crystalline nuclei of cubic and spherical shape embedded in liquid wa-

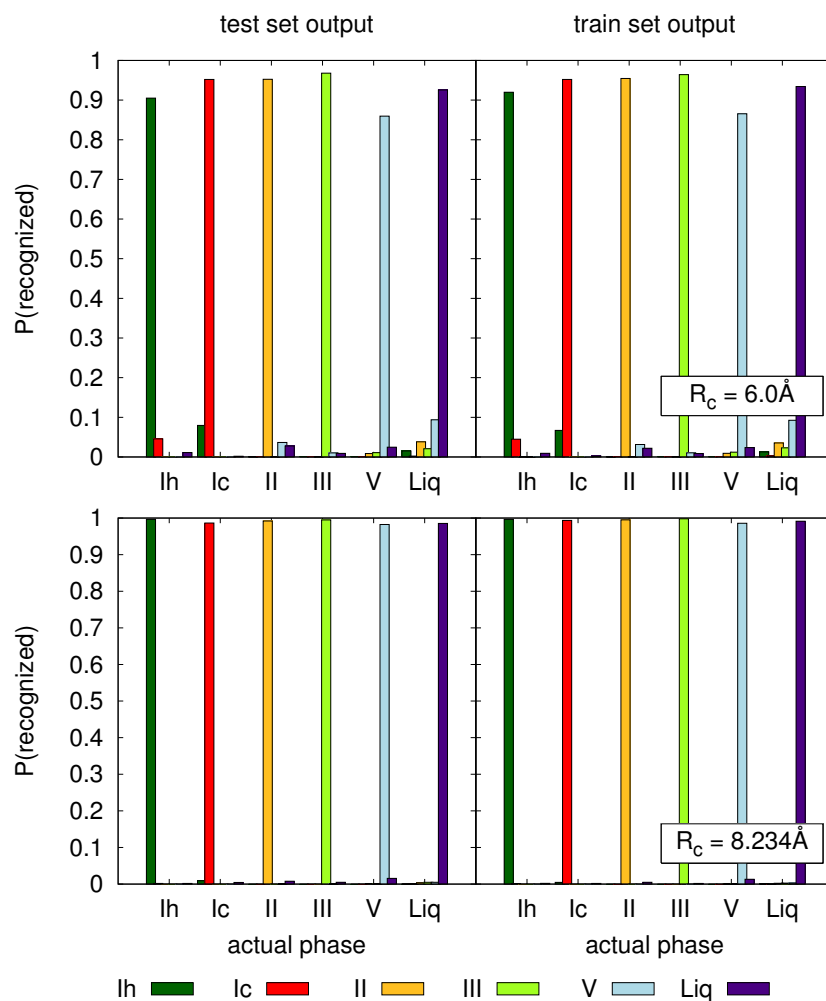


Figure 4.4.: Distribution of structures assigned by the neural network for the test set (left) and the training set (right) for liquid water and ice Ih, Ic, II, III, and V. For each of the different phases indicated on the x -axis, the heights of the colour-coded bars correspond to the fractions of structures that have been assigned the type specified by the color at the bottom. Results were obtained for a cutoff of $R_c = 6 \text{ \AA}$ (top) and for a cutoff of $R_c = 8.234 \text{ \AA}$ (bottom).

ter, as well as liquid/solid slab geometries in our training set. We generated these configurations fixing a fraction of the molecules to their respective positions in the perfect lattice using harmonic springs. Then we heated the system to melt the mobile molecules and subsequently relaxed it at 235 K with removed springs. Note that for the analysis, however, we have used a neural network that can distinguish between hexagonal and cubic ice.

To determine the free energy as a function of the order parameter we have used an umbrella sampling procedure with overlapping windows with hard walls. We study a system consisting of $N = 2880$ molecules at temperature $T = 235$ K and pressure of $P = 1$ atm, corresponding to 13% supercooling with respect to the melting temperature $T_{\text{melt}} = (270 \pm 3)$ K of TIP4P/ice model [142]. We chose this particular temperature such that the critical nucleus is of a size that fits in the simulation box. For this temperature, the growth rate of the crystalline nucleus is still sufficiently high such that the simulations are not hindered by the sluggish dynamics of water at low temperatures (see Weiss et al. [143] for a detailed study of crystal growth kinetics).

For each window, corresponding to a certain range of the order parameter, we have sampled NPT configurations using the hybrid Monte Carlo method [144], in which new configurations are generated by performing NVE molecular dynamics simulations. These short dynamical trajectories are computed without bias and the constraints on the order parameter imposed by the windows are taken into account only in the Monte Carlo acceptance step. We have integrated the equations of motion with a modified version of the algorithm of Miller et al. [138], which follows the algorithm of Omelyan [145]. This algorithm requires two force evaluations per integration step and exactly conserves phase space volume as required by the hybrid Monte Carlo scheme. Five molecular dynamics steps of length $\Delta t = 7.2$ fs are carried out for each short trajectory, yielding an acceptance probability of roughly 50%. To improve the sampling efficiency of the simulation we also carry out exchanges of configuration between adjacent windows following the replica exchange procedure of Auer and Frenkel [51]. We have carried out 5×10^6 equilibration HMC steps and 10^7 production HMC steps in each of the 40 windows. Histograms of the order parameter obtained from the each window are combined with the *self-consistent histogram* method [40] and the free energy is then obtained as the logarithm of the

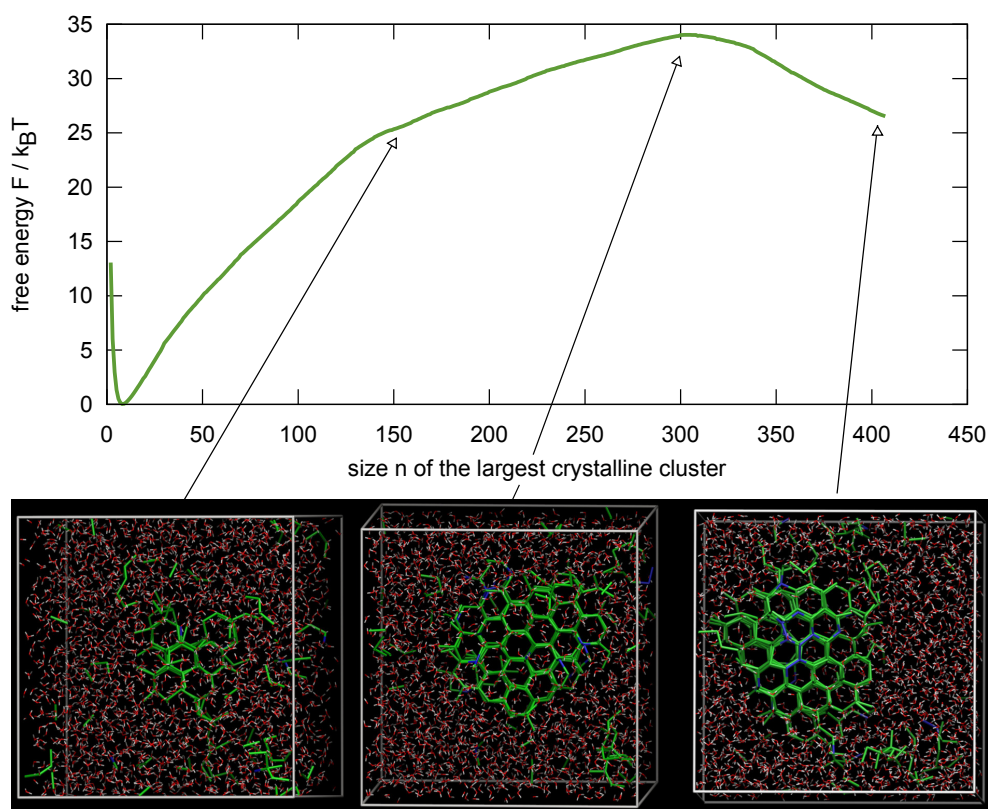


Figure 4.5.: Free energy $\beta F(n)$ as a function of the size n of the largest crystalline cluster for a system of $N = 2280$ TIP4P/ice water molecules at temperature $T = 235$ K and pressure $P = 1$ bar corresponding to 13% undercooling. The pictures at the bottom show snapshots of the system in different stages of the transition from liquid water to hexagonal ice, ice Ih. Crystalline hexagonal and cubic molecules and the bonds between them are shown in green and blue, respectively. The orientation of the each simulation box is such that the visibility of the crystalline structure is enhanced.

resulting distribution $P(n)$

$$F(n) = -k_B T \ln P(n).$$

The free energy $F(n)$ as a function of the size n of largest crystalline cluster obtained from our simulations is shown in Fig. 4.5. The shape of this free energy

profile with a barrier separating the supercooled state for small values of n from the completely crystalline state at large values of n is typical for a phase transition proceeding via nucleation and growth. In the picture of classical nucleation theory, which provides a qualitative description of nucleation processes, the barrier is due to the free energetic cost required to form an interface between the crystal nucleus and the surrounding metastable phase. Only after the crystalline nucleus reaches the so called critical size does the lower free energy of the crystalline phase prevail and the free energy decreases from this size on. This qualitative picture of the mechanism for crystallization is confirmed by the snapshots in the bottom row of Fig. 4.5, showing the system at different stages of the crystallization process. Note that the kink in the free energy profile visible at about $n = 140$ is most likely the result of insufficient sampling possibly due to slow shape equilibration.

Our calculations, carried out at $T = 235$ K and pressure $P = 1$ bar, yield a barrier height of $34 k_B T$ and a critical crystalline nucleus consisting of $n \sim 300$ molecules. This critical size is smaller than the critical cluster size of 615 molecules found by Li et al. at 235 K for the mW model, which has a melting point of 274.6 K [146]. These critical nuclei were identified from a dynamical criterion based on committor calculations such that no information on the height of the free energy barrier is available in this case. This discrepancy in the size of the critical nucleus might be due to difference in the water model, specifically in the melting point, the surface tension and in the heat of melting, but also to the different ways used to detect crystallinity.

Previous computer simulation studies carried out by Brukhno et al. [54] as well as Li et al. [137] have indicated that during the formation of hexagonal ice the crystalline nucleus may include regions of cubic ice. In contrast, our simulations yielded only crystalline nuclei with purely hexagonal structure. Single molecules with cubic environments were found only on the surface of the nucleus as can be seen in Fig. 4.5.

4.6. Summary and conclusions

In summary, we have developed an artificial neural network for the detection and the classification of local atomic structures. Different classes of atomic arrangements are distinguished based on a set of symmetry functions that capture the essential structural features and are invariant with respect to translations, rotations and per-

mutations of identical atoms. These symmetry functions are fed into the input layer of the neural network, which then performs a series of summations and non-linear operations that finally yield an output vector, in which each component corresponds to one of the structures to be recognized. Typically, our neural networks have 30 – 40 input nodes (one for each symmetry functions) and 2 hidden layers with about 40 nodes each. They depend on a few thousand parameters that provide the flexibility required to adapt the neural network to a variety of different structures. The parameters are tuned during a learning phase, in which the neural network is trained based on a training set consisting of several tens of thousands of local atomic configurations with known structure types. Such a training set, and an independent test set used to assess the quality of the structure recognition, can be prepared with molecular dynamics or Monte Carlo simulations performed in the pure phases. The neural networks developed here can be used to analyze the results of molecular dynamics and Monte Carlo simulations a posteriori, but also to drive such simulations to important but rarely visited regions of configuration space. Applying such a bias is, for instance, useful in studying nucleation phenomena which involve rare barrier crossing events. By applying the neural network method to the Lennard-Jones system as well as to water/ice we have demonstrated the this approach works well not only for simple phases but also for complex, open structures for which conventional structure recognition methods fail.

In the development of a neural network for structure recognition an appropriate definition of the symmetry functions is the most crucial step and the performance of the method strongly depends on the quality of the symmetry functions. The symmetry functions need to be designed such that they provide sufficient information to distinguish the various structures. Structural features gleaned from distributions of distances and angles can be useful in this process. While in this work we have used only symmetry functions of the type developed by Behler and Parrinello for energy calculations [58, 59], the structure recognition may be enhanced by adding also other structural fingerprints such as the Steinhard bond order parameters to the input for the neural network. In the application of the neural network the computation of the symmetry functions is usually the computationally most time-consuming step while the processing done by the neural network is relatively inexpensive. Therefore, it is advantageous to keep the number of symmetry functions as low as possible. A *sensitivity analysis*, which determines how strongly the output of a network depends on a particular input, may help to eliminate redundant symmetry functions without

sacrificing the accuracy of the structure detection.

Another important factor in the development of a neural network for structure detection is the generation of an appropriate training set. This set of configurations needs to include arrangements similar to all structures to which the neural network is eventually applied. Since the neural network is nothing else than a complicated fitting function, atomic structures that differ markedly from all structures included in the training set will not be assigned correctly. In practice, this implies that structures for the training set must be collected from simulations carried out over a broad range of pressures and temperatures. We have also found that it is important that configurations included in the training set are statistically independent from each other.

The range within which atoms are considered for the calculation of the symmetry function influences both the accuracy as well as the spatial resolution of the structure recognition. While including structural information from a large region around the central atom increases the accuracy of the method, it reduces its resolution and leads to unwanted averaging effects particularly near inhomogeneities such as interfaces and defects. Thus, particularly in the study of nucleation phenomena where interfaces between different phases play an important role, it is advisable to choose cutoffs that do not exceed those of other detection methods typically including atoms up to the second neighbor shell [50–52]. The general method developed here may be applied also to detect defects such as interstitials, vacancies and dislocations, in which case a small cutoff is particularly important. While in this thesis we have explored only the detection and classification of known structures, the neural networks developed here may also be used to search for new structures not included in the training set. For such structure two networks trained separately using the same training set should give conflicting answers raising the flag for the possible detection of a new structure.

4.7. Parameters of symmetry functions

In this section we list the parameters of the symmetry functions for the water system (Tab. 4.1). This particular set of symmetry functions is not unique. Sets containing G_5 , G_6 and G_7 type symmetry functions were found to give similar results.

Table 4.1.: Parameters of the symmetry functions for water and ice modeled with the TIP4P/Ice potential. The cutoff parameters used in this case are $R_c = 6 \text{ \AA}$, $\alpha_c = 30 \text{ \AA}^{-1}$, $\epsilon_c = 0.2 \text{ \AA}$ and $\nu = 5 \text{ \AA}^{-1}$.

| G_2 | $\eta (\text{\AA}^{-2})$ | $R_s (\text{\AA})$ | G_3 | $\kappa (\text{\AA}^{-2})$ | G_8 | $\alpha (1)$ | $\eta (1)$ | $a_l (\text{\AA})$ | $a_r (\text{\AA})$ |
|-------|--------------------------|--------------------|-------------|----------------------------|-------|--------------|------------|--------------------|--------------------|
| 1 | 0.049857 | 2.533440 | 14 | 0.157888 | 27 | 1.22 | 0.1375 | 2.00 | 3.15 |
| 2 | 0.138492 | 2.533440 | 15 | 0.315776 | 28 | 0.35 | 0.1000 | 2.00 | 6.00 |
| 3 | 0.406998 | 3.103464 | 16 | 0.473664 | 29 | 0.75 | 0.2275 | 2.00 | 6.00 |
| 4 | 0.553970 | 3.768492 | 17 | 0.631552 | 30 | 0.63 | 0.1825 | 2.00 | 6.00 |
| 5 | 0.797717 | 6.143592 | 18 | 1.420993 | 31 | 0.70 | 0.1000 | 3.00 | 4.00 |
| 6 | 1.246432 | 2.960958 | 19 | 1.736769 | 32 | 0.58 | 0.1000 | 3.15 | 6.00 |
| 7 | 1.246432 | 4.148508 | 20 | 1.894657 | 33 | 1.05 | 0.1075 | 3.15 | 6.00 |
| 8 | 1.246432 | 5.241054 | 21 | 2.526209 | 34 | 0.63 | 0.1825 | 3.15 | 6.00 |
| 9 | 2.215880 | 2.960958 | | | 35 | 1.05 | 0.1000 | 4.00 | 6.00 |
| 10 | 4.985730 | 2.770950 | | | | | | | |
| G_4 | $\eta (\text{\AA}^{-2})$ | | $\zeta (1)$ | $\lambda (1)$ | | | | | |
| 11 | 4.985730 | 3.293472 | 22 | 0.031578 | 10.0 | -1 | | | |
| 12 | 4.985730 | 4.766034 | 23 | 0.031578 | 10.0 | 1 | | | |
| 13 | 19.94292 | 3.103464 | 24 | 0.052629 | 6.0 | -1 | | | |
| | | | 25 | 0.083099 | 5.5 | -1 | | | |
| | | | 26 | 0.143535 | 14.0 | 1 | | | |

Chapter 5.

Technical aspects

Although a rather simple molecule, water requires very carefully considered implementation aspects for computer simulation, as illustrated by the large number of empirical model potentials for water developed over the last decades. It has turned out that there is no single model which is capable to describe all properties of water with the same degree of accuracy, but rather a large variety of well-developed models covering different classes of water properties.

In this chapter we introduce the empirical model and integrator we use, as well as details of the crystal generation and explain how electrostatic interactions are implemented.

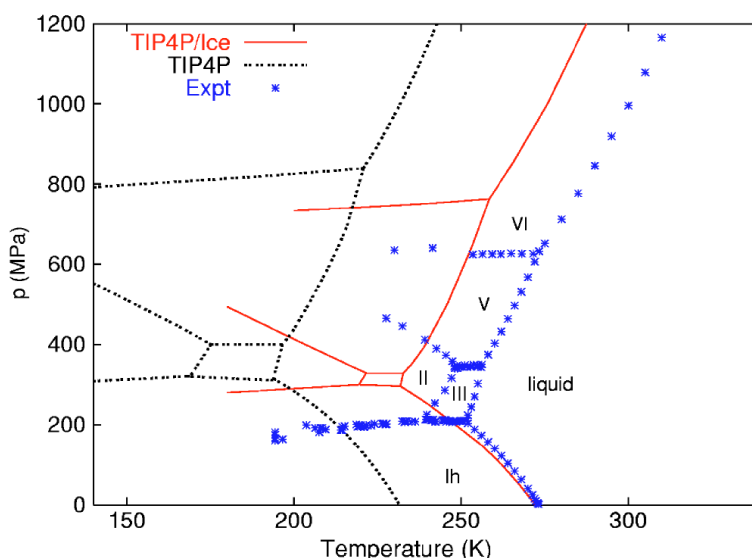


Figure 5.1.: Phase diagram of the TIP4P/Ice water model taken from Ref. [103]. The blue stars are experimental data points and the red lines are coexistence lines for the TIP4P/Ice model.

5.1. Modeling the water molecule

In the last decades many different model potentials for water in classical simulations have been employed [147]. While the majority of these models treats the water molecule as a rigid body by imposing geometrical constraints, many different approaches to model the water molecule under different conditions exist. In these rigid models the O-H bond distance and the H-O-H angle are kept constant and the electrostatic properties of water are modeled using three or more point charges at certain positions, usually the hydrogen atom positions and in vicinity of the oxygen*. The HOH-angle as well as the OH-bonds, the charges and the Lennard-Jones parameters, which model the Van-der-Wals interaction between the oxygen atoms, are free parameters which are fitted to reproduce either experimentally determined quantities or data provided by *ab initio* calculations.

For some studies rigid water models are not appropriate. For these cases flexible

* In models with more than three sites the effective charge of the oxygen is modeled by one or more point charges which are offset from the oxygen position to approximate the electron density of the water molecule.

models are available where a harmonic or Morse potential is used to describe the OH bond, thereby opening, for instance, the study of vibrational modes. Although due to the required short time step an increased computational cost has to be paid, integration techniques such as the *multiple time step* integrator developed by Tuckerman, Berne and Martyna [76, 148] exist to reduce the extra computational cost by increasing the maximum time step size. Essentially, this method separates the integration for degrees of freedom with a short relaxation time from those with a slower dynamics. In this algorithm, forces responsible for bond vibrations for instance, are calculated more often than those which are responsible for translative motion.

Another group of models features polarizability by including charge distributions which respond to the surrounding electric field. This kind of models are not discussed in this thesis.

In this work we are mainly interested in properties of solid water, thus we have chosen the recently developed water model TIP4P/Ice [103] which is fitted to experimental properties of low and high density ice. In this model (as is the case for all TIP4P-like models [149]) each molecule is represented by four interaction sites rigidly connected to each other. These sites, placed at the positions of the oxygen atom, the two hydrogen atoms and on the bisector of the HOH-angle, interact solely via pair potentials and polarization effects are neglected. While the oxygen atoms interact with each other only via a Lennard-Jones potential, all other interaction sites carry charges that interact Coulombically. Only the O and H site carry a mass, while the bisector site M is massless. The TIP4P/Ice model reproduces all ice phases consisting of intact water molecules and leads to a phase diagram with the correct topology and coexistence lines that are only slightly displaced with respect to the experimental phase diagram [150], as shown in Fig. 5.1. The model also yields an accurate prediction of the densities of the ice phases as well as the liquid phase.

5.2. Generation of ice crystal structures

In order to perform simulations of ice phases it is necessary to set up a simulation box with particle positions derived from the structure of real ice crystals. These initial conditions were constructed for each crystalline phase by taking the space group of a cell, its cell parameters and the fractional coordinates from literature. This information is then used to build the atomic arrangements used as initial configurations for our simulations.

As mentioned in Chapter 3, ice crystals can feature proton ordered arrangements. Here, molecules are orientated such that all hydrogens sit on a lattice, i.e., a crystallographic cell can be constructed from symmetry operations applied not only to the oxygens, but to all atoms (see Chapter 3 for details). While the proton ordered crystals are simply produced using the fractional coordinates for all oxygen and hydrogen atoms provided by literature, the disordered phases have to be generated in a way that obeys the Bernal-Fowler ice rules [79]. The Bernal-Fowler rules ensure the integrity of the ice crystal, i.e., each oxygen atom has covalent bonds to exactly two hydrogen atoms as well as H-bonds to exactly two neighboring oxygens.

Here, we have used the method developed by Rahman and Stillinger [107] and modified by Ayala and Tchijov [108] to generate permitted hydrogen atom disorder from proton ordered arrangements, which starts from a crystal with perfect proton order and protons located on the connecting lines between neighboring oxygens. The proton order is then disrupted by shifting protons from a position close to one oxygen to the position close to the neighboring oxygen originally accepting the hydrogen bond involving the shifted hydrogen. As a result, the neighboring oxygen has now three covalent bonds and only one hydrogen bond. The procedure is repeated for the neighboring water molecule, where one of the other two hydrogens forming a covalent bond is selected at random and shifted. In order to keep the water molecules in the sample intact, this shifting operation has to be carried out along closed loops of hydrogen bonds. This sequence of basic steps is repeated until every water molecule has been touched several times and a vanishing total dipole moment is achieved. At the end of the procedure, the ideal water molecules, which have a geometry consistent with perfect tetrahedral coordination, are replaced by molecules with TIP4P geometry.

In the following we give a list of the ice structure we use and their source in literature. For the proton ordered hexagonal ice two different H arrangements are studied (see Chapter 3), where both cells were taken from Ref. [98]. From this arrangement, disordered ice Ih was generated by applying the method described above to one of these two proton-ordered initial structures. As noted in detail in Chapter 3 cubic ice Ic and different proton ordered variants are generated according to Lekner [85]. The proton ordered ice II crystals were generated according to Ref. [151]. The atomic coordinates and hydrogen site occupancies for ice IX, the proton ordered counter part of ice III, were taken from Refs. [152, 153]. And finally, ice V and XIII were set up according to Refs. [80, 153].

5.3. Equilibrium sampling

When rigid water molecules are considered, the integration of the equations of motion for different ensembles necessitates a few extensions compared to simple single atom systems [154]. In the last decades integration schemes which generate the correct distributions of fluctuations of the state variables have been developed [155]. Such integrators were employed in order to generate configurations of desired ensembles for water. In particular, we have carried out molecular dynamics simulations in the NVT and isotropic NPT ensembles using a slightly modified version of the Verlet-like integrator proposed by Kamberaj et al. [139], based on the Trotter decomposition schemes applied by Miller et al. [138] and Martyna et al. [76]. In these integration schemes, the canonical and isothermal-isobaric ensembles are implemented through thermostat chains based on the Nosé-Hoover [156, 157] and the Andersen [158] approaches. An overview of these integrators is given in Appendix B.

The determination of the free energy profile of the liquid \rightarrow ice Ih transition was done using window sampling combined with self consistent histogramming [40]. In particular, we have employed hard window walls, i.e., no umbrella function was used and no bias added in the Metropolis Monte Carlo acceptance criterion. For each of the overlapping windows we have sampled NPT configurations using the *hybrid Monte Carlo* (HMC) method [144]. New configurations for each HMC step were generated by performing NVE molecular dynamics. Instead of Miller's integrator [138] we have employed a higher order Trotter decomposition according to Omelyan [145] which performs better compared to the former one. Although Miller's algorithm is fully time-reversible, which is a required property of the integrator when performing HMC, it can only be used with a maximum time step of 1 to 2 fs when doing 5 MD steps of a typical system size for the HMC procedure. On the other hand when using a decomposition according to Omelyan, where the center of mass degrees of freedom are propagated more accurately, a time step of 9 fs for the same system size can be used in order to achieve acceptance rates of 50 to 60%. Note that in the HMC scheme the maximum size of the time step depends on the number of steps performed at each HMC step as well as the size of the system. A possible reason for the better accuracy of the Omelyan algorithm lies in the fact that the Verlet algorithm is accurate to $\mathcal{O}(\Delta t^4)$ for the positions but only to $\mathcal{O}(\Delta t^2)$ for the momenta. For the energy fluctuations within the hybrid Monte Carlo scheme this

asymmetry yields an $\mathcal{O}(\Delta t^2)$ overall algorithm. The Omelyan algorithm is symmetric with respect to positions and momenta, but requires two force calculations for one integration step instead of one. In particular, for the window sampling of the hexagonal ice system consisting of 2880 molecules we have used a time step of 7.2 fs and 5 MD steps for each HMC step.

The long range interactions are treated using Ewald summation with 1152 k -vectors to ensure a good convergence of the Coulombic potential and forces in the reciprocal space (see Sec. 5.4 for details).

In order to provide a convenient way for the implementation of water in a computer simulation, we have employed a commonly used set of units. This choice also aids the comparison with other results from literature. In particular, we use the following set of units: for length angstroms, for time femtoseconds, for the energy kilojoules per mole and for the charge we use the elementary charge. Furthermore, the Boltzmann constant is set to unity, thereby fixing the unit of temperature.

5.4. Electrostatic interactions

The TIP4P model incorporates three point charges located on the two H sites and on the massless site on the symmetry axis of the molecule slightly off the O position, respectively. While for finite systems the Coulombic $1/r$ interaction can be computed in a straightforward manner, the necessary truncation of the potential in periodic systems leads to incorrect results. For rapidly decaying potentials the error due to truncation at a comparatively large cutoff is well defined. In three dimensions, this means that the integral over the potential beyond this cutoff converges,

$$\int_{r_{\text{cut}}}^{\infty} dr r^2 u(r) < \infty. \quad (5.1)$$

Such convergence is possible only for potentials which decay faster than $1/r^3$. To account for the much slower decay of the electrostatic potential, a special ansatz has to be employed. Many useful techniques exist in literature, as for instance the *Lekner summation* [159] or the *reaction field* method [160, 161]. Nevertheless, a widely used method is the so-called Ewald summation technique [40, 162], where the $1/r$ point charges are replaced by charges which are screened by Gaussian charge clouds. To correct for this additional charge distributions a screening background is introduced which compensates for the Gaussians. Mathematically, this artifice splits the total

potential energy into three terms: one which converges in the real space, another which converges in the reciprocal space and a correction term. Thus, the potential can be written as

$$U = U_{\text{real}} + U_{\text{rec}} + U_{\text{corr}}. \quad (5.2)$$

Explicitly, these terms are

$$U_{\text{real}} = \frac{k_e}{2} \sum_i \sum_{\alpha} \sum_{j \neq i} q_{i\alpha} \sum_{\beta} q_{j\beta} \frac{\text{erfc}(\kappa r_{i\alpha j\beta})}{r_{i\alpha j\beta}}, \quad (5.3)$$

$$U_{\text{rec}} = k_e \frac{2\pi}{V} \sum_{\mathbf{k} \neq 0} Q(k) S(\mathbf{k}) S(-\mathbf{k}), \quad (5.4)$$

$$U_{\text{corr}} = -k_e \frac{\kappa}{\sqrt{\pi}} \sum_i \sum_{\alpha} q_{i\alpha}^2 - \frac{k_e}{2} \sum_i \sum_{\alpha} \sum_{\beta \neq \alpha} q_{i\alpha} q_{i\beta} \frac{\text{erf}(\kappa r_{i\alpha i\beta})}{r_{i\alpha i\beta}}, \quad (5.5)$$

where $Q(\mathbf{k})$ and the atomic structure factor $S(\mathbf{k})$ are defined as

$$S(\mathbf{k}) = \sum_i \sum_{\alpha} q_{i\alpha} \exp(i\mathbf{k} \cdot \mathbf{r}_{i\alpha j\beta}), \quad (5.6)$$

and

$$Q(k) = \frac{1}{k^2} \exp\left(\frac{-k^2}{4\kappa^2}\right). \quad (5.7)$$

In the formulas above, the indices i and j run over all molecules and α and β over their corresponding charged sites, denoted as $q_{i\alpha}$ and $q_{j\beta}$, respectively. The distance of interaction sites located on distinct molecules is given by $\mathbf{r}_{i\alpha j\beta} = \mathbf{r}_{i\alpha} - \mathbf{r}_{j\beta}$ and the reciprocal lattice vector by $\mathbf{k} = 2\pi(n_1/L_x, n_2/L_y, n_3/L_z)^T$, where the n_i are integers ranging from $-n_{\text{max}}$ to $+n_{\text{max}}$. The condition $|\mathbf{n}|^2 \leq n_{\text{max}}^2$ restricts the used k -vectors to lie within an ellipsoid. In the definition of the k -vector we have implicitly assumed a rectangular simulation box, thus the system volume is given by $V = L_x L_y L_z$. The Coulomb constant is $k_e = 1/(4\pi\epsilon_0)$, where ϵ_0 is the vacuum permittivity and κ is a tunable Ewald parameter. The correction part U_{corr} consists of 2 terms, where the first one corrects for the point self-energy and the second one corrects for interactions between charges of the same molecule, which are included in the reciprocal sum (Eq. (5.4)).

The force acting on atom α of molecule i is calculated by taking the negative gradient of Eq. (5.2),

$$\mathbf{F}_{i\alpha} = -\underbrace{\frac{\partial U_{\text{real}}}{\partial \mathbf{r}_{i\alpha}}}_{\mathbf{F}_{i\alpha}^{\text{real}}} - \underbrace{\frac{\partial U_{\text{rec}}}{\partial \mathbf{r}_{i\alpha}}}_{\mathbf{F}_{i\alpha}^{\text{rec}}} - \underbrace{\frac{\partial U_{\text{corr}}}{\partial \mathbf{r}_{i\alpha}}}_0, \quad (5.8)$$

$$\mathbf{F}_{i\alpha}^{\text{real}} = k_e q_{i\alpha} \sum_{j \neq i} \sum_{\beta} q_{j\beta} \left[\frac{2}{\sqrt{\pi}} \kappa r_{i\alpha j\beta} \exp(-\kappa^2 r_{i\alpha j\beta}^2) \right. \quad (5.9)$$

$$\left. + \operatorname{erfc}(\kappa r_{i\alpha j\beta}) \right] \frac{\mathbf{r}_{i\alpha j\beta}}{r_{i\alpha j\beta}^3}, \quad (5.10)$$

$$\mathbf{F}_{i\alpha}^{\text{rec}} = -k_e q_{i\alpha} \left\{ \frac{4\pi}{V} \sum_{\mathbf{k} \neq 0} Q(k) \mathbf{k} \Im \left[\exp(-i \mathbf{k} \cdot \mathbf{r}_{i\alpha}) S(\mathbf{k}) \right] \right\}, \quad (5.11)$$

where $\Im[x]$ denotes the imaginary part of x . The stress tensor (see Refs. [163, 164]) is given by

$$\begin{aligned} VP_{ab} = & \frac{k_e}{2} \sum_i \sum_{\alpha} q_{i\alpha} \sum_{j \neq i} \sum_{\beta} q_{j\beta} \left[\frac{2}{\sqrt{\pi}} \kappa r_{i\alpha j\beta} \exp(-\kappa^2 r_{i\alpha j\beta}^2) \right. \\ & \left. + \operatorname{erfc}(\kappa r_{i\alpha j\beta}) \right] \frac{(\mathbf{r}_{ij})_a (\mathbf{r}_{i\alpha j\beta})_b}{r_{i\alpha j\beta}^3} \\ & + k_e \left[\frac{2\pi}{V} \sum_{\mathbf{k} \neq 0} Q(k) S(\mathbf{k}) S(-\mathbf{k}) \left(\delta_{ab} - \frac{2\mathbf{k}_a \mathbf{k}_b}{k^2} - \frac{\mathbf{k}_a \mathbf{k}_b}{2\kappa^2} \right) \right] \\ & - \sum_i \sum_{\alpha} (\mathbf{r}_{i\alpha} - \mathbf{r}_i)_b (\mathbf{F}_{i\alpha}^{\text{rec}})_a, \end{aligned} \quad (5.12)$$

with the Kronecker delta δ_{ab} .

Although the method of Ewald summation has only one free parameter to optimize, the task of finding a good prescription for κ is not trivial. Particularly for constant pressure dynamics, where the box can fluctuate such that the volume of the system can change significantly, a re-evaluation of this parameter at every time step might be necessary. Another circumstance which one has to consider is the advantageous use of a real-space cutoff smaller than half of the smallest cell length. The usage of a real space cutoff, which truncates the potential at a certain distance, significantly reduces the program execution times by reducing the number of interaction partners as well as permitting the employment of $\mathcal{O}(N)$ algorithms like the *linked lists* or *Verlet lists* methods [40, 162], respectively.

5.4.1. Convergence parameter

For a cutoff fixed to the half box length many good prescriptions for choosing κ exist [165, 166]. In addition, there are studies where the influence of the cutoff on the Ewald parameter κ has been investigated in detail [167–169]. We propose a formula

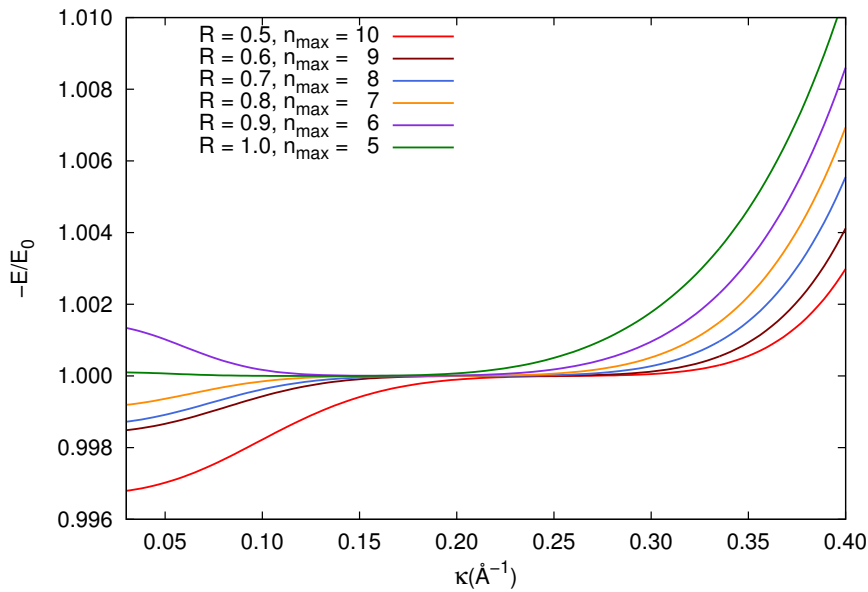


Figure 5.2.: Typical convergence behavior of the Coulomb energy as a function of the Ewald parameter κ . These particular curves were computed for an equilibrium NVT configuration at $T = 300$ K, $\rho = 1000$ kg/m³ with $N = 2000$ molecules using the TIP4P water potential. The Coulomb energy is scaled by its optimal value, which occurs where the slope of the function is zero. $R = 2r_{\text{cut}}/L$ is the scaled cutoff, defined as described in the main text.

for water, which is inspired by the expressions found by Rycerz [168] for other ionic systems. While our procedure of finding this prescription is closely related to the one of Rycerz, the results differ in their analytical form.

We have calculated Coulomb energies for different equilibrium configurations of different system sizes (ranging from hundreds to many thousands of water molecules) and different densities ranging from 850 to 1300 kg/m³.

Fig. 5.2 shows the Coulomb energy as a function of the Ewald parameter κ for an arbitrary configuration. One can see that the function is forming a plateau over a rather wide range of κ values. On the left hand side, i.e., better convergence of the Ewald sum in the reciprocal space, the plateau is bordered by insufficient decay of the error function within the cutoff, where the right border is determined by

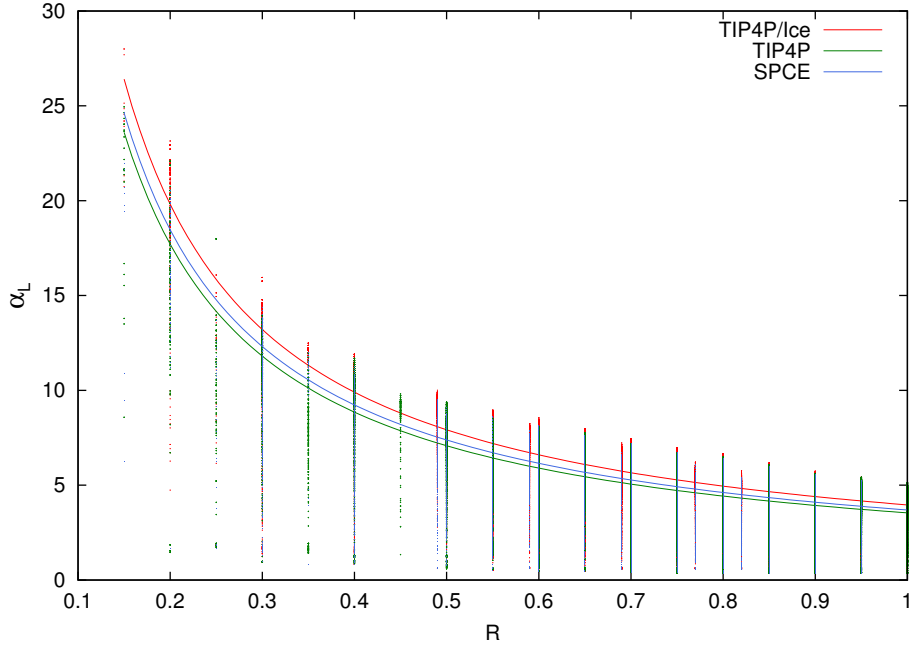


Figure 5.3.: Dependence of the left plateau border α_L from a scaled cutoff R . Here, we show results for several NVT configurations at $T = 300$ and various densities and system sizes (points). The solid lines are fits using the functional form $\alpha_L(R) = a_c/R$, where a_c is the fit parameter.

the number of terms in the reciprocal part of the Ewald sum ($\sim n_{\max}^2$). For a set number of k -vectors and a fixed cutoff the interaction converges for an interval of κ values which is indicated by the plateaus in Fig. 5.2. Thus, the goal is to find an optimal value within a certain range which both optimizes the number of terms in the reciprocal part of the Ewald sum and the decay of the complementary error function.

To quantify the plateau boundaries we define the plateau value E_0 as the value of the single curve minimum or else as the value of the point of inflection if the curve has no minimum. Furthermore, we define the border of the plateau as the last points α_L, α_R which are within a small interval around the plateau value $|E - E_0|/E_0 < \varepsilon$. In our case we use $\varepsilon = 0.0002$. Following Ref. [167], we employ the dimensionless cutoff $R = 2r_{\text{cut}}/L$, scaled in units of the box length and a scaled Ewald parameter $\alpha = L\kappa$.

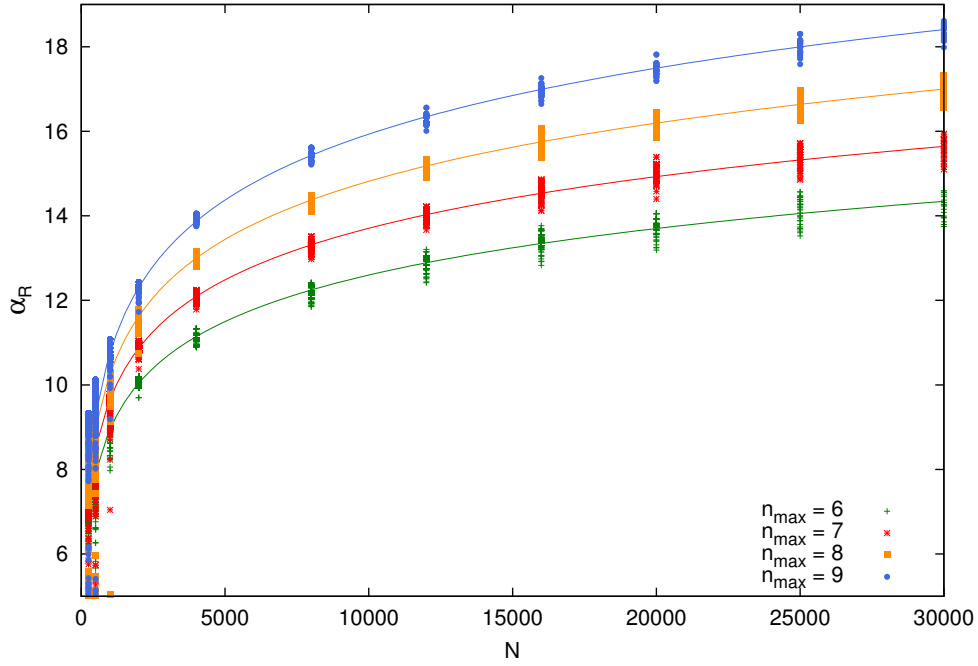


Figure 5.4.: Fits to the right plateau border with respect to the system size for four different values of n_{\max} corresponding to $k_{\max} = 518, 783, 1152$ and 1661 .

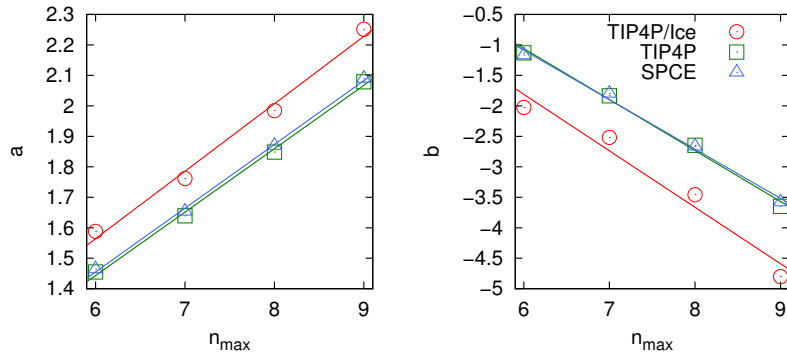


Figure 5.5.: Linear regression fits for the n_{\max} dependence of Eq. (5.15).

In order to construct an empirical formula describing the left boundary of the plateau we calculate a fit to the left plateau borders α_L , determined using the definition above, as a function of the scaled real space cutoff (shown in Fig. 5.3). Each point represents a result for a single configuration rather than an equilibrium average. The analytic form is obtained by fitting the function

$$\alpha_L(R) = a_c/R. \quad (5.13)$$

This was done for the data of three different water models: TIP4P [170], TIP4P/Ice (Sec. 5.1) and SPC/E [171]. The resulting fit parameters a_c are given in Tab. 5.1.

The right border of the plateau is mainly influenced by the system size and the maximum number of k -vectors used. In Fig. 5.4 we plot the right plateau boundary α_R for all studied system sizes N and all densities ρ for four different numbers of k -vectors. Here we have used the function

$$\alpha_R(N) = a_r \ln(N) + b_r, \quad (5.14)$$

to fit the data for each value of n_{\max} . Fig. 5.4 only shows results for TIP4P/Ice, since the results for TIP4P and SPC/E are qualitatively very similar. To account for the n_{\max} dependency we have assumed $a_r = a_r(n_{\max})$ and $b_r = b_r(n_{\max})$, respectively. In the two plots of Fig. 5.5 one can see the linear fits for $a_r(n_{\max}) = k_a n_{\max} + d_a$ and $b_r(n_{\max}) = k_b n_{\max} + d_b$. The final formula is then given by

$$\alpha_R(N, n_{\max}) = (k_a n_{\max} + d_a) \ln(N) + k_b n_{\max} + d_b. \quad (5.15)$$

Numerical values for the fits in Fig. 5.5 are given in Tab. 5.1.

Merging Eq. (5.13) and Eq. (5.15) together we can give a very accurate estimate of a good Ewald parameter with both a good convergence in real space as well as in reciprocal space

$$\kappa_{\text{opt}} = \frac{\alpha_{\text{opt}}(N, R, n_{\max})}{L} = \frac{1}{2L} [\alpha_L(R) + \alpha_R(N, n_{\max})]. \quad (5.16)$$

Table 5.1.: Fit parameter a_c for the left plateau border α_L of Eq. (5.13) and fit parameters k_a , d_a , k_b and d_b for the right plateau border α_R of Eq. (5.15) for different water models.

| model | a_c | k_a | d_a | k_b | d_b |
|-----------|--------|----------|----------|-----------|----------|
| TIP4P | 3.5409 | 0.208068 | 0.194845 | -0.836485 | 3.959020 |
| SPC/E | 3.6925 | 0.209186 | 0.200055 | -0.810547 | 3.775885 |
| TIP4P/Ice | 3.9613 | 0.221274 | 0.236740 | -0.926862 | 3.750335 |

Part III.

Appendices

Appendix A.

Determination of linearized equation of motion for pair potentials

A dynamical system, consisting of N particles of mass m and described by the Hamiltonian \mathcal{H} evolves in time according to the equations of motions

$$\begin{aligned}\dot{\mathbf{r}}_i &= \frac{\partial \mathcal{H}}{\partial \mathbf{p}_i} = \mathbf{p}_i/m, \\ \dot{\mathbf{p}}_i &= -\frac{\partial \mathcal{H}}{\partial \mathbf{r}_i} = \mathbf{F}_i,\end{aligned}\tag{A.1}$$

derived from the Hamiltonian

$$\mathcal{H} = \sum_{i=1}^N \frac{\mathbf{p}_i^2}{2m} + \Phi(\mathbf{r}_1, \dots, \mathbf{r}_N).\tag{A.2}$$

Here \mathbf{r}_i is the position vector, \mathbf{p}_i the momenta vector of the particle i and Φ the potential energy. For the sake of simplicity, we introduce the phase space vector $\mathbf{x} = \{\mathbf{r}_1, \dots, \mathbf{r}_N, \mathbf{p}_1, \dots, \mathbf{p}_N\}$ and write the equations of motion by

$$\dot{\mathbf{x}} = \mathbf{\Gamma}(\mathbf{x}).\tag{A.3}$$

Now, we consider the environment of an arbitrary point in the system's phase space. We introduce an infinitesimal displacement vector $\delta\mathbf{x}$, which denotes a deviation of the given trajectory at a particular point. This perturbed trajectory evolves according to

$$\frac{d}{dt}(\mathbf{x} + \delta\mathbf{x}) = \mathbf{\Gamma}(\mathbf{x} + \delta\mathbf{x}) \approx \mathbf{\Gamma}(\mathbf{x}) + \mathbf{D}\mathbf{\Gamma}|_{\mathbf{x}} \cdot \delta\mathbf{x},\tag{A.4}$$

where $\mathbf{D}\mathbf{\Gamma}|_{\mathbf{x}}$ is the Jacobi matrix of the vector function $\mathbf{\Gamma}$, determined at the perturbation point \mathbf{x} . Hence, the deviation vector evolves in tangent space according

to the linearized equations of motion

$$\frac{d}{dt}\delta\mathbf{x} = \mathbf{D}\mathbf{\Gamma}|_{\mathbf{x}} \cdot \delta\mathbf{x}. \quad (\text{A.5})$$

In the following we give the derivation of a general expression for this Jacobi matrix for a system of particles interacting only via pair potentials. If the forces are only functions of the positions $\mathbf{F}_i = \mathbf{F}_i(\mathbf{r}_i)$, i.e., no friction term, then the Jacobi matrix is of the form

$$\mathbf{D}\mathbf{\Gamma} = \left(\begin{array}{c|c} 0 & \mathbf{1} \\ \hline -\mathbf{H} & 0 \end{array} \right), \quad (\text{A.6})$$

where $(\mathbf{H}_{ij}) = \left(\frac{\partial^2}{\partial \mathbf{r}_i \partial \mathbf{r}_j} \Phi \right)$ is the Hessian matrix of the potential. For reasons of simplicity we divide the Hessian matrix into the 3×3 sub-matrices

$$\mathbf{A}_{ij} = \left(\frac{\partial}{\partial \mathbf{r}_i} \mathbf{F}_j \right), \quad (\text{A.7})$$

which correspond to the Jacobian matrix of \mathbf{F}_j with respect to the positional coordinates \mathbf{r}_i . In the following we denote the x -component of the vector \mathbf{r}_i by r_i^x , the distance vector of two particles by $\mathbf{r}_{ij} = \mathbf{r}_j - \mathbf{r}_i$ and one of its components by $r_{ij}^x = r_j^x - r_i^x$. For the distance between two particles we introduce $r_{ij} = |\mathbf{r}_{ij}|$. First we rewrite the expression in Eq. (A.7) as

$$\mathbf{A}_{ij} = -\frac{\partial}{\partial \mathbf{r}_i} \frac{\partial}{\partial \mathbf{r}_j} \Phi = -\frac{1}{2} \sum_m \sum_n \frac{\partial}{\partial \mathbf{r}_i} \frac{\partial}{\partial \mathbf{r}_j} \Phi_{mn} \quad (\text{A.8})$$

and since $\Phi_{ij} = \Phi_{ij}(r_{ij})$ we can write the gradient of the potential as

$$\frac{\partial}{\partial \mathbf{r}_j} \Phi_{mn} = \underbrace{\left(\frac{d}{dr_{mn}} \Phi_{mn} \right)}_{\Phi'_{mn}} \frac{\mathbf{r}_{mn}}{r_{mn}} (\delta_{nj} - \delta_{mj}), \quad (\text{A.9})$$

where δ_{ij} is the Kronecka Delta. Using $\gamma_{mn} = r_{mn}^{-1} \Phi'_{mn}$ Eq. (A.8) becomes

$$\begin{aligned} \mathbf{A}_{ij} &= -\frac{1}{2} \sum_m \sum_n \frac{\partial}{\partial \mathbf{r}_i} \gamma_{mn} \mathbf{r}_{mn} (\delta_{nj} - \delta_{mj}) \\ &= -\frac{1}{2} \sum_m \frac{\partial}{\partial \mathbf{r}_i} \gamma_{mj} \mathbf{r}_{mj} + \frac{1}{2} \sum_n \frac{\partial}{\partial \mathbf{r}_i} \gamma_{jn} \mathbf{r}_{jn} \\ &= -\sum_m \begin{bmatrix} \left(\frac{\partial}{\partial \mathbf{r}_i} \gamma_{mj} r_{mj}^x \right)^\top \\ \vdots \\ \left(\frac{\partial}{\partial \mathbf{r}_i} \gamma_{mj} r_{mj}^z \right)^\top \end{bmatrix}, \end{aligned} \quad (\text{A.10})$$

where in the last equation we have used that $\mathbf{r}_{jm} = -\mathbf{r}_{mj}$. For the row elements of these matrices we get

$$\frac{\partial}{\partial \mathbf{r}_i} \gamma_{mj} r_{mj}^x = r_{mj}^x \underbrace{\frac{\partial}{\partial \mathbf{r}_i} \gamma_{mj}}_{\otimes} + \gamma_{mj} \underbrace{\frac{\partial}{\partial \mathbf{r}_i} r_{mj}^x}_{(\delta_{ij} - \delta_{im}) \hat{e}_x}, \quad (\text{A.11})$$

$$\otimes = \frac{\partial}{\partial \mathbf{r}_i} \Phi'_{mj} r_{mj}^{-1} = r_{mj}^{-1} \Phi''_{mj} \frac{\mathbf{r}_{mj}}{r_{mj}} (\delta_{ij} - \delta_{im}) - \Phi'_{mj} \frac{\mathbf{r}_{mj}}{r_{mj}^3} (\delta_{ij} - \delta_{im}). \quad (\text{A.12})$$

Using identical derivations for the other components we obtain

$$\begin{aligned} \frac{\partial}{\partial \mathbf{r}_i} \gamma_{mj} r_{mj}^x &= [\chi_{mj} \mathbf{r}_{mj} r_{mj}^x + \gamma_{mj} \hat{e}_x] (\delta_{ij} - \delta_{im}), \\ \frac{\partial}{\partial \mathbf{r}_i} \gamma_{mj} r_{mj}^y &= [\chi_{mj} \mathbf{r}_{mj} r_{mj}^y + \gamma_{mj} \hat{e}_y] (\delta_{ij} - \delta_{im}), \\ \frac{\partial}{\partial \mathbf{r}_i} \gamma_{mj} r_{mj}^z &= [\chi_{mj} \mathbf{r}_{mj} r_{mj}^z + \gamma_{mj} \hat{e}_z] (\delta_{ij} - \delta_{im}), \end{aligned} \quad (\text{A.13})$$

where

$$\chi_{mj} = \frac{\Phi''_{mj}}{r_{mj}^2} - \frac{\gamma_{mj}}{r_{mj}^2}. \quad (\text{A.14})$$

Then Eq. (A.10) becomes

$$\mathbf{A}_{ij} = - \sum_m (\delta_{ij} - \delta_{im}) [\chi_{mj} \mathbf{Q}_{mj} + \mathbf{G}_{mj}], \quad (\text{A.15})$$

where

$$\mathbf{Q}_{mj} = \begin{pmatrix} r_{mj}^x r_{mj}^x & r_{mj}^x r_{mj}^y & r_{mj}^x r_{mj}^z \\ r_{mj}^y r_{mj}^x & r_{mj}^y r_{mj}^y & r_{mj}^y r_{mj}^z \\ r_{mj}^z r_{mj}^x & r_{mj}^z r_{mj}^y & r_{mj}^z r_{mj}^z \end{pmatrix}, \quad \mathbf{G}_{mj} = \begin{pmatrix} \gamma_{mj} & 0 & 0 \\ 0 & \gamma_{mj} & 0 \\ 0 & 0 & \gamma_{mj} \end{pmatrix}. \quad (\text{A.16})$$

Finally the sum over the Kronecka delta yields

$$\mathbf{A}_{ij} = \begin{cases} - \sum_m [\chi_{mj} \mathbf{Q}_{mj} + \mathbf{G}_{mj}] & \text{if } i = j, \\ \chi_{ij} \mathbf{Q}_{ij} + \mathbf{G}_{ij} & \text{else.} \end{cases} \quad (\text{A.17})$$

In addition, introducing the dyadic product \otimes we can rewrite the last equation to

$$\mathbf{A}_{ij} = \begin{cases} - \sum_m \left[\Phi''_{mj} \hat{\mathbf{r}}_{mj} \otimes \hat{\mathbf{r}}_{mj} + \frac{\Phi'_{mj}}{r_{mj}} (\mathbf{1}_3 - \hat{\mathbf{r}}_{mj} \otimes \hat{\mathbf{r}}_{mj}) \right] & \text{if } i = j, \\ \Phi''_{ij} \hat{\mathbf{r}}_{ij} \otimes \hat{\mathbf{r}}_{ij} + \frac{\Phi'_{ij}}{r_{ij}} (\mathbf{1}_3 - \hat{\mathbf{r}}_{ij} \otimes \hat{\mathbf{r}}_{ij}) & \text{else,} \end{cases} \quad (\text{A.18})$$

with $\hat{\mathbf{r}}_{ij} = \mathbf{r}_{ij}/r_{ij}$ and the 3×3 unity matrix is denoted by $\mathbf{1}_3$.

This derivation is valid for all pair potentials, i. e., where the value of the potential only depends on the distances between particles and can be used to determine Lyapunov exponents, as presented in chapter 1, or the calculation of second order corrections for the Raman spectrum of water in the O-H bond stretching regime [130, 172].

For the Ewald summation technique, where the potential depends not only on the distance of the particles, but also on its absolute positions within the simulation box, a separate derivation is required, which is given in the appendix of Ref. [130].

Appendix B.

Time-propagation of rigid water molecules in various ensembles

The use of a non-flexible water model makes it necessary to employ advanced simulation methods. In particular, here, we consider the proper treatment of rigid bodies and the Ewald summation to calculate Coulombic interactions. The rigidity of the water molecules can be ensured either by introducing Lagrangian constraint forces to the system [162], or by propagating the Euler equations for the rotation of a rigid body rather than the propagation of each individual atom [162]. The latter approach has the advantage that integration schemes can be derived which conserve time reversibility. This property is not only beneficial for the HMC scheme, where large time steps are only achieved for time-reversible integrators, but also indispensable for techniques like transition path sampling [6] and transition interface sampling [173]. In the following we present integrators based on a quaternion representation of the molecule orientation rather than the Euler angles. This representation avoids singularities and also allows the derivation of symplectic and time-reversible integrators.

B.1. Mathematical basics

In order to understand the integrators presented in this appendix correctly, it is necessary to recall some mathematical fundamentals first.

While we use a roman numeral as index for the molecules, we number the atoms in a molecule with a greek letter. For instance, $\mathbf{r}_{i\alpha}$ is the position of atom α of molecule i , $\mathbf{v}_{i\alpha}$ its velocity, $m_{i\alpha}$ its mass and so on. The molecule index runs from $i = \{1, \dots, n_m\}$ and the atom (or site) index $\alpha = \{1, \dots, n_a\}$, where n_m is the number

of molecules and n_a the number of atoms within this molecule. This notation is consistently used throughout this appendix. Next, we define the center of mass of the i -th molecule by

$$\mathbf{R}_i = \frac{1}{M_i} \sum_{\alpha=1}^{n_a} m_{\alpha} \mathbf{r}_{i\alpha},$$

where M_i is its total mass and the center of mass momentum is given by

$$\mathbf{P}_i = \sum_{\alpha=1}^{n_a} m_{\alpha} \mathbf{v}_{i\alpha}.$$

To describe the motion of rigid bodies two coordinate systems are used: the space fixed system (SS), where all coordinates are given with respect to a origin, usually the center or a corner of the simulation box, and the body fixed coordinate systems (BS), where the coordinate basis is fixed to the axis of the rigid molecule. The latter coordinate system is used to derive the rotational part of the equations of motions for a rigid body, the so-called Euler equations. An important quantity entering the Euler equations is the moment of inertia tensor, which plays a similar role for rotations as the mass does for translations. This tensor is defined by

$$I_{ij} = \sum_{\alpha=1}^{n_a} m_{\alpha} [(r_{\alpha}^*)^2 \delta_{ij} - (\mathbf{r}_{\alpha}^*)_i \otimes (\mathbf{r}_{\alpha}^*)_j] \quad i, j = \{1, 2, 3\},$$

where $(\mathbf{r}_{\alpha}^*)_i$ is the i -th component of the distance vector from the origin to the α -th site in the BS (indicated by a star *), r_{α}^* its distance and \otimes the dyadic product. For the sake of simplicity we choose the BS identical to the principal axis system by setting the origin in the center of mass of the molecule and rotating the molecule until a diagonal inertia tensor is achieved. This is easily done by geometrical consideration (at least for simple molecules) or with principal axis transformation (for any kind of complexity).

Given the relation between the angular velocity and the angular momentum $\mathbf{L} = \mathbf{I} \cdot \boldsymbol{\omega}$ and the equation of motion $\frac{d}{dt} \mathbf{L} = \mathbf{M}$, where \mathbf{M} is the torque, it is easy to show that the rotational degrees of freedom of a rigid body obey the Euler equations [174]

$$\begin{aligned} I_{11} \dot{\omega}_1^* + (I_{33} - I_{22}) \omega_2^* \omega_3^* &= M_1^*, \\ I_{22} \dot{\omega}_2^* + (I_{11} - I_{33}) \omega_1^* \omega_3^* &= M_2^*, \\ I_{33} \dot{\omega}_3^* + (I_{22} - I_{11}) \omega_1^* \omega_2^* &= M_3^*. \end{aligned} \tag{B.1}$$

The torque is defined by

$$\mathbf{M}^* = \sum_{\alpha=1}^{n_a} \mathbf{d}_{\alpha}^* \times \mathbf{F}_{i\alpha}^*, \quad (\text{B.2})$$

where $\mathbf{F}_{i\alpha}^*$ is the force on site α of molecule i in the BS.

As noted above, we use quaternions [175] rather than Euler angles to describe the orientational motion of the water molecules since this leads to fast and time-reversible integrators. Furthermore, we avoid singularities which are implicitly included in the Euler angle representation.

A quaternion is a hypercomplex number

$$q = q_0 + i \cdot q_1 + j \cdot q_2 + k \cdot q_3,$$

which is usually written as the four dimensional vector $(q_0, q_1, q_2, q_3)^T$. i , j and k are imaginary numbers with $i^2 = j^2 = k^2 = -1$. A pair of quaternions can be used to store the information of a molecule's rotation and its time propagation, i.e., the Euler equations (Eq. B.1) can be rewritten for the quaternion representation. The conversion from the Euler angle representation to the quaternion representation is given by

$$\begin{aligned} q_0 &= \cos \frac{\theta}{2} \cos \frac{\phi + \psi}{2}, \\ q_1 &= \sin \frac{\theta}{2} \cos \frac{\phi - \psi}{2}, \\ q_2 &= \sin \frac{\theta}{2} \sin \frac{\phi - \psi}{2}, \\ q_3 &= \cos \frac{\theta}{2} \sin \frac{\phi + \psi}{2}, \end{aligned} \quad (\text{B.3})$$

and consequently the rotation matrix, which transforms between BS and SS reads

$$\mathbf{A}(\mathbf{q}) = \begin{pmatrix} q_0^2 + q_1^2 - q_2^2 - q_3^2 & 2(q_1 q_2 + q_0 q_3) & 2(q_1 q_3 - q_0 q_2) \\ 2(q_1 q_2 - q_0 q_3) & q_0^2 - q_1^2 + q_2^2 - q_3^2 & 2(q_2 q_3 + q_0 q_1) \\ 2(q_1 q_3 + q_0 q_2) & 2(q_2 q_3 - q_0 q_1) & q_0^2 - q_1^2 - q_2^2 + q_3^2 \end{pmatrix}. \quad (\text{B.4})$$

Another useful conversion for a rotation quaternion can be achieved when only the rotation axis $\hat{\mathbf{n}}$ ($|\hat{\mathbf{n}}| = 1$) and the rotation angle α is given. Then the corresponding rotation quaternion can be created using

$$\mathbf{q} = \begin{pmatrix} \cos\left(\frac{\alpha}{2}\right) \\ \frac{\mathbf{v}}{v} \sin\left(\frac{\alpha}{2}\right) \end{pmatrix}. \quad (\text{B.5})$$

The linear transformation from the SS to the BS and vice versa by means of the rotation matrix Eq. (B.4) is given by

$$\mathbf{u}^* = \mathbf{A} \cdot \mathbf{u}, \quad (\text{B.6})$$

$$\mathbf{u} = \mathbf{A}^T \cdot \mathbf{u}^*. \quad (\text{B.7})$$

Using the orthogonal matrix

$$\mathbf{Q}(\mathbf{q}) = \begin{pmatrix} q_0 & -q_1 & -q_2 & -q_3 \\ q_1 & q_0 & -q_3 & q_2 \\ q_2 & q_3 & q_0 & -q_1 \\ q_3 & -q_2 & q_1 & q_0 \end{pmatrix} \quad (\text{B.8})$$

we can determine the angular velocity

$$\boldsymbol{\omega}^{(4)*} = 2\mathbf{Q}^T(\mathbf{q})\dot{\mathbf{q}}, \quad (\text{B.9})$$

where $\boldsymbol{\omega}^{(4)*} = (0, \omega_1, \omega_2, \omega_3)^T$ in the BS. Miller et al. [138] have pointed out that a rotation can be described by the extended Hamiltonian

$$\mathcal{H}_{rot}(\mathbf{q}, \boldsymbol{\pi}) = \sum_{k=1}^3 h_k(\mathbf{q}, \boldsymbol{\pi}) + \phi(\mathbf{q}) \quad (\text{B.10})$$

with the rotational kinetic energy

$$E_{rot} = \sum_{k=1}^3 h_k(\mathbf{q}, \boldsymbol{\pi}), \quad (\text{B.11})$$

and

$$h_k(\mathbf{q}, \boldsymbol{\pi}) = \frac{1}{8I_{kk}} (\boldsymbol{\pi}^T \mathbf{D}_k \mathbf{q})^2, \quad (\text{B.12})$$

where

$$\boldsymbol{\pi} = 2\mathbf{Q}(\mathbf{q}) \begin{pmatrix} 0 \\ I_{xx}\omega_1^* \\ I_{yy}\omega_2^* \\ I_{zz}\omega_3^* \end{pmatrix}$$

is the conjugate momentum to \mathbf{q} such that Hamilton's equations are fulfilled

$$\begin{aligned} \dot{\mathbf{q}} &= \nabla_{\boldsymbol{\pi}} \mathcal{H}_{rot}(\mathbf{q}, \boldsymbol{\pi}), \\ \dot{\boldsymbol{\pi}} &= -\nabla_{\mathbf{q}} \mathcal{H}_{rot}(\mathbf{q}, \boldsymbol{\pi}). \end{aligned} \quad (\text{B.13})$$

Here the three symmetry operations $\mathbf{D}_k \mathbf{q}$ are given by

$$\begin{aligned} \mathbf{D}_1 \mathbf{q} &= (-q_1, q_0, q_3, -q_2)^T, \\ \mathbf{D}_2 \mathbf{q} &= (-q_2, -q_3, q_0, q_1)^T, \\ \mathbf{D}_3 \mathbf{q} &= (-q_3, q_2, -q_1, q_0)^T. \end{aligned} \quad (\text{B.14})$$

When propagating a molecule using these Hamiltonian equations of motion, its rigidness is ensured by the identity $q^2 \equiv 1$.

Trotter decomposition

For a system of first order differential equations $\dot{\mathbf{x}}(t) = \mathbf{\Gamma}[\mathbf{x}(t)]$ the formal solution is given by $\mathbf{x}(t) = \exp\{i\mathcal{L}t\}\mathbf{x}(0)$, where $i\mathcal{L} = \mathbf{\Gamma}[\mathbf{x}] \cdot \nabla_x$ is the Liouville operator and \mathbf{x} a phase space vector. The operator $\phi_t = \exp\{i\mathcal{L}t\}$ is called the propagator of the system, which is the exact solution for the time evolution (from time 0 to t) of the system. If the phase space is spanned only by positions and momenta, i.e., $\mathbf{x} = \mathbf{x}(\mathbf{r}, \mathbf{p})$ and the system is Hamiltonian then the Liouvillian is defined as $i\mathcal{L} = \dot{\mathbf{r}} \frac{\partial}{\partial \mathbf{r}} + \dot{\mathbf{p}} \frac{\partial}{\partial \mathbf{p}}$ and the propagator has the form $\phi_t = e^{(A+B)t}$. Since the operators $A = \dot{\mathbf{r}} \frac{\partial}{\partial \mathbf{r}}$ and $B = \dot{\mathbf{p}} \frac{\partial}{\partial \mathbf{p}}$ are usually not commutative, the decomposition of

$$e^{(A+B)t} = e^{At}e^{Bt} + \mathcal{O}(t^2)$$

is correct only up to terms of order t^2 . Hence, for small times t we can create numerical integrators of arbitrary order by using different decomposition schemes. One popular scheme is the Strang decomposition [176], where a given operator

$$e^{i\mathcal{L}\Delta t} = e^{(A_1+\dots+A_p)\Delta t}$$

is symmetrically decomposed to

$$\phi_t = e^{\Delta t/2A_1} \dots e^{\Delta t/2A_{p-1}} e^{\Delta tA_p} e^{\Delta t/2A_{p-1}} \dots e^{\Delta t/2A_1} + \mathcal{O}(\Delta t^3). \quad (\text{B.15})$$

If the interactions of a given system can be divided into long and short range contributions, Tuckerman et al. [148] have shown that the propagator can be decomposed such that a multiple time step scheme can be used. For instance, a Hamiltonian system with the full Liouville operator

$$i\mathcal{L} = \sum_{i=1}^N \left\{ \frac{\mathbf{p}_i}{m} \frac{\partial}{\partial \mathbf{x}_i} + \left(\mathbf{F}_i^{\text{fast}} + \mathbf{F}_i^{\text{slow}} \right) \frac{\partial}{\partial \mathbf{p}_i} \right\} = i\mathcal{L}^{\text{pos}} + i\mathcal{L}^{\text{fast}} + i\mathcal{L}^{\text{slow}}$$

can be decomposed into

$$e^{i\mathcal{L}\Delta t} \approx e^{i\mathcal{L}^{\text{slow}}\Delta t/2} \left[\prod_{i=1}^{n_c} \prod_{j=1}^{n_{ys}} e^{i\mathcal{L}^{\text{fast}}w_j\Delta t/(2n_c)} e^{i\mathcal{L}^{\text{pos}}w_j\Delta t/n_c} e^{i\mathcal{L}^{\text{fast}}w_j\Delta t/(2n_c)} \right] e^{i\mathcal{L}^{\text{slow}}\Delta t/2}, \quad (\text{B.16})$$

where the factors w_j are $\{w_1 = w_3 = 1/(2 - 2^{1/3}), w_2 = 1 - w_1\}$ for $n_{ys} = 3$. Higher order schemes for $n_{ys} = 5, 7, 9, \dots$ can be constructed too. Using this decomposition according to Martyna et al. [76], Miller et al. [138] were able to derive a Verlet-like algorithm for the rotational equations of motion, which is summarized in the next section.

B.2. Dynamics in the NVE ensemble

We denote the full equations of motion for a molecule i as:

$$\begin{aligned} \dot{\mathbf{R}}_i &= \frac{\mathbf{P}_i}{M_i}, \\ \dot{\mathbf{P}}_i &= \mathbf{F}_i, \\ \dot{\mathbf{q}}_i &= \sum_{k=1}^3 \frac{1}{4I_{kk}} (\boldsymbol{\pi}_i^T \mathbf{D}_k \mathbf{q}_i) \mathbf{D}_k \mathbf{q}_i, \\ \dot{\boldsymbol{\pi}}_i &= 2\mathbf{Q}(\mathbf{q}_i) \mathbf{M}_i^{(4)*} - \sum_{k=1}^3 \frac{1}{4I_{kk}} (\boldsymbol{\pi}_i^T \mathbf{D}_k \mathbf{q}_i) \mathbf{D}_k \boldsymbol{\pi}_i. \end{aligned} \quad (\text{B.17})$$

Analogous to $\boldsymbol{\omega}^{(4)}$, $\mathbf{M}_i^{(4)}$ corresponds to the four-dimensional total torque vector in the BS, where the first component equals zero and the remaining components are defined in Eq. (B.2).

Propagator

In the case of the NVE integrator according to Miller et al. [138] the decomposed Liouvillean is given by

$$i\mathcal{L}_{NVE} = i\mathcal{L}_1^{\text{trans}} + i\mathcal{L}_2^{\text{trans}} + i\mathcal{L}^{\text{rot}}, \quad (\text{B.18})$$

with

$$i\mathcal{L}_1^{\text{trans}} = \sum_{i=1}^N \dot{\mathbf{R}}_i \cdot \frac{\partial}{\partial \mathbf{R}_i} = \sum_{i=1}^N \frac{\mathbf{P}_i}{M_i} \cdot \frac{\partial}{\partial \mathbf{R}_i}, \quad (\text{B.19})$$

$$i\mathcal{L}_2^{\text{trans}} = \sum_{i=1}^N \dot{\mathbf{P}}_i \cdot \frac{\partial}{\partial \mathbf{P}_i} = \sum_{i=1}^N \mathbf{F}_i \cdot \frac{\partial}{\partial \mathbf{P}_i}, \quad (\text{B.20})$$

and

$$\begin{aligned} i\mathcal{L}^{\text{rot}} &= \sum_{i=1}^N \left\{ \dot{\mathbf{q}}_i \cdot \frac{\partial}{\partial \dot{\mathbf{q}}_i} + \dot{\boldsymbol{\pi}}_i \cdot \frac{\partial}{\partial \boldsymbol{\pi}_i} \right\} \\ &= \sum_{i=1}^N \left\{ \underbrace{\sum_{k=1}^3 \left[\frac{\partial}{\partial \boldsymbol{\pi}_i} h_k \cdot \frac{\partial}{\partial \mathbf{q}_i} - \frac{\partial}{\partial \mathbf{q}_i} h_k \cdot \frac{\partial}{\partial \boldsymbol{\pi}_i} \right]}_{i\mathcal{L}_k^{\text{rot}}} + \underbrace{2\mathbf{Q}\mathbf{M}_i^{(4)*} \frac{\partial}{\partial \boldsymbol{\pi}_i}}_{i\mathcal{L}_4^{\text{rot}}} \right\}. \end{aligned} \quad (\text{B.21})$$

According to Miller the last operator can be rewritten as (from now on we omit the molecule index i)

$$e^{i\mathcal{L}^{\text{rot}}\Delta t} = \sum_{k=1}^4 i\mathcal{L}_k^{\text{rot}} \approx e^{i\mathcal{L}_4^{\text{rot}}\Delta t/2} \left[\prod_{i=1}^{n_c} \prod_{j=1}^{n_{ys}} E_{\Delta t}^{\text{rot}} \right] e^{i\mathcal{L}_4^{\text{rot}}\Delta t/2}, \quad (\text{B.22})$$

where

$$\begin{aligned} E_{\Delta t}^{\text{rot}} &= e^{i\mathcal{L}_3^{\text{rot}}w_j\Delta t/(2n_c)} e^{i\mathcal{L}_2^{\text{rot}}w_j\Delta t/(2n_c)} e^{i\mathcal{L}_1^{\text{rot}}w_j\Delta t/n_c} \\ &\quad \times e^{i\mathcal{L}_2^{\text{rot}}w_j\Delta t/(2n_c)} e^{i\mathcal{L}_3^{\text{rot}}w_j\Delta t/(2n_c)}. \end{aligned}$$

An exemplary factorization is obtained for $n_{ys} = 3$ with $w_1 = w_3 = 1/(2 - 2^{1/3})$ and $w_2 = 1 - 2w_1$. We summarize the whole decomposed NVE propagator as

$$e^{i\mathcal{L}_{NVE}\Delta t} \approx e^{i\mathcal{L}_2^{\text{trans}}\Delta t/2} e^{i\mathcal{L}_4^{\text{rot}}\Delta t/2} E^{\text{rot}}(\Delta t) e^{i\mathcal{L}_1^{\text{trans}}\Delta t} e^{i\mathcal{L}_4^{\text{rot}}\Delta t/2} e^{i\mathcal{L}_2^{\text{trans}}\Delta t/2}. \quad (\text{B.23})$$

The action of the translational operators gives the well-known velocity Verlet form [40]

$$\begin{aligned} e^{i\mathcal{L}_1^{\text{trans}}\Delta t} \mathbf{R}_i &= \mathbf{R}_i + \Delta t \frac{\mathbf{P}_i}{M_i}, \\ e^{i\mathcal{L}_2^{\text{trans}}\Delta t/2} \mathbf{P}_i &= \mathbf{P}_i + \frac{\Delta t}{2} \mathbf{F}_i, \end{aligned} \quad (\text{B.24})$$

and according to Miller [138] the actions of the rotational operators are given by

$$\begin{aligned} e^{i\mathcal{L}_k^{\text{rot}}\Delta t} \mathbf{q}_i &= \cos(\zeta_k \Delta t) \mathbf{q}_i + \sin(\zeta_k \Delta t) \mathbf{D}_k \mathbf{q}_i \quad (k = 1, 2, 3), \\ e^{i\mathcal{L}_k^{\text{rot}}\Delta t} \boldsymbol{\pi}_i &= \cos(\zeta_k \Delta t) \boldsymbol{\pi}_i + \sin(\zeta_k \Delta t) \mathbf{D}_k \boldsymbol{\pi}_i \quad (k = 1, 2, 3), \\ e^{i\mathcal{L}_4^{\text{rot}}\Delta t/2} \boldsymbol{\pi}_i &= \boldsymbol{\pi}_i + \frac{\Delta t}{2} 2\mathbf{Q}(\mathbf{q}_i) \mathbf{M}^{(4)*}, \end{aligned} \quad (\text{B.25})$$

where

$$\zeta_k = \frac{1}{4I_{kk}} (\boldsymbol{\pi}_i^T \mathbf{D}_k \mathbf{q}_i).$$

We show an implementation of this integrator in a computer program in Algorithm B.1. This integration scheme is both time reversible and symplectic and therefore long term stable and accurate for large time steps.

step 1 propagate position and quaternion a full time step and the conjugate momenta half a timestep (actual time is set to $t = 0$ and index i for molecules is omitted)

1. $\mathbf{V}_{\Delta t/2} = \mathbf{V}_0 + \frac{\Delta t}{2} \frac{\mathbf{F}_0}{m}$
2. $\mathbf{R}_{\Delta t} = \mathbf{R}_0 + \Delta t \mathbf{V}_{\Delta t/2}$
3. $\boldsymbol{\pi}' = \boldsymbol{\pi}_0 + \frac{\Delta t}{2} 2\mathbf{Q}(\mathbf{q}_0) \mathbf{M}_0^{(4)}$ and $\mathbf{q}' = \mathbf{q}_0$
4. using $\xi_k = \frac{1}{4I_{kk}} \boldsymbol{\pi}'^T \mathbf{D}_k \boldsymbol{\pi}'$ calculate

$$\begin{aligned} \boldsymbol{\pi}' &= \cos(\xi_k \delta t) \boldsymbol{\pi}' + \sin(\xi_k \delta t) \mathbf{D}_k \boldsymbol{\pi}' \\ \mathbf{q}' &= \cos(\xi_k \delta t) \mathbf{q}' + \sin(\xi_k \delta t) \mathbf{D}_k \mathbf{q}' \end{aligned}$$

and iterate 5 times with $(k = 3, \delta t = \Delta t/2)$, $(k = 2, \delta t = \Delta t/2)$, $(k = 1, \delta t = \Delta t)$, $(k = 2, \delta t = \Delta t/2)$ and $(k = 3, \delta t = \Delta t/2)$

5. $\boldsymbol{\pi}_{\Delta t/2} = \boldsymbol{\pi}'$ and $\mathbf{q}_{\Delta t} = \mathbf{q}'$

step 2 calculate forces $\mathbf{F}_{\Delta t}$ and torques $\mathbf{M}_{\Delta t}^{(4)}$ using $\mathbf{R}_{\Delta t}$ and the rotation matrix $\mathbf{A}(\mathbf{q}_{\Delta t})$

step 3 propagate conjugate momenta to $t + \Delta t$

1. $\mathbf{V}_{\Delta t} = \mathbf{V}_{\Delta t/2} + \frac{\Delta t}{2} \frac{\mathbf{F}_{\Delta t}}{m}$
2. $\boldsymbol{\pi}_{\Delta t} = \boldsymbol{\pi}_{\Delta t/2} + \frac{\Delta t}{2} 2\mathbf{Q}(\mathbf{q}_{\Delta t}) \mathbf{M}_{\Delta t}^{(4)}$

Algorithm B.1: Simple scheme of a symplectic and time-reversible *NVE* integrator for rigid molecules.

B.3. Dynamics in the NVT ensemble

Instead of *NVE* dynamics, where the Hamiltonian is a conserved quantity, we can also perform dissipative dynamics. Systems subjected to these dynamics are typically defined as systems exchanging energy due to the presence of energy reservoirs, which can be achieved by adding friction terms to the equations of motion. The thermodynamic equivalent to a system coupled to a heat bath is the canonical or *NVT* ensemble.

Nosé and Hoover have developed a thermostat [156, 157] to implement dynamics of this type in computer simulations. Based on this idea, Martyna et al. [76] have proposed a time-reversible integrator for the Nosé–Hoover equations of motion, which has been generalized for rigid molecules by Kamberaj et al. [139]. The latter approach utilizes the following equations of motion:

$$\begin{aligned}
 \dot{\mathbf{R}} &= \frac{\mathbf{P}}{M}, \\
 \dot{\mathbf{P}} &= \mathbf{F}^* - \xi_1^{(t)} \mathbf{P}, \\
 \dot{\mathbf{q}} &= \sum_{k=1}^3 \frac{1}{4I_{kk}} (\boldsymbol{\pi}^T \mathbf{D}_k \mathbf{q}) \mathbf{D}_k \mathbf{q}, \\
 \dot{\boldsymbol{\pi}} &= 2\mathbf{Q}(\mathbf{q})\mathbf{M}^{(4)*} - \sum_{k=1}^3 \frac{1}{4I_{kk}} (\boldsymbol{\pi}^T \mathbf{D}_k \mathbf{q}) \mathbf{D}_k \boldsymbol{\pi} - \xi_1^{(r)} \boldsymbol{\pi}, \\
 \dot{\xi}_1^{(x)} &= G_1^{(x)} / Q_{p_1}^{(x)} - \xi_2^{(x)} \xi_1^{(x)}, \quad \dot{\xi}_2^{(x)} = G_2^{(x)} / Q_{p_2}^{(x)}, \\
 \dot{s}_1^{(x)} &= \xi_1^{(x)} \quad \dot{s}_2^{(x)} = \xi_2^{(x)} \quad \text{with } x = t, r.
 \end{aligned} \tag{B.26}$$

Note, that the extended equations of motion for rigid bodies given here employ a chain of two thermostats. Here, $\xi_1^{(t)}$ and $\xi_1^{(r)}$ play the role of velocities of thermostat 1 coupled to the (t) translational, or (r) rotational degrees of freedom, respectively. $G_x^{(t,r)}$ are the thermostat 'forces', given by

$$\begin{aligned}
 G_1^{(t)} &= 2E_{\text{trans}} - g_f^{(t)} k_B T_0, & G_1^{(r)} &= 2E_{\text{rot}} - g_f^{(r)} k_B T_0, \\
 G_2^{(t)} &= Q_{p_1}^{(t)} (\xi_1^{(t)})^2 - k_B T_0, & G_2^{(r)} &= Q_{p_1}^{(r)} (\xi_1^{(r)})^2 - k_B T_0,
 \end{aligned} \tag{B.27}$$

where E_{trans} and E_{rot} (see Eq. (B.11)) are the translational kinetic energy and the rotational kinetic energy, respectively. Furthermore $g_f^{(t)}$ and $g_f^{(r)}$ are the number of translational and rotational degrees of freedom, k_B the Boltzmann's constant, T_0 is the desired temperature and $Q_{p_x}^{(t)}$ and $Q_{p_x}^{(r)}$ the thermostat 'masses'. The thermostat

'positions' $s_{1,2}^{(t)}$ and $s_{1,2}^{(r)}$ occur only at the left hand side of the equations of motion in Eq. (B.26) and could be neglected. However, since they are required for determining the degree to which the extended Hamiltonian is conserved as well as the phase space compressibility, they are usually also integrated. This extended pseudo Hamiltonian is given by

$$\mathcal{H}_{\text{NVT}} = \mathcal{H}_{\text{NVE}} + k_B T_0 \ln J_{\text{NVT}} + \frac{1}{2} \sum_{k=1}^2 \sum_{x=t,r} Q_{p_k}^{(x)} (\xi_k^{(x)})^2, \quad (\text{B.28})$$

where J is the system's Jacobian, given by

$$J_{\text{NVT}} = \exp \left[g_f^{(t)} s_1^{(t)} + g_f^{(r)} s_1^{(r)} + s_2^{(t)} + s_2^{(r)} \right]. \quad (\text{B.29})$$

The number of degrees of freedom for a system of N rigid molecules is $g_f^{(t)} = g_f^{(r)} = dN$, where d is the system's dimension. While physically more or less meaningless, the quantity \mathcal{H}_{NVT} is conserved during the simulation and can be used to check the implementation, as well as the choice of the time step.

The thermostat 'masses' are related to the the thermostat fluctuations by

$$Q_{p_1}^{(t,r)} = g_f^{(t,r)} k_B T_0 / \nu^2, \quad Q_{p_2}^{(t,r)} = k_B T_0 / \nu^2, \quad (\text{B.30})$$

where ν is the frequency of the system's temperature fluctuations.

Propagator

The corresponding Liouville operator is

$$i\mathcal{L}_{\text{NVT}} = i\mathcal{L}_{\text{NVE}} + i \sum_{x=t,r} \mathcal{L}_{\text{NHC}}^{(x)}, \quad (\text{B.31})$$

where \mathcal{L}_{NVE} is given in Eq. (B.18) and \mathcal{L}_{NHC} emerges due to the Nosé - Hoover chain extensions to the equations of motion

$$i\mathcal{L}_{\text{NHC}}^{(x)} = i\mathcal{L}_{\text{NHC},1}^{(x)} + i\mathcal{L}_{\text{NHC},2}^{(x)} + i\mathcal{L}_{\text{NHC},3}^{(x)} + \mathcal{L}_{\text{NHC},4}^{(x)}, \quad (\text{B.32})$$

with

$$\begin{aligned} i\mathcal{L}_{\text{NHC},1}^{(t)} &= \sum_{j=1}^N \left[-\xi_1^{(t)} \mathbf{V}_j \right] \cdot \frac{\partial}{\partial \mathbf{V}_j}, & i\mathcal{L}_{\text{NHC},1}^{(r)} &= \sum_{j=1}^N \left[-\xi_1^{(r)} \boldsymbol{\pi}_j \right] \cdot \frac{\partial}{\partial \boldsymbol{\pi}_j}, \\ i\mathcal{L}_{\text{NHC},2}^{(x)} &= \left[\frac{G_1^{(x)}}{Q_{p_1}} - \xi_2^{(x)} \xi_1^{(x)} \right] \frac{\partial}{\partial \xi_1^{(x)}}, & i\mathcal{L}_{\text{NHC},3}^{(x)} &= \frac{G_2^{(x)}}{Q_{p_2}} \frac{\partial}{\partial \xi_2^{(x)}}, \\ i\mathcal{L}_{\text{NHC},4}^{(x)} &= \sum_{k=1}^2 \xi_k^{(x)} \frac{\partial}{\partial s_k^{(x)}}. \end{aligned} \quad (\text{B.33})$$

step 1 update thermostat variables for half a timestep $t \rightarrow t + \Delta t/2$; repeat all steps for $x = t$ and $x = r$, respectively

1. calculate $G_1^{(x)}/Q_1^{(x)}$ and $G_2^{(x)}/Q_2^{(x)}$
2. $\xi_2^{(x)} \rightarrow \xi_2^{(x)} + \frac{\Delta t}{4} G_2^{(x)}/Q_2^{(x)}$
3. $\xi_1^{(x)} \rightarrow \left[\xi_1^{(x)} e^{-\xi_2^{(x)} \Delta t/8} + \frac{\Delta t}{4} G_1^{(x)}/Q_1^{(x)} \frac{\sinh(\xi_1^{(x)} \Delta t/8)}{\xi_1^{(x)} \Delta t/8} \right] e^{-\Delta t/8 \xi_2^{(x)}}$
4. update velocities:
 for x=t do $\mathbf{V}_j \rightarrow \mathbf{V}_j \exp(-\xi_1^{(t)} \Delta t/2)$ and
 for x=b do $\boldsymbol{\pi}_j \rightarrow \boldsymbol{\pi}_j \exp(-\xi_1^{(r)} \Delta t/2)$ for each molecules j
5. $s_k^{(x)} \rightarrow s_k^{(x)} + \xi_k^{(x)} \Delta t/2$ for $k = 1, 2$
6. do substep 3 again
7. do substep 2 again

step 2 apply the *NVE* algorithm (Algorithm B.2)

step 3 do step 1 again

Algorithm B.2: Simple scheme of a time-reversible NVT integrator for rigid molecules.

Using the Strang splitting we can denote the full propagator for one time step $\phi_t = \exp(i\Delta t \mathcal{L}_{\text{NVT}})$ according Tuckerman et al. [77, 177] as

$$\phi_t = e^{i\Delta t/2 \mathcal{L}_{\text{NHC}}} e^{i\Delta t \mathcal{L}_{\text{NVE}}} e^{i\Delta t/2 \mathcal{L}_{\text{NHC}}} \quad (\text{B.34})$$

where the Nosé-Hoover chain variables are propagated by the following decomposed operator

$$\begin{aligned} e^{i\Delta t/2 \mathcal{L}_{\text{NHC}}} &= e^{i\Delta t/4 \mathcal{L}_{\text{NHC},3}^{(r)}} e^{i\Delta t/4 \mathcal{L}_{\text{NHC},3}^{(t)}} e^{i\Delta t/4 \mathcal{L}_{\text{NHC},2}^{(r)}} e^{i\Delta t/4 \mathcal{L}_{\text{NHC},2}^{(t)}} \\ &\times e^{i\Delta t/2 \mathcal{L}_{\text{NHC},1}^{(r)}} e^{i\Delta t/2 \mathcal{L}_{\text{NHC},1}^{(t)}} e^{i\Delta t/2 \mathcal{L}_{\text{NHC},4}^{(r)}} e^{i\Delta t/2 \mathcal{L}_{\text{NHC},4}^{(t)}} \\ &\times e^{i\Delta t/4 \mathcal{L}_{\text{NHC},2}^{(t)}} e^{i\Delta t/4 \mathcal{L}_{\text{NHC},2}^{(r)}} e^{i\Delta t/4 \mathcal{L}_{\text{NHC},3}^{(t)}} e^{i\Delta t/4 \mathcal{L}_{\text{NHC},3}^{(r)}} . \end{aligned} \quad (\text{B.35})$$

In Eq. (B.33) three different types of operators occur, where their action is given by

$$\begin{aligned}
 \exp \left\{ i a x \frac{\partial}{\partial x} \right\} x &= x + a, \\
 \exp \left\{ i a \mathbf{x} \cdot \frac{\partial}{\partial \mathbf{x}} \right\} \mathbf{x} &= e^{a \mathbf{x}}, \\
 \exp \left\{ i a (b - cx) \frac{\partial}{\partial x} \right\} x &= x e^{-ac} + a b e^{-\frac{a}{2}c} \left[\frac{\sinh(\frac{a}{2}c)}{\frac{a}{2}c} \right]. \quad (\text{B.36})
 \end{aligned}$$

Since the action of the last operator Eq. (B.36) requires the evaluation of the singular function, one can either use the Taylor expansion of $\sinh(x)/x$ or use the further factorization

$$\exp \left\{ i a (b - cx) \frac{\partial}{\partial x} \right\} x \approx \exp \left(-\frac{a}{2} c x \frac{\partial}{\partial x} \right) \exp \left(a b x \frac{\partial}{\partial x} \right) \exp \left(-\frac{a}{2} c x \frac{\partial}{\partial x} \right). \quad (\text{B.37})$$

Using the last results we can derive a scheme for the NVT -integrator given in Algorithm B.2.

B.4. Dynamics in the NPT ensemble

For isotropic cell fluctuations only the equations of motion for rigid molecules are given as

$$\begin{aligned}
 \dot{\mathbf{R}} &= \frac{\mathbf{P}}{M} + \xi_\epsilon \mathbf{R} \\
 \dot{\mathbf{P}} &= \mathbf{F} - \xi_1^{(t)} \mathbf{P} - \left(1 + \frac{d}{g_f} \right) \xi_\epsilon \mathbf{P} \\
 \dot{\mathbf{q}} &= \sum_{k=1}^3 \frac{1}{4I_{kk}} (\boldsymbol{\pi}^T \mathbf{D}_k \mathbf{q}) \mathbf{D}_k \mathbf{q} \\
 \dot{\boldsymbol{\pi}} &= 2\mathbf{Q}(\mathbf{q})\mathbf{M}^{(4)*} - \sum_{k=1}^3 \frac{1}{4I_{kk}} (\boldsymbol{\pi}^T \mathbf{D}_k \mathbf{q}) \mathbf{D}_k \boldsymbol{\pi} - \xi_1^{(r)} \boldsymbol{\pi} - \frac{d}{g_f} \xi_\epsilon \boldsymbol{\pi} \\
 \dot{\epsilon} &= \xi_\epsilon \\
 \dot{\xi}_\epsilon &= G_\epsilon / W - \xi_1^{(b)} \xi_\epsilon \\
 \dot{\xi}_1^{(x)} &= G_1^{(x)} / Q_{p_1}^{(x)} - \xi_2^{(x)} \xi_1^{(x)}, \quad \dot{\xi}_2^{(x)} = G_2^{(x)} / Q_{p_2}^{(x)} \\
 \dot{s}_1^{(x)} &= \xi_1^{(x)}, \quad \dot{s}_2^{(x)} = \xi_2^{(x)} \quad \text{with } x = t, r, b. \quad (\text{B.38})
 \end{aligned}$$

Here, a barostat is coupled to the center of mass positions and momenta, as well as to the quaternion momenta via ξ_ϵ . Its 'position' is related to the volume of the simulation box according to $\epsilon = \ln(V)/3$. Furthermore, a chain of thermostats $\xi_1^{(b)}$

and $\xi_2^{(b)}$ is coupled to the pressure bath. The total number of degrees of freedom is $g_f = g_f^{(t)} + g_f^{(r)} = 6N$. The barostat 'force' is given by

$$G_\epsilon = dV (P_{\text{int}} - P_0) + \frac{2d}{g_f} (E_{\text{trans}} + E_{\text{rot}}), \quad (\text{B.39})$$

where the internal pressure P_{int} is given below in Eq. (B.49) and E_{trans} and E_{rot} are translational and rotational kinetic energy, respectively. The thermostat 'forces' acting on the pressure bath are

$$G_1^{(b)} = W \xi_\epsilon^2 - k_B T_0, \quad G_2^{(b)} = Q_{p_1}^{(b)} (\xi_1^{(b)})^2 - k_B T_0. \quad (\text{B.40})$$

The barostat and thermostat related 'masses' are given by

$$\begin{aligned} Q_{p_1}^{(b)} &= d^2 k_B T_0 / \nu_b^2, & Q_{p_2}^{(b)} &= k_B T_0 / \nu_b^2, \\ W &= (g_f + d) k_B T_0 / \nu_b^2, \end{aligned} \quad (\text{B.41})$$

where ν_b is the frequency of the volume fluctuations of the system.

The conserved quantity for systems propagating the equations of motion as given in Eq. (B.38) is

$$\mathcal{H}_{\text{NPT}} = \mathcal{H}_{\text{NVE}} + P_0 V + k_B T_0 \ln J_{\text{NPT}} + \frac{1}{2} \sum_{x=t,r,b} \sum_{k=1}^2 Q_{p_k}^{(x)} (\xi_k^{(x)})^2 + \frac{W}{2} \xi_\epsilon^2, \quad (\text{B.42})$$

with the Jacobian

$$J_{\text{NPT}} = J_{\text{NVT}} \times \exp \left[s_1^{(b)} + s_2^{(b)} \right]. \quad (\text{B.43})$$

According to Andersen [158] a good choice of the barostat coupling is $\nu_b^{-1} = \sqrt[3]{V}/c$, where V is the volume of the simulation box and c is the speed of sound in the system.

Propagator

For the isothermal-isobaric ensemble the Liouville operator can be written as

$$i\mathcal{L}_{\text{NPT}} = i\mathcal{L}_1^{\text{trans}} + i\mathcal{L}_2^{\text{trans}} + i\mathcal{L}^{\text{rot}} + i\mathcal{L}_1^{\text{baro}} + i\mathcal{L}_2^{\text{baro}} + i \sum_{x=t,r,b} \mathcal{L}_{\text{NHC}}^{(x)},$$

where the particular operators are given by

$$\begin{aligned}
 i\mathcal{L}_1^{\text{trans}} &= \sum_{j=1}^N \left[\frac{\mathbf{P}_j}{M} + \xi_\epsilon \mathbf{R}_j \right] \cdot \frac{\partial}{\partial \mathbf{R}_j}, & i\mathcal{L}_2^{\text{trans}} &= \sum_{j=1}^N \left[\mathbf{F}_j - \left(1 + \frac{d}{g_f} \right) \xi_\epsilon \mathbf{P} \right] \cdot \frac{\partial}{\partial \mathbf{P}_j} \\
 i\mathcal{L}_{\text{NHC},1}^{(b)} &= -\xi_1^{(b)} \xi_\epsilon \frac{\partial}{\partial \xi_\epsilon}, & i\mathcal{L}_4^{\text{rot}} &= \sum_{j=1}^N \left[2\mathbf{QM}_i^{(4)*} - \frac{d}{g_f} \xi_\epsilon \boldsymbol{\pi}_j \right] \cdot \frac{\partial}{\partial \boldsymbol{\pi}_j} \\
 i\mathcal{L}_1^{\text{baro}} &= \xi_\epsilon \frac{\partial}{\partial \epsilon}, & i\mathcal{L}_2^{\text{baro}} &= \frac{G_\epsilon}{W} \frac{\partial}{\partial \xi_\epsilon}.
 \end{aligned} \tag{B.44}$$

The Liouville operators $i\mathcal{L}^{\text{rot}1,2,3}$ and $i\mathcal{L}_{\text{NHC},2,3,4}$ remain unchanged and are defined in Eqs. (B.19)–(B.21) and (B.33), respectively. Similar to the NVT propagator we use the following decomposed isotropic NPT propagator:

$$\begin{aligned}
 \phi_t &= e^{i\Delta t/2\mathcal{L}_{\text{NHC}}^{(b)}} e^{i\Delta t/2\mathcal{L}_{\text{NHC}}^{(t)}} e^{i\Delta t/2\mathcal{L}_{\text{NHC}}^{(r)}} e^{i\Delta t/2\mathcal{L}_2^{\text{baro}}} e^{i\Delta t/2\mathcal{L}_2^{\text{trans}}} \\
 &\times e^{i\Delta t/2\mathcal{L}_4^{\text{rot}}} e^{i\Delta t\mathcal{L}_1^{(\text{baro})}} e^{i\Delta t\mathcal{L}_1^{\text{trans}}} E^{\text{rot}}(\Delta t) e^{i\Delta t/2\mathcal{L}_4^{\text{rot}}} \\
 &\times e^{i\Delta t/2\mathcal{L}_2^{\text{trans}}} e^{i\Delta t/2\mathcal{L}_2^{\text{baro}}} e^{i\Delta t/2\mathcal{L}_{\text{NHC}}^{(r)}} e^{i\Delta t/2\mathcal{L}_{\text{NHC}}^{(t)}} e^{i\Delta t/2\mathcal{L}_{\text{NHC}}^{(b)}}.
 \end{aligned} \tag{B.45}$$

Here, a new type of operator occurs in addition to the operators of Eq. (B.36), namely

$$\exp \left\{ i a (\mathbf{b} + c \mathbf{x}) \cdot \frac{\partial}{\partial \mathbf{x}} \right\} \mathbf{x} = \mathbf{x} e^{ac} + \mathbf{b} a e^{\frac{a}{2}c} \left[\frac{\sinh \left(\frac{a}{2}c \right)}{\frac{a}{2}c} \right]. \tag{B.46}$$

Using this propagator we summarize the whole NPT integrator in Algorithm B.3.

Internal pressure

For a system of N particles the instantaneous internal pressure is given by the virial

$$P_{\text{int}} = \frac{1}{3V} \left(2E_{\text{kin}} + \sum_{i=1}^N \mathbf{r}_i \cdot \mathbf{F}_i \right), \tag{B.47}$$

where \mathbf{r}_i is the position of particle i and \mathbf{F}_i is the force acting on it. Unfortunately, this definition only holds for non-periodic systems. Extending the virial to systems with periodic boundary conditions (PBC) in the case of pair potentials, the virial can be rewritten to

$$P_{\text{int}} = \frac{1}{3V} \left(2E_{\text{kin}} + \sum_{i=1}^{N-1} \sum_{j=i+1}^N \mathbf{r}_{ij} \cdot \mathbf{f}_{ij} \right), \tag{B.48}$$

- step 1** apply step 1 of the NVT algorithm (Algorithm B.2) for the thermostat variables $x = t$, $x = r$ as well as $x = b$. For the thermostat variables coupled to the box ($x = b$) add the modification of sub step 4: $\xi_\epsilon \rightarrow \xi_\epsilon \exp(-\xi_1^{(b)} \Delta t/2)$
- step 2** calculate pressure bath 'force' and update 'velocity'
1. calculate G_ϵ according Eq. (B.39)
 2. $\xi_\epsilon \rightarrow \xi_\epsilon e^{-\xi_1^{(b)} \Delta t/2}$
- step 3** update center of mass velocities and quaternion 'velocities' to $t + \frac{\Delta t}{2}$
1. $\mathbf{V} \rightarrow \mathbf{V} e^{-[1+d/g_f]\xi_\epsilon \Delta t/2} + \frac{\Delta t}{2M} \mathbf{F} e^{-[1+d/g_f]\xi_\epsilon \Delta t/4} \frac{\sinh(\xi_\epsilon \Delta t/4)}{\xi_\epsilon \Delta t/4}$
 2. $\boldsymbol{\pi} \rightarrow \boldsymbol{\pi} e^{-\frac{d}{g_f} \xi_\epsilon \Delta t/2} + \frac{\Delta t}{2} 2\mathbf{QM}_i^{(4)*} e^{-\frac{d}{g_f} \xi_\epsilon \Delta t/4} \frac{\sinh(\xi_\epsilon \Delta t/4)}{\xi_\epsilon \Delta t/4}$
- step 4** rotate molecules for a full timestep according step 4 and 5 of the NVE algorithm (Algorithm B.1)
- step 5** update center of mass positions $\mathbf{R} \rightarrow \mathbf{R} e^{\Delta t \xi_\epsilon} + \Delta t \mathbf{V} e^{\xi_\epsilon \Delta t/2} \frac{\sinh(\xi_\epsilon \Delta t/2)}{\xi_\epsilon \Delta t/2}$
- step 6** Update box $\epsilon \rightarrow \epsilon + \Delta t \xi_\epsilon$, recalculate box dependent quantities like tail corrections, k-vector for *Ewald summation*,...
- step 7** calculate forces, pressure and torques
- step 8** do step 3 again
- step 9** do step 2 again
- step 10** do step 1 again

Algorithm B.3: Simple scheme of a time-reversible isotropic NPT integrator for rigid molecules.

where \mathbf{r}_{ij} is the distance vector between particle i and j and \mathbf{f}_{ij} the force on atom i due to atom j , respectively. In the case of systems with non-pair potential and periodic boundary conditions the correct virial is given by

$$P_{\text{int}} = \frac{1}{3V} \left(2E_{\text{kin}} + \sum_{i=1}^N \mathbf{r}_i \cdot \mathbf{F}_i \right) - \frac{\partial U}{\partial V}. \quad (\text{B.49})$$

For a full derivation see [178].

For a molecular system with short range and electrostatic interactions, like TIP4P water, in a periodically replicated box the internal pressure is given by

$$P_{\text{int}} = \frac{1}{3V} \left(E_{\text{trans}} + E_{\text{rot}} + \sum_{i=1}^{N_s-1} \sum_{j=i+1}^{N_s} \mathbf{r}_{ij} \cdot \mathbf{f}_{ij}^s \right) + \frac{1}{3} \text{Tr} \left(\mathbf{P}^{\text{Ewald}} \right) - \frac{\partial U}{\partial V}. \quad (\text{B.50})$$

where N_s is the number of interaction sites affected by short-ranged pair-additive forces f^s , $\text{Tr} \left(\mathbf{P}^{\text{Ewald}} \right)$ is the trace of the pressure tensor of the Coulomb interactions given in Eq. (5.12) and $\partial U / \partial V$ is the contribution due to other additional non-pair interactions, as for instance Lennard-Jones tail corrections.

Alternatively, the average pressure $\langle P_{\text{int}} \rangle$ can be measured more accurately (at least for small systems) following Ref. [165].

Lennard-Jones tail corrections for systems with fluctuating cells

Due to the usage of finite simulation boxes in computer programs, periodic boundary conditions are used in order to simulate bulk materials. Hence, interaction partners are usually selected using the *nearest image convention* [40, 162].

When a potential is truncated then the contribution of particles beyond this cutoff are obviously neglected. This introduces an error which can be estimated using so-called tail corrections. If the potential energy is written as sum over all interaction pairs then the corrected energy of the system is given by

$$U_{\text{corr}} = \sum_{j>i} u(r_{ij}) + U^{\text{tail}}(r_{\text{cut}}). \quad (\text{B.51})$$

As denoted in Eq. (5.1) this energy tail correction can be estimated by the integral over the pair potential

$$U^{\text{tail}} = N2\pi\rho \int_{r_{\text{cut}}}^{\infty} dr u(r)r^2, \quad (\text{B.52})$$

where N is the number of particles, $\varrho = N/V$ the density, r_{cut} the cutoff and $u(r)$ the pair potential function. In particular, for Lennard-Jones interactions the tail correction is given by

$$U_{\text{LJ}}^{\text{tail}} = 8\pi N \varrho \varepsilon \int_{r_{\text{cut}}}^{\infty} dr \left[\frac{\sigma^{12}}{r^{10}} - \frac{\sigma^6}{r^4} \right] = \frac{8}{3} N \pi \varrho \varepsilon \sigma^3 \left(\frac{1}{3} \frac{\sigma^9}{r_{\text{cut}}^9} - \frac{\sigma^3}{r_{\text{cut}}^3} \right). \quad (\text{B.53})$$

The estimation given in Eq. (B.52) is only valid for a truncated potential and it is assumed that beyond the cutoff the density is homogenous. Since this truncation introduces a discontinuity in the potential function, one can avoid this singularity by shifting the potential such that $u_{\text{shifted}}(r) = u(r) - u(r_{\text{cut}})$. This shift necessitates a modification of the tail corrections in the following manner

$$U_{\text{shifted}}^{\text{tail}} = U^{\text{tail}}(r_{\text{cut}}) + N u_a(r_{\text{cut}}), \quad (\text{B.54})$$

where $u_a(r_{\text{cut}})$ depends on the average number of particle in the vicinity of an arbitrary particle, namely

$$u_a(r_{\text{cut}}) = N_c(r_{\text{cut}}) \frac{u(r_{\text{cut}})}{2}, \quad (\text{B.55})$$

where the average number of interaction partners N_c can be estimated by

$$N_c(r_{\text{cut}}) = \varrho V_{\text{cut}} - 1 \approx \varrho V_{\text{cut}}, \quad (\text{B.56})$$

and V_{cut} is the volume of sphere with radius r_{cut} .

For truncated and shifted Lennard-Jones interactions, the tail correction (Equation (B.54)) becomes

$$\begin{aligned} U_{\text{shifted LJ}}^{\text{tail}} &= \frac{8}{3} N \pi \varrho \varepsilon \sigma^3 \left(\frac{1}{3} \frac{\sigma^9}{r_{\text{cut}}^9} - \frac{\sigma^3}{r_{\text{cut}}^3} \right) + N \frac{8}{3} \pi r_{\text{cut}}^3 \varrho \varepsilon \left(\frac{\sigma^{12}}{r_{\text{cut}}^{12}} - \frac{\sigma^6}{r_{\text{cut}}^6} \right) \\ &= \frac{16\pi}{3} N \varrho \sigma^3 \varepsilon \left(\frac{2}{3} \frac{\sigma^9}{r_{\text{cut}}^9} - \frac{\sigma^3}{r_{\text{cut}}^3} \right). \end{aligned} \quad (\text{B.57})$$

While in constant energy or constant temperature simulations these tail corrections do not influence the dynamics of the system, in isobaric simulations (NPH, NPT, ...) the instantaneous pressure appears in the equations of motion and must therefore be computed accurately. This becomes obvious when we consider the definition of the instantaneous pressure Eq. (B.50). Since the potential energy tail correction depends on the volume of the system the derivative $\partial U^{\text{tail}}/\partial V$ is non-zero

and has to be added to the internal pressure. Depending on the way the cutoff is implemented two different cases exist, which must be considered separately. First, if a constant cutoff is chosen in cell fluctuating simulations (rather than the ratio of the box length) then

$$\frac{\partial}{\partial V} U_{\text{LJ}}^{\text{tail}} = \frac{\partial}{\partial V} U_{\text{shifted LJ}}^{\text{tail}} = -\frac{16}{3} \pi \rho^2 \sigma^3 \epsilon \left(\frac{2}{3} \frac{\sigma^9}{r_{\text{cut}}^9} - \frac{\sigma^3}{r_{\text{cut}}^3} \right) =: -P_{\text{LJ}}^{\text{tail}}. \quad (\text{B.58})$$

This result is usually called the pressure tail correction for Lennard-Jones interactions. Note, due to the definition of the internal pressure Eq. (B.50) the negative sign disappears and the tail correction is simply added to the pressure.

When using a cutoff equal to half of box length $r_{\text{cut}} = L_{\text{Box}}/2$ then the derivation of the potential with respect to the volume differs due to $r_{\text{cut}} = r_{\text{cut}}(V)$ and the alterable potential shift, i.e., at every time step the potential is shifted according to r_{cut} . If we rewrite Eq. (B.51) to

$$U_{\text{corr}} = \frac{1}{2} \sum_i \sum_{j \neq i} [u(r_{ij}) - u(r_{\text{cut}})] + U^{\text{tail}}(r_{\text{cut}}), \quad (\text{B.59})$$

and use the approximation

$$U^{\text{shift}} = -\frac{1}{2} \sum_i \sum_{j \neq i} u(r_{\text{cut}}) \approx -\frac{NN_c}{2} u(r_{\text{cut}}), \quad (\text{B.60})$$

as well as

$$\frac{\partial U}{\partial V} = \frac{\partial r_{\text{cut}}}{\partial V} \frac{\partial U}{\partial r_{\text{cut}}} = \frac{1}{24r_{\text{cut}}^2} \frac{\partial U}{\partial r_{\text{cut}}} \quad (\text{B.61})$$

and estimate the average particle number within the cutoff as given in equation (B.56) we can denote

$$\frac{\partial}{\partial V} U_{\text{LJ}}^{\text{shift}} = \frac{\pi N^2 \epsilon}{6r_{\text{cut}}^3} \left(\frac{4}{3} \frac{\sigma^{12}}{r_{\text{cut}}^{12}} - \frac{\sigma^6}{r_{\text{cut}}^6} \right), \quad (\text{B.62})$$

and

$$\frac{\partial}{\partial V} U_{\text{LJ}}^{\text{tail}} = -\frac{\pi N^2 \epsilon}{12r_{\text{cut}}^3} \left(2 \frac{\sigma^{12}}{r_{\text{cut}}^{12}} - \frac{\sigma^6}{r_{\text{cut}}^6} \right). \quad (\text{B.63})$$

Summing up the last two equations gives the final result

$$\frac{\partial}{\partial V} \left(U_{\text{LJ}}^{\text{shift}} + U_{\text{LJ}}^{\text{tail}} \right) = -\frac{16\pi}{3} \rho^2 \sigma^3 \epsilon \left(\frac{2}{3} \frac{\sigma^9}{r_{\text{cut}}^9} - \frac{\sigma^3}{r_{\text{cut}}^3} \right) =: -P_{\text{LJ}}^{\text{tail}}. \quad (\text{B.64})$$

This shows that every possible implementation of the cutoff leads to $P_{\text{LJ}}^{\text{tail}}$ as the additional term in the internal pressure Eq. (B.50).

Distributions of thermostat and barostat state variables

In order to decrease the time a simulation needs to equilibrate initially, all state variables should be randomly chosen from the appropriate equilibrium distribution. Sometimes it can also be necessary to sample state variables at random, for instance in the HMC scheme (see Sec. 5.3). Another possible application is the use of checkpoints which were previously generated in a certain ensemble as starting states for the propagation in a different ensemble. Let's imagine we want to analyze properties of critical nuclei of a certain system. A convenient way to generate such configurations is the use of biased Monte Carlo simulations (umbrella sampling). Unfortunately, the study of time dependent quantities requires time propagation via real dynamics as provided by molecular dynamics simulations. Since only positions are available from Monte Carlo simulations, all other state variables have to be drawn from their equilibrium distributions in order to set up an equilibrated MD simulation.

The thermostat as well as the barostat enter the equations of motion (Eqs. (B.26) and (B.26)) as velocities providing additional kinetic energy-like terms to the extended Hamiltonian (Eqs. (B.28) and (B.42)). Thus the corresponding distributions are Gaussian with zero mean and the standard deviation

$$\sigma = \sqrt{\frac{k_B T}{m}}, \quad (\text{B.65})$$

where the mass m corresponds to one of the thermostat or barostat 'masses'. In particular, these are $Q_{p_1}^{(x)}, Q_{p_2}^{(x)}$ for $x = t, r, b$ and W .

Numerical results for the equilibrium distributions of the state variables of the thermostat and barostat are shown in Fig. B.1.

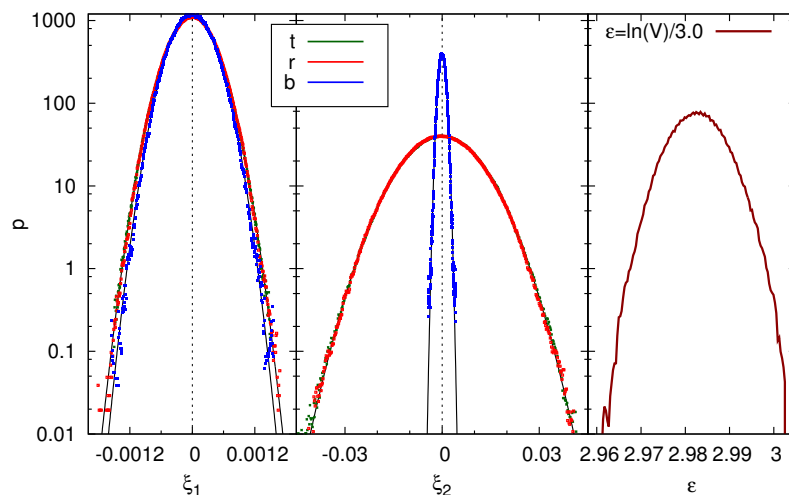


Figure B.1.: Probability distributions of the thermostat and barostat extended state variables. Left: distributions $p(\xi_1^{(t)})$, $p(\xi_1^{(r)})$ and $p(\xi_1^{(b)})$. Center: distributions $p(\xi_2^{(t)})$, $p(\xi_2^{(r)})$ and $p(\xi_2^{(b)})$. Right: probability distribution $p(\epsilon)$. The black solid lines are the analytically determined Gaussians, while all dots are simulation results. The simulation parameters are: system size $N = 256$, temperature $T = 300$ K, pressure $P = 0$ bar, trajectory length $\tau = 10$ ns and time step $\Delta t = 1$ fs. (All values in the plots are in reduced units, see Sec. 5.3).

Index

- Artificial neural networks, *see* Neural network
- Bond angle distribution method, 31
- Centrosymmetry deviation method, 31
- Common neighbor analysis method, 31
- Coulombic interactions
 - Ewald summation, 102 – 108, 116
 - Lekner summation, 102
 - reaction field method, 102
- Dimer, 23
- Dynamical system, 7
- Euler angles, 119
- Ewald summation, 64
- Feed-forward neural network, 2
- Fermi-Pasta-Ulam chain, 6
- Forest-Ruth integrator, 18
- FPU problem, *see* Fermi-Pasta-Ulam chain
- Free energy calculation
 - metadynamics, 30
 - Umbrella sampling, 30, 91, 101
- Free energy calculations
 - Umbrella sampling, 135
- Hybrid Monte Carlo (HMC), 91, 101, 117, 135
- Ice
 - Bernal Fowler rules, 58, 100
 - ice rules, *see* Bernal Fowler rules
 - proton order, 58, 100
- Integrator
 - for the *NPT* ensemble, 130
 - for the *NVE* ensemble, 124
 - for the *NVT* ensemble, 128
- Internal pressure, 129 – 132
- IR absorption spectrum
 - calculation, 62
 - of cubic ice phases, 70
 - of hexagonal ice phases, 70
- Jacobi matrix, 113
- Kalman filter, 41f
 - multistreaming, 42
- Lennard Jones
 - angular distribution function, 45
 - isotherms, 43

- radial distribution function, 45
- Lorentz gas, 17
- Lyapunov exponent, 8
 - finite time, 8
- Lyapunov weighted path ensemble (LWPE), 11

- Martyna Tuckerman Klein algorithm
 - distribution of state variables, 134f
 - equations of motion, 128

- Neural network, 33, 39
 - over-fitting, 49
 - sensitivity analysis, 39, 94
 - training, 40f
- Neural network structure detection
 - method, 2, 33, 89

- Order parameter criteria, 30

- Propagator, 7, 121

- Quaternions, 119ff

- Rare event, 1
- Reactive trajectory, 1
- Relative Lyapunov Indicator (RLI), 9
- Root mean square error (RMSE), 41
- root mean square error (RMSE), 46

- Saddle point, 1, 26
- Self-consistent histogram method, 91, 101
- Steinhardt bond order parameters, 31, 49ff, 84f
- Symmetry functions, 35 – 40

- Tail corrections, 132ff
- Transition interface sampling, 117
- Transition path sampling, 11, 30, 117
- Trotter decomposition, 121

- Units, 102

- Virial, 130

- Water model properties
 - SPC/E, 108
 - TIP4P, 108
 - TIP4P/Ice, 61, 99, 108

Bibliography

- [1] E. OTT, *Chaos in dynamical systems*, Cambridge University Press, 1993.
- [2] N. MURRAY and M. HOLMAN, The origin of chaos in the outer solar system, *Science* **283**, 1877 (1999).
- [3] T. KOMATSUZAKI and R. S. BERRY, Chemical Reaction Dynamics: Many-Body Chaos and Regularity, *Adv. Chem. Phys.* **123**, 79 (2002).
- [4] G. S. EZRA, H. WAALKENS, and S. WIGGINS, Microcanonical rates, gap times, and phase space dividing surfaces, *J. Chem. Phys.* **130**, 164118 (2009).
- [5] J. TAILLEUR and J. KURCHAN, Probing rare physical trajectories with Lyapunov weighted dynamics, *Nature Phys.* **3**, 203 (2007).
- [6] C. DELLAGO, P. BOLHUIS, F. CSAJKA, and D. CHANDLER, Transition Path Sampling and the Calculation of Rate Constants, *J. Chem. Phys.* **108**, 1964 (1998).
- [7] P. G. BOLHUIS, C. DELLAGO, P. L. GEISLER, and D. CHANDLER, Transition path sampling: throwing ropes over mountains in the dark, *J. Phys.: Condens. Matter* **12**, A147 (2000).
- [8] C. DELLAGO, P. BOLHUIS, and P. GEISLER, Transition path sampling, *Adv. Chem. Phys.* **123**, 1 (2002).
- [9] C. DELLAGO and P. BOLHUIS, Transition Path Sampling and Other Advanced Simulation Techniques for Rare Events, *Adv. Poly. Sci.* **221**, 167 (2008).
- [10] S. TĂNASE-NICOLA and J. KURCHAN, Topological Methods for Searching Barriers and Reaction Paths, *Phys. Rev. Lett.* **91**, 188302 (2003).
- [11] S. TĂNASE-NICOLA and J. KURCHAN, Metastable States, Transitions, Basins and Borders at Finite Temperatures, *J. Stat. Phys.* **116**, 1201 (2004).

- [12] L. O. HEDGES, R. L. JACK, J. P. GARRAHAN, and D. CHANDLER, Dynamic Order-Disorder in Atomistic Models of Structural Glass Formers, *Science* **323**, 1309 (2009).
- [13] G. BENETTIN, L. GALGANI, A. GIORGILLI, and J.-M. STRELCYN, Lyapunov characteristic exponents for smooth dynamical systems and for Hamiltonian systems; a method for computing all of them. I: Theory, *Meccanica* **15**, 9 (1980).
- [14] W. G. HOOVER and H. A. POSCH, Second-law irreversibility and phase-space dimensionality loss from time-reversible nonequilibrium steady-state Lyapunov spectra, *Phys. Rev. E* **49**, 1913 (1994).
- [15] R. B. SHIRTS and W. P. REINHARDT, Approximate constants of motion for classically chaotic vibrational dynamics: Vague tori, semiclassical quantization, and classical intramolecular energy flow, *J. Chem. Phys.* **77**, 5204 (1982).
- [16] R. DVORAK, G. CONTOPOULOS, C. EFTHYMIPOULOS, and N. VOGLIS, Stickiness in mappings and dynamical systems, *Planet. Space Sci.* **46**, 1567 (1998).
- [17] C. DELLAGO, W. G. HOOVER, and H. A. POSCH, Fluctuations, convergence times, correlation functions, and power laws from many-body Lyapunov spectra for soft and hard disks and spheres, *Phys. Rev. E* **65**, 056216 (2002).
- [18] Z. SÁNDOR, B. RDI, and C. EFTHYMIPOULOS, The Phase Space Structure Around L4 in the Restricted Three-Body Problem, *Celest. Mech. Dyn. Astron.* **78**, 113 (2000).
- [19] Z. SÁNDOR, E. BÁLINT, S. ANDRÁS, and B. FUNK, The Relative Lyapunov Indicator: An Efficient Method of Chaos Detection, *Celest. Mech. Dyn. Astron.* **90**, 127 (2004).
- [20] G. CONTOPOULOS and N. VOGLIS, A fast method for distinguishing between ordered and chaotic orbits, *Astron. Astrophys.* **317**, 73 (1997).
- [21] C. DELLAGO and W. HOOVER, Are local Lyapunov exponents continuous in phase space?, *Phys. Lett. A* **268**, 330 (2000).

- [22] C. DELLAGO, P. G. BOLHUIS, and D. CHANDLER, Efficient transition path sampling: Application to Lennard-Jones cluster rearrangements, *J. Chem. Phys.* **108**, 9236 (1998).
- [23] P. G. BOLHUIS, C. DELLAGO, and D. CHANDLER, Sampling ensembles of deterministic transition pathways, *Faraday Discuss.* **110**, (1998).
- [24] B. V. CHIRIKOV, A universal instability of many-dimensional oscillator systems, *Phys. Rep.* **52**, 263 (1979).
- [25] H. A. POSCH, W. G. HOOVER, and C. G. HOOVER, Lyapunov instability of pendulums, chains, and strings, *Phys. Rev. A* **41**, 2999 (1990).
- [26] I. P. OMEL'YAN, I. M. MRYGLOD, and R. FOLK, Optimized Forest-Ruth- and Suzuki-like algorithms for integration of motion in many-body systems, *Comput. Phys. Commun.* **146**, 188 (2002).
- [27] Y. SINAI, On the foundation of the ergodic hypothesis for a dynamical system of statistical mechanics, in *Soviet Math. Dokl.*, volume 4, pp. 1818–1822, 1963.
- [28] J. MACHTA and R. ZWANZIG, Diffusion in a Periodic Lorentz Gas, *Phys. Rev. Lett.* **50**, 1959 (1983).
- [29] C. DELLAGO, L. GLATZ, and H. A. POSCH, Lyapunov spectrum of the driven Lorentz gas, *Phys. Rev. E* **52**, 4817 (1995).
- [30] E. FERMI, J. PASTA, and S. ULAM, Studies of non linear problems, in *Collected Papers of Enrico Fermi.*, pp. 978–988, University of Chicago Press, 1965.
- [31] T. DAUXOIS, M. PEYRARD, and S. RUFFO, The Fermi-Pasta-Ulam 'numerical experiment': history and pedagogical perspectives, *Eur. J. Phys.* **26**, S3 (2005).
- [32] T. CRETEGNY, T. DAUXOIS, S. RUFFO, and A. TORCINI, Localization and equipartition of energy in the β -FPU chain: Chaotic breathers, *Physica D: Nonlinear Phen.* **121**, 109 (1998).
- [33] N. J. ZABUSKY and M. D. KRUSKAL, Interaction of "Solitons" in a Collisionless Plasma and the Recurrence of Initial States, *Phys. Rev. Lett.* **15**, 240 (1965).

- [34] J. E. STRAUB, M. BORKOVEC, and B. J. BERNE, Molecular dynamics study of an isomerizing diatomic in a Lennard-Jones fluid, *J. Chem. Phys.* **89**, 4833 (1988).
- [35] C. DELLAGO, P. G. BOLHUIS, and D. CHANDLER, On the calculation of reaction rate constants in the transition path ensemble, *J. Chem. Phys.* **110**, 6617 (1999).
- [36] J. D. WEEKS, D. CHANDLER, and H. C. ANDERSEN, Role of Repulsive Forces in Determining the Equilibrium Structure of Simple Liquids, *J. Chem. Phys.* **54**, 5237 (1971).
- [37] G. TORRIE and J. VALLEAU, Nonphysical sampling distributions in Monte Carlo free-energy estimation: Umbrella sampling, *J. Comput. Phys.* **23**, 187 (1977).
- [38] A. LAIO and M. PARRINELLO, Escaping free-energy minima, *Proc. Natl. Acad. Sci. USA* **99**, 12562 (2002).
- [39] C. J. GEYER and E. A. THOMPSON, Annealing Markov Chain Monte Carlo with Applications to Ancestral Inference, *J. Am. Statist. Assoc.* **90**, 909 (1995).
- [40] D. FRENKEL and B. SMIT, *Understanding molecular simulation: from algorithms to applications*, Academic Press, 2002.
- [41] D. MORONI, P. R. TEN WOLDE, and P. G. BOLHUIS, Interplay between Structure and Size in a Critical Crystal Nucleus, *Phys. Rev. Lett.* **94**, 235703 (2005).
- [42] W. LECHNER, C. DELLAGO, and P. G. BOLHUIS, Role of the Prestructured Surface Cloud in Crystal Nucleation, *Phys. Rev. Lett.* **106**, 085701 (2011).
- [43] U. U. GASSER, E. R. WEEKS, A. SCHOFIELD, P. N. PUSEY, and D. A. WEITZ, Real-space imaging of nucleation and growth in colloidal crystallization, *Science* **292**, 258 (2003).
- [44] J. D. HONEYCUTT and H. C. ANDERSEN, Molecular dynamics study of melting and freezing of small Lennard-Jones clusters, *J. Phys. Chem.* **91**, 4950 (1987).

-
- [45] C. L. CLEVELAND, W. D. LUEDTKE, and U. LANDMAN, Melting of gold clusters, *Phys. Rev. B* **60**, 5065 (1999).
- [46] D. FAKEN and H. JÓNSSON, Systematic analysis of local atomic structure combined with 3D computer graphics, *Comput. Mater. Sci.* **2**, 279 (1994).
- [47] C. L. KELCHNER, S. J. PLIMPTON, and J. C. HAMILTON, Dislocation nucleation and defect structure during surface indentation, *Phys. Rev. B* **58**, 11085 (1998).
- [48] G. J. ACKLAND and A. P. JONES, Applications of local crystal structure measures in experiment and simulation, *Phys. Rev. B* **73**, 054104 (2006).
- [49] P. J. STEINHARDT, D. R. NELSON, and M. RONCHETTI, Bond-orientational order in liquids and glasses, *Phys. Rev. B* **28**, 784 (1983).
- [50] P.-R. TEN WOLDE, M. J. RUIZ-MONTERO, and D. FRENKEL, Simulation of homogeneous crystal nucleation close to coexistence, *Farad. Discuss.* **104**, 93 (1996).
- [51] S. AUER and D. FRENKEL, Numerical Simulation of Crystal Nucleation in Colloids, *Adv. Polym. Sci.* **173**, 149 (2005).
- [52] W. LECHNER and C. DELLAGO, Accurate determination of crystal structures based on averaged local bond order parameters, *J. Chem. Phys.* **129**, 114707 (2008).
- [53] R. RADHAKRISHNAN and B. L. TROUT, Nucleation of Hexagonal Ice (Ih) in Liquid Water, *J. Am. Chem. Soc.* **125**, 7743 (2003).
- [54] A. V. BRUKHNO, J. ANWAR, R. DAVIDCHACK, and R. HANDEL, Challenges in molecular simulation of homogeneous ice nucleation, *J. Phys.: Condens. Matter* **20**, 494243 (2008).
- [55] A. REINHARDT, J. P. K. DOYE, E. G. NOYA, and C. VEGA, Local order parameters for use in driving homogeneous ice nucleation with all-atom models of water, *J. Chem. Phys.* **137**, 194504 (2012).
- [56] P. L. CHAU and A. J. HARDWICK, A new order parameter for tetrahedral configurations, *Mol. Phys.* **93**, 511 (1998).

- [57] J. R. ERRINGTON and P. G. DEBENEDETTI, Relationship between structural order and the anomalies of liquid water, *Nature* **409**, 318 (2001).
- [58] J. BEHLER and M. PARRINELLO, Generalized Neural-Network Representation of High-Dimensional Potential-Energy Surfaces, *Phys. Rev. Lett.* **98**, 146401 (2007).
- [59] J. BEHLER, Neural network potential-energy surfaces in chemistry: a tool for large-scale simulations, *Phys. Chem. Chem. Phys.* **13**, 17930 (2011).
- [60] S. LORENZ, A. GROSS, and M. SCHEFFLER, Representing high-dimensional potential-energy surfaces for reactions at surfaces by neural networks, *Chem. Phys. Lett.* **395**, 210 (2004).
- [61] J. BEHLER, Atom-centered symmetry functions for constructing high-dimensional neural network potentials, *J. Chem. Phys.* **134**, 074106 (2011).
- [62] J. M. ZURADA, A. MALINOWSKI, and I. CLOETE, Sensitivity Analysis for Minimization of Input Data Dimension for Feedforward Neural Network, in *IEEE International Symposium on Circuits and Systems*, pp. 447–450, 1994.
- [63] H. L. VIKTOR, A. P. ENGELBRECHT, and I. CLOETE, Reduction of Symbolic Rules from Artificial Neural Networks Using Sensitivity Analysis, in *IEEE International Conference on Neural Networks*, volume 4, pp. 1788–1793, 1995.
- [64] A. P. ENGELBRECHT and I. CLOETE, Feature Extraction from Feedforward Neural Networks using Sensitivity Analysis, in *International Conference on Systems, Signals, Control, Computers*, volume 2, pp. 221–225, 1998.
- [65] D. E. RUMELHART, G. E. HINTON, and R. J. WILLIAMS, Learning representations by back-propagating errors, *Nature* **323**, 533 (1986).
- [66] M. T. HAGAN and M. MENHAJ, Training Feedforward Networks with the Marquardt Algorithm, *IEEE Trans. Neural Netw.* **5**, 989 (1994).
- [67] S. SINGHAL and L. WU, Training multilayer perceptrons with the extended Kalman algorithm, in *Advances in neural information processing systems 1*, pp. 133–140, Morgan Kaufmann Publishers Inc., 1989.
- [68] S. HAYKIN, *Kalman filtering and neural networks*, Wiley, 2001.

- [69] F. HEIMES, Extended Kalman filter neural network training: experimental results and algorithm improvements, in *IEEE International Conference on Systems, Man, and Cybernetics*, volume 2, pp. 1639–1644, 1998.
- [70] Y. ZHANG and X. LI, A fast U-D factorization-based learning algorithm with applications to nonlinear system modeling and identification, *IEEE Trans. Neural Netw.* **10**, 930 (1999).
- [71] D. J. LARY and H. Y. MUSSA, Using an extended Kalman filter learning algorithm for feed-forward neural networks to describe tracer correlations, *Atmos. Chem. Phys. Discuss.* **4**, 3653 (2004).
- [72] D. NGUYEN and B. WIDROW, Improving the learning speed of 2-layer neural networks by choosing initial values of the adaptive weights, in *IEEE International Joint Conference on Neural Networks*, volume 3, p. 21, 1990.
- [73] T. MORAWIETZ, Entwicklung eines effizienten Potentials für das Wasser-Dimer basierend auf künstlichen neuronalen Netzen, Master’s Thesis, University of Bochum, 2010.
- [74] H. ESHET, F. BRUNEVAL, and M. PARRINELLO, New Lennard-Jones metastable phase, *J. Chem. Phys.* **129**, 026101 (2008).
- [75] V. G. BAIDAKOV, K. S. BOBROV, and A. S. TETERIN, Cavitation and crystallization in a metastable Lennard-Jones liquid at negative pressures and low temperatures, *J. Chem. Phys.* **135**, 054512 (2011).
- [76] G. J. MARTYNA, M. E. TUCKERMAN, D. TOBIAS, and M. L. KLEIN, Explicit reversible integrators for extended systems dynamics, *Mol. Phys.* **87**, 1117 (1996).
- [77] M. E. TUCKERMAN, *Statistical Mechanics: Theory and Molecular Simulation*, Oxford University Press, 2010.
- [78] E. LINDHOLM, J. NICKOLLS, S. F. OBERMAN, and J. MONTRYM, NVIDIA Tesla: A Unified Graphics and Computing Architecture, *IEEE Micro* **28**, 39 (2008).
- [79] V. PETRENKO and R. WHITWORTH, *Physics of Ice*, Oxford University Press, 1999.

- [80] C. G. SALZMANN, P. G. RADAELLI, A. HALLBRUCKER, E. MAYER, and J. L. FINNEY, The preparation and structures of hydrogen ordered phases of ice, *Science* **311**, 1758 (2006).
- [81] C. G. SALZMANN, P. G. RADAELLI, E. MAYER, and J. L. FINNEY, Ice XV: A New Thermodynamically Stable Phase of Ice, *Phys. Rev. Lett.* **103**, 105701 (2009).
- [82] T. LOERTING and N. GIOVAMBATTISTA, Amorphous ices: experiments and numerical simulations, *J. Phys.: Condens. Matter* **18**, R919 (2006).
- [83] K. WINKEL, M. S. ELSAESSER, E. MAYER, and T. LOERTING, Water polyamorphism: Reversibility and (dis)continuity, *J. Chem. Phys.* **128**, 044510 (2008).
- [84] T. LOERTING, K. WINKEL, M. SEIDL, M. BAUER, C. MITTERDORFER, P. H. HANDLE, C. G. SALZMANN, E. MAYER, J. L. FINNEY, and D. T. BOWRON, How many amorphous ices are there?, *Phys. Chem. Chem. Phys.* **13**, 8783 (2011).
- [85] J. LEKNER, Electrostatics of proton arrangements in ice Ic, *Physica B: Cond. Matter* **240**, 263 (1997).
- [86] W. F. KUHS, J. L. FINNEY, C. VETTIER, and D. V. BLISS, Structure and hydrogen ordering in ices VI, VII, and VIII by neutron powder diffraction, *J. Chem. Phys.* **81**, 3612 (1984).
- [87] B. MINČEVA-ŠUKAROVA, W. SHERMANN, and G. WILKINSON, A high pressure spectroscopic study on the ice III – ice IX. Disordered – ordered transition, *J. Mol. Struct.* **115**, 137 (1984).
- [88] J. D. LONDONO, W. F. KUHS, and J. L. FINNEY, Neutron diffraction studies of ices III and IX on under-pressure and recovered samples, *J. Chem. Phys.* **98**, 4878 (1993).
- [89] H. FUKAZAWA, S. IKEDA, and S. MAE, Incoherent inelastic neutron scattering measurements on ice XI; the proton-ordered phase of ice Ih doped with KOH, *Chem. Phys. Lett.* **282**, 215 (1998).

-
- [90] A. J. LEADBETTER, R. C. WARD, J. W. CLARK, P. A. TUCKER, T. MATSUO, and H. SUGA, The equilibrium low-temperature structure of ice, *J. Chem. Phys.* **82**, 424 (1985).
- [91] H. FUKAZAWA, A. HOSHIKAWA, H. YAMAUCHI, Y. YAMAGUCHI, and Y. ISHII, Formation and growth of ice XI: A powder neutron diffraction study, *J. Cryst. Growth* **282**, 251 (2005).
- [92] Y. TAJIMA, T. MATSUO, and H. SUGA, Calorimetric study of phase transition in hexagonal ice doped with alkali hydroxides, *J. Phys. Chem. Sol.* **45**, 1135 (1984).
- [93] O. YAMAMURO, M. OGUNI, T. MATSUO, and H. SUGA, High-pressure calorimetric study on the ice XI – Ih transition, *J. Chem. Phys.* **86**, 5137 (1987).
- [94] R. HOWE and R. W. WHITWORTH, A determination of the crystal structure of ice XI, *J. Chem. Phys.* **90**, 4450 (1989).
- [95] S. M. JACKSON, V. M. NIELD, R. W. WHITWORTH, M. OGURO, and C. C. WILSON, Single-Crystal Neutron Diffraction Studies of the Structure of Ice XI, *J. Phys. Chem. B* **101**, 6142 (1997).
- [96] J.-C. LI, V. NIELD, and S. JACKSON, Spectroscopic measurements of ice XI, *Chem. Phys. Lett.* **241**, 290 (1995).
- [97] J. LEKNER, Energetics of hydrogen ordering in ice, *Physica B: Cond. Matter* **252**, 149 (1998).
- [98] T. K. HIRSCH and L. OJAMÄE, Quantum-Chemical and Force-Field Investigations of Ice Ih: Computation of Proton-Ordered Structures and Prediction of Their Lattice Energies, *J Phys. Chem. B* **108**, 15856 (2004).
- [99] V. BUCH, P. SANDLER, and J. SADLEJ, Simulation of H₂O Solid, Liquid, and Clusters, with an Emphasis in Ferroelectric Ordering Transition in Hexagonal Ice, *J. Phys. Chem. B* **102**, 8642 (1998).
- [100] A. GARG, High-pressure Raman spectroscopic study of the ice Ih → ice IX phase transition, *Phys. Stat. Sol. (a)* **110**, 467 (1988).

- [101] H. ITOH, K. KAWAMURA, T. HONDOH, and S. MAE, Polarized librational spectra of proton-ordered ice XI by molecular dynamics simulations, *J. Chem. Phys.* **109**, 4894 (1998).
- [102] K. FURIC and V. VOLOVSEK, Water ice at low temperatures and pressures: New Raman results, *J. Mol. Structure* **976**, 174 (2010).
- [103] J. L. F. ABASCAL, E. SANZ, R. G. FERNANDEZ, and C. VEGA, A potential model for the study of ices and amorphous water: TIP4P/Ice, *J. Chem. Phys.* **122**, 234511 (2005).
- [104] C. LAWRENCE and J. SKINNER, Flexible TIP4P model for molecular dynamics simulation of liquid water, *Chem. Phys. Lett.* **372**, 842 (2003).
- [105] M. NEUMANN, Dielectric relaxation in water. Computer simulations with the TIP4P potential, *J. Chem. Phys.* **85**, 1567 (1986).
- [106] J. MARTÍ, E. GUÀRDIA, and J. PADRÓ, Dielectric properties and infrared spectra of liquid water: Influence of the dynamic cross correlations, *J. Chem. Phys.* **101**, 10883 (1994).
- [107] A. RAHMAN and F. H. STILLINGER, Proton Distribution in Ice and the Kirkwood Correlation Factor, *J. Chem. Phys.* **57**, 4009 (1972).
- [108] R. AYALA and V. TCHIOV, A molecular dynamics study of ices III and V using TIP4P and TIP5P water models, *Can. J. Phys.* **81**, 11 (2003).
- [109] A. K. SOPER, The radial distribution functions of water and ice from 220 to 673 K at pressures up to 400 MPa, *Chem. Phys.* **258**, 121 (2000).
- [110] D. A. MCQUARRIE, *Statistical Mechanics*, Harper and Row, New York, 1976.
- [111] R. ZWANZIG, *Nonequilibrium Statistical Mechanics*, Oxford University Press, USA, 2001.
- [112] J. MARTÍ, J. PADRÓ, and E. GUÀRDIA, Molecular dynamics calculation of the infrared spectra in liquid H₂O-D₂O mixtures, *J. Mol. Liq.* **62**, 17 (1994).
- [113] L. G. MACDOWELL and C. VEGA, Dielectric Constant of Ice Ih and Ice V: A Computer Simulation Study, *J. Phys. Chem. B* **114**, 6089 (2010).

- [114] P. E. BLÖCHL, Projector augmented-wave method, *Phys. Rev. B* **50**, 17953 (1994).
- [115] G. KRESSE and D. JOUBERT, From ultrasoft pseudopotentials to the projector augmented-wave method, *Phys. Rev. B* **59**, 1758 (1999).
- [116] J. P. PERDEW, K. BURKE, and M. ERNZERHOF, Generalized Gradient Approximation Made Simple, *Phys. Rev. Lett.* **77**, 3865 (1996).
- [117] M. DION, H. RYDBERG, E. SCHRÖDER, D. C. LANGRETH, and B. I. LUNDQVIST, Van der Waals Density Functional for General Geometries, *Phys. Rev. Lett.* **92**, 246401 (2004).
- [118] J. KLIMEŠ, D. R. BOWLER, and A. MICHAELIDES, Chemical accuracy for the van der Waals density functional, *J. Phys.: Condens. Matter* **22**, 022201 (2010).
- [119] J. KLIMEŠ, D. R. BOWLER, and A. MICHAELIDES, Van der Waals density functionals applied to solids, *Phys. Rev. B* **83**, 195131 (2011).
- [120] G. KRESSE, J. FURTHMÜLLER, and J. HAFNER, Ab initio Force Constant Approach to Phonon Dispersion Relations of Diamond and Graphite, *Europhys. Lett.* **32**, 729 (1995).
- [121] Z. RAZA, D. ALFE, C. G. SALZMANN, J. KLIMES, A. MICHAELIDES, and B. SLATER, Proton ordering in cubic ice and hexagonal ice; a potential new ice phase-XIc, *Phys. Chem. Chem. Phys.* **13**, 19788 (2011).
- [122] J. HARL and G. KRESSE, Accurate Bulk Properties from Approximate Many-Body Techniques, *Phys. Rev. Lett.* **103**, 056401 (2009).
- [123] J. HARL, L. SCHIMKA, and G. KRESSE, Assessing the quality of the random phase approximation for lattice constants and atomization energies of solids, *Phys. Rev. B* **81**, 115126 (2010).
- [124] B. SANTRA, J. C. V. KLIMEŠ, D. ALFÈ, A. TKATCHENKO, B. SLATER, A. MICHAELIDES, R. CAR, and M. SCHEFFLER, Hydrogen Bonds and van der Waals Forces in Ice at Ambient and High Pressures, *Phys. Rev. Lett.* **107**, 185701 (2011).

- [125] C. VEGA, C. MCBRIDE, E. SANZ, and J. L. F. ABASCAL, Radial distribution functions and densities for the SPC/E, TIP4P and TIP5P models for liquid water and ices I, I, II, III, IV, V, VI, VII, VIII, IX, XI and XII, *Phys. Chem. Chem. Phys.* **7**, 1450 (2005).
- [126] E. R. DAVIDSON and K. MOROKUMA, A proposed antiferroelectric structure for proton ordered ice Ih, *J. Chem. Phys.* **81**, 3741 (1984).
- [127] S. J. SINGER and C. KNIGHT, Hydrogen-Bond Topology and Proton Ordering in Ice and Water Clusters, *Adv. Chem. Phys.* **147**, 1 (2011).
- [128] M. ARAKAWA, H. KAGI, and H. FUKAZAWA, Laboratory Measurements of Infrared Absorption Spectra of Hydrogen-ordered Ice: A Step to the Exploration of Ice XI in Space, *Astrophys. J. Suppl. Ser.* **184**, 361 (2009).
- [129] J. BERTIE, H. LABBÉ, and E. WHALLEY, Absorptivity of Ice I in the Range 4000–30 cm, *J. Chem. Phys.* **50**, 4501 (1969).
- [130] J. EAVES, A. TOKMAKOFF, and P. GEISLER, Electric Field Fluctuations Drive Vibrational Dephasing in Water, *J. Phys. Chem. A* **109**, 9424 (2005).
- [131] S. CORCELLI and J. SKINNER, Infrared and Raman Line Shapes of Dilute HOD in Liquid H₂O and D₂O from 10 to 90 °C, *J. Phys. Chem. A* **109**, 6154 (2005).
- [132] C. G. SALZMANN, A. HALLBRUCKER, J. L. FINNEY, and E. MAYER, Raman spectroscopic study of hydrogen ordered ice XIII and of its reversible phase transition to disordered ice V, *Phys. Chem. Chem. Phys.* **8**, 3088 (2006).
- [133] A. HALLBRUCKER, E. MAYER, and G. P. JOHARI, The heat capacity and glass transition of hyperquenched glassy water, *Phil. Mag. B* **60**, 179 (1989).
- [134] I. KOHL, E. MAYER, and A. HALLBRUCKER, The glassy water-cubic ice system: a comparative study by X-ray diffraction and differential scanning calorimetry, *Phys. Chem. Chem. Phys.* **2**, 1579 (2000).
- [135] B. PAMUK, J. M. SOLER, R. RAMÍREZ, C. P. HERRERO, P. W. STEPHENS, P. B. ALLEN, and M.-V. FERNÁNDEZ-SERRA, Anomalous Nuclear Quantum Effects in Ice, *Phys. Rev. Lett.* **108**, 193003 (2012).

- [136] H. SUGA, A facet of recent ice sciences, *Thermochim. Acta* **300**, 117 (1997).
- [137] T. LI, D. DONADIO, G. RUSSO, and G. GALLI, Homogeneous ice nucleation from supercooled water, *Phys. Chem. Chem. Phys.* **13**, 19807 (2011).
- [138] T. F. MILLER III, M. ELEFThERIOU, P. PATTNAIK, A. NDIRANGO, D. NEWNS, and G. J. MARTYNA, Symplectic quaternion scheme for biophysical molecular dynamics, *J. Chem. Phys.* **116**, 8649 (2002).
- [139] H. KAMBERAJ, R. J. LOW, and M. P. NEAL, Time reversible and symplectic integrators for molecular dynamics simulations of rigid molecules, *J. Chem. Phys.* **122**, 224114 (2005).
- [140] D. QUIGLEY and P. M. RODGER, Metadynamics simulations of ice nucleation and growth, *J. Chem. Phys.* **128**, 154518 (2008).
- [141] A. REINHARDT and J. P. K. DOYE, Free energy landscapes for homogeneous nucleation of ice for a monatomic water model, *J. Chem. Phys.* **136**, 054501 (2012).
- [142] R. G. FERNANDEZ, J. L. F. ABASCAL, and C. VEGA, The melting point of ice I_h for common water models calculated from direct coexistence of the solid-liquid interface, *J. Chem. Phys.* **124**, 144506 (2006).
- [143] V. C. WEISS, M. RULLICH, C. KOHLER, and T. FRAUENHEIM, Kinetic aspects of the thermostatted growth of ice from supercooled water in simulations, *J. Chem. Phys.* **135**, 034701 (2011).
- [144] B. MEHLIG, D. W. HEERMANN, and B. M. FORREST, Hybrid Monte Carlo method for condensed-matter systems, *Phys. Rev. B* **45**, 679 (1992).
- [145] I. P. OMELIAN, I. M. MRYGLOD, and R. FOLK, Optimized Verlet-like algorithms for molecular dynamics simulations, *Phys. Rev. E* **65**, 056706 (2002).
- [146] V. MOLINERO and E. B. MOORE, Water Modeled As an Intermediate Element between Carbon and Silicon, *J. Phys. Chem. B* **113**, 4008 (2009).
- [147] B. GUILLOT, A reappraisal of what we have learnt during three decades of computer simulations on water, *J. Mol. Liq.* **101**, 219 (2002).

- [148] M. TUCKERMAN, B. J. BERNE, and G. J. MARTYNA, Reversible multiple time scale molecular dynamics, *J. Chem. Phys.* **97**, 1990 (1992).
- [149] W. L. JORGENSEN, J. CHANDRASEKHAR, J. D. MADURA, R. W. IMPEY, and M. L. KLEIN, Comparison of simple potential functions for simulating liquid water, *J. Chem. Phys.* **79**, 926 (1983).
- [150] C. VEGA and J. L. F. ABASCAL, Simulating water with rigid non-polarizable models: a general perspective, *Phys. Chem. Chem. Phys.* **13**, 19663 (2011).
- [151] B. KAMB, W. C. HAMILTON, S. J. LA PLACA, and A. PRAKASH, Ordered Proton Configuration in Ice II, from Single-Crystal Neutron Diffraction, *J. Chem. Phys.* **55**, 1934 (1971).
- [152] S. J. LA PLACA, W. C. HAMILTON, B. KAMB, and A. PRAKASH, On a nearly proton-ordered structure for ice IX, *J. Chem. Phys.* **58**, 567 (1973).
- [153] C. LOBBAN, J. L. FINNEY, and W. F. KUHS, The structure and ordering of ices III and V, *J. Chem. Phys.* **112**, 7169 (2000).
- [154] S. NOSÉ and M. KLEIN, Constant pressure molecular dynamics for molecular systems, *Mol. Phys.* **50**, 1055 (1983).
- [155] M. E. TUCKERMAN, Y. LIU, G. CICCOTTI, and G. J. MARTYNA, Non-Hamiltonian molecular dynamics: Generalizing Hamiltonian phase space principles to non-Hamiltonian systems, *J. Chem. Phys.* **115**, 1678 (2001).
- [156] S. NOSÉ, A unified formulation of the constant temperature molecular dynamics methods, *J. Chem. Phys.* **81**, 511 (1984).
- [157] W. G. HOOVER, Canonical dynamics: Equilibrium phase-space distributions, *Phys. Rev. A* **31**, 1695 (1985).
- [158] H. C. ANDERSEN, Molecular dynamics simulations at constant pressure and/or temperature, *J. Chem. Phys.* **72**, 2384 (1980).
- [159] J. LEKNER, Summation of Coulomb fields in computer-simulated disordered systems, *Physica A: Stat. Mech. App.* **176**, 485 (1991).

-
- [160] M. NEUMANN and O. STEINHAUSER, The influence of boundary conditions used in machine simulations on the structure of polar systems, *Mol. Phys.* **39**, 437 (1980).
- [161] M. NEUMANN, O. STEINHAUSER, and G. S. PAWLEY, Consistent calculation of the static and frequency-dependent dielectric constant in computer simulations, *Mol. Phys.* **52**, 97 (1984).
- [162] M. P. ALLEN and D. J. TILDESLEY, *Computer simulation of liquids*, Clarendon Press, 1989.
- [163] D. M. HEYES, Pressure tensor of partial-charge and point-dipole lattices with bulk and surface geometries, *Phys. Rev. B* **49**, 755 (1994).
- [164] J. ALEJANDRE, D. J. TILDESLEY, and G. A. CHAPELA, Molecular dynamics simulation of the orthobaric densities and surface tension of water, *J. Chem. Phys.* **102**, 4574 (1995).
- [165] G. HUMMER, N. GRONBECH-JENSEN, and M. NEUMANN, Pressure calculation in polar and charged systems using Ewald summation: Results for the extended simple point charge model of water, *J. Chem. Phys.* **109**, 2791 (1998).
- [166] A. Y. TOUKMAJI and J. A. BOARD JR., Ewald summation techniques in perspective: a survey, *Comp. Phys. Comm.* **95**, 73 (1996).
- [167] Z. A. RYCERZ and P. W. M. JACOBS, Ewald Summation in the Molecular Dynamics Simulation of Large Ionic Systems, *Mol. Sim.* **8**, 197 (1992).
- [168] Z. A. RYCERZ, Calculation of the Coulomb Interactions in Condensed Matter Simulation, *Mol. Sim.* **9**, 327 (1992).
- [169] G. HUMMER, The numerical accuracy of truncated Ewald sums for periodic systems with long-range Coulomb interactions, *Chem. Phys. Lett.* **235**, 297 (1995).
- [170] W. L. JORGENSEN and J. D. MADURA, Temperature and size dependence for Monte Carlo simulations of TIP4P water, *Mol. Phys.* **56**, 1381 (1985).

- [171] H. J. C. BERENDSEN, J. R. GRIGERA, and T. P. STRAATSMA, The missing term in effective pair potentials, *J. Phys. Chem.* **91**, 6269 (1987).
- [172] M. WEINWURM and C. DELLAGO, Vibrational Spectroscopy of Water in Narrow Nanopores, *J. Phys. Chem. B* **115**, 5268 (2011).
- [173] T. S. VAN ERP, D. MORONI, and P. G. BOLHUIS, A novel path sampling method for the calculation of rate constants, *J. Chem. Phys.* **118**, 7762 (2003).
- [174] H. GOLDSTEIN, *Classical Mechanics*, Addison-Wesley, Reading, MA, 1980.
- [175] J. DIEBEL, Representing Attitude: Euler Angles, Unit Quaternions, and Rotation Vectors, 2006.
- [176] G. STRANG, On the Construction and Comparison of Difference Schemes, *SIAM J. Numer. Anal.* **5**, 506 (1968).
- [177] M. E. TUCKERMAN, J. ALEJANDRE, R. LPEZ-RENDN, A. L. JOCHIM, and G. J. MARTYNA, A Liouville-operator derived measure-preserving integrator for molecular dynamics simulations in the isothermalisobaric ensemble, *J. Phys. A: Math. Gen.* **39**, 5629 (2006).
- [178] M. J. LOUWERSE and E. J. BAERENDS, Calculation of pressure in case of periodic boundary conditions, *Chem. Phys. Lett.* **421**, 138 (2006).

Curriculum vitae

Philipp Geiger

Mödling, Austria

email: philipp.geiger@univie.ac.at, philipp.geiger@tuwien.ac.at

Personal Details

- Nationality: Austria
- Birthplace: Vienna, Austria
- Date of birth: 16.09.1980
- Command of languages: German (mother tongue), English

Education

- **PhD study of Computational Physics**
since June 2008 under supervision of Prof. Dr. Christoph Dellago
University of Vienna, Austria
- **Study of Computational Physics**
2003 - 2008 obtained *Mag. rer. nat.* 'mit Auszeichnung' on 20th May 2008
(equivalent to a Master of Science degree with honors)
University of Vienna, Austria
- **High school**
1995 - 2000 Federal Secondary College of Engineering (HTL)
branch of study: Industrial engineering and management
(Wirtschaftsingenieurwesen), Mödling, Austria
1992 - 1995 Private HS, Gebrüder-Lang-Gasse, Vienna, Austria
1991 - 1992 Jakob-Thoma HS, Mödling, Austria
- **Elementary school**
1987 - 1991 VS Lerchengasse, Mödling, Austria

Work History

- Miscellaneous minor employments 2002 - 2003

Other Activities

- Alternative civilian service 2001

Academic achievements

Grants

- | | |
|-----------------------|--|
| since Oct. 2012 | Employee of the project 'Fourier Monte Carlo Simulation of Elastic Membranes' Vienna University of Technology, Austria |
| Apr. 2012 - Sep. 2012 | Employee of the project 'VASP Vienna Ab-initio Simulation Package' University of Vienna, Austria |
| Nov. 2008 - Mar. 2012 | Doctoral student program 'Wissenschaftskolleg' at the CMS - Center for Computational Materials Science, University of Vienna, Austria |
| May 2008 - Oct. 2008 | Junior Research Fellow at the Erwin Schrödinger International, Institute for Mathematical Physics Vienna, Austria |

Teaching

- Tutor and temporary lecturer, Introduction to Mathematical Methods in Physics I+II,
University of Vienna 2007 - 2009, 2011

Presentations

- 8th Liquid Matter Conference, Vienna, Austria, *Freezing of water: local structure detection using neural networks*, September 2011 (poster presentation)

- Vienna Computational Materials Laboratory (ViCoM) seminar, *Local structure detection of polymorphic systems using neural networks*, January 2011 (oral presentation)
- CECAM workshop Lausanne: 'Crystallization: from colloids to pharmaceuticals', *Proton order of cubic ice*, July 2010, (poster presentation)

Publications

- G. Menzl, M. A. Gonzalez, J. L. Aragoes, Ph. Geiger, G. Pallares, M. El Mekki-Azouzi, F. Caupin, J. L. F. Abascal, Ch. Dellago, Ch. Valeriani, *Developing an order parameter for cavitation: A thermodynamically consistent bubble volume*, in preparation.
- G. Menzl, M. A. Gonzalez, J. L. Aragoes, Ph. Geiger, G. Pallares, M. El Mekki-Azouzi, F. Caupin, J. L. F. Abascal, Ch. Dellago, Ch. Valeriani, *Homogeneous cavitation in water under negative pressure*, in preparation.
- Ph. Geiger, and Ch. Dellago, *Structure detection in polymorphic system using neural networks*, submitted to Journal of Chemical Physics.
- Ph. Geiger, Ch. Dellago, M. Macher, C. Franchini, G. Kresse, J. Bernard, J. N. Stern and T. Lörting, *Proton ordering of cubic Ic: experiments and computer simulations*, submitted to Physical Review B.
- Ph. Geiger, and Ch. Dellago, *Identifying rare chaotic and regular trajectories in dynamical systems with Lyapunov weighted path sampling*, Chemical Physics **375**, 309-315 (2010)
- Ph. Geiger, and Ch. Dellago, *Optimum protocol for fast-switching free energy calculations*, Physical Review E **81**, 021127 (2010)
- Ph. Geiger, Diploma thesis: *Optimal protocol for fast switching non-equilibrium processes*, (2008)